Fabrication of High-Performance Probes for Atomic Force Microscope (AFM)

by

Medhat Samaan

A thesis

presented to the University of Waterloo

in fulfillment of the

thesis requirement for the degree of

Doctor of Philosophy

in

Electrical and Computer Engineering

Waterloo, Ontario, Canada, 2021

© Medhat Samaan 2021

Examining Committee membership

Professor Bo Cui, Electrical and Computer Engineering, Supervisor

Professor Karim Karim, Electrical and Computer Engineering

Professor Omar M. Ramahi, Electrical, and Computer Engineering

Professor Boxin Zhao, Chemical Engineering

Professor Wen-Di Li, Mechanical Engineering, Univ. of Hong Kong (external examiner)

Author's Declaration

I hereby declare that I am the sole author of this thesis. This is a true copy of the thesis, including any required final revisions, as accepted by my examiners.

I understand that my thesis may be made electronically available to the public.

Abstract

Atomic force microscope (AFM) is widely used for topographical structure characterization. However, one serious issue with AFM imaging is the intrinsic artifact in the AFM image when mapping a none-flat surface (e.g. a deep and narrow hole/trench) where the tip cannot fully follow the sample surface. The natural solution to overcome this issue is by using thin and high aspect ratio (HAR) tips that can follow the sample surface more precisely. This thesis focuses on the fabrication of HAR AFM probes. The HAR tips are obtained by modifying regular AFM tips having a pyramid shape. The high aspect ratio structure in silicon, sitting on top of a pyramid base, is created by a dry plasma etching process, so the key is to form a hard metal dot right on top of the pyramid tip apex to act as the mask for silicon etching.

Three approaches were developed to form the hard mask metal nano-dot on the tip apex. The first method (Chapter 3) employed metal deposition steps with the regular tip mounted on a tilted surface, and its etching back to leave behind metal only at the tip apex (the metal on the sidewall of the pyramid was etched away). Since both metal film deposition and its etching, as well as the subsequent dry plasma etching of silicon using the metal as mask to form the HAR structure, can be carried out on an entire wafer of regular AFM tips, this process is a low-cost and high throughput batch process. The second method (Chapter 6) utilized focused ion beam (FIB). FIB has been extensively used to fabricate HAR tips by milling away the silicon surrounding the tip axis, leaving behind a thin pillar or sharp cone of silicon at the pyramid axis. However, the FIB milling time for each tip is long, leading to high cost. Our method used FIB to mill away only a very thin layer of metal film to leave behind a metal dot at tip apex, thus the expensive FIB machine time is greatly reduced. The third method (Chapter 6) also utilized Ga-ion FIB, but instead of milling a metal dot mask pattern, the Ga ions were implanted to the tip apex area to act as a mask since Ga metal is resistant to fluorine-based plasma etching.

For the above three approaches, silicon etching is very critical, so Chapter 5 covers our effort in developing silicon etching recipes using a non-switching pseudo-Bosch process with C_4F_8-SF_6 gas, with a goal of obtaining vertical sidewall profile needed for HAR, high selectivity to mask, and high etching rate. As well,

the etched silicon structures must be further sharpened to reduce its apex radius to below 10nm. So, Chapter 4 covers the process optimization of the oxidation sharpening process that involves thermal oxidation and subsequent oxide etching by HF. It was found that 950°C is a suitable oxidation temperature, and the oxidation sharpening can be carried out more than once to improve tip sharpness.

Lastly, inspired by the first approach described above, we also developed the fabrication process for "edge probe" (Chapter 3), for which the tip apex sits right at the end of the cantilever, and thus the tip location can be precisely determined in the view of the integrated optical microscope in an AFM system. Our method involves angle evaporation of a hard mask layer onto the AFM probe, followed by silicon dry etching that etches away the area not covered by the metal layer, i.e., the shadow area of the pyramid-shaped tip.

Acknowledgments

First, I would like to express my appreciation to my supervisor Professor Bo Cui. This work would not be possible without his guidance throughout the entire work.

I would also like to thank my examination committee members Professor Karim Karim, Professor Omar Ramahi, Professor Boxin Zhao and Professor Wen-Di Li (external examiner), who agreed to be my committee members and rearranged their schedules to make this exam possible as well as their valuable advices.

Also, I would like to thank my group mates for their support. It is worth to mention that the nanopillars wet etch experiment is done in collaboration with Aixi Pan and Xiaoli Zhu, and the ion implantation experiments are performed in collaboration with Huseyn Ekinci and Ripon Dey. Besides, the edge tip and batch HAR tip is accomplished in collaboration with Chenxu Zhu and Shuo Zheng.

Finally, I would like to express my gratitude to the nanofabrication facilities at Quantum NanoFab, WATLab, and Giga-to-Nanoelectronics (G2N) Laboratory at the University of Waterloo. Quantum NanoFab infrastructure would not be possible without the significant contributions of the Canada Foundation for Innovation, the Ontario Ministry of Research & Innovation, Industry Canada, and Mike & Ophelia Lazaridis. Likewise, the G2N laboratory is funded by the Canada Foundation for Innovation, the Ontario Ministry of Research & Innovation, and Industry Canada; their support is also greatly appreciated.

Table of Contents

Examining Committee membership II
Author's Declaration III
Abstract....................IV
Acknowledgments....................VI
List of Figures ....**xiiI**
List of Tables .... **xix**

Chapter 1

Overview of micro-nano fabrication techniques **1**
1.1. Nanofabrication overview **1**
1.2. Evaporation **3**
1.2.1. Thermal evaporation **3**
1.2.2. Electron beam evaporation **4**
1.3. Atomic layer deposition (ALD) **5**
1.4. Etching....................6
1.4.1. Wet etch **6**
1.4.1.1. Introduction **6**
1.4.1.2. Silicon wet etchants **8**
1.4.1.2.1. Potassium Hydroxide (KOH) **8**
1.4.1.2.2. Tetramethylammonium Hydroxide (TMAH) **8**
1.4.1.2.3. Nitric and Hydrofluoric acid (HNO_3 - HF) etch 9
1.4.2. Dry etch....................**10**
1.4.2.1. Introduction **10**
1.4.2.2. Deep RIE (DRIE) of silicon processes 13
1.4.2.2.1. Bosch process....................**13**
1.4.2.2.2. Cryogenic DRIE 15
1.5. Focus ion beam (FIB) **18**
1.5.1. Introduction **18**
1.5.2. FIB construction....................**18**
1.5.3. FIB utilization **21**

1.6. Atomic force microscope 22
1.6.1. Introduction 22
1.6.1.1. Microscope families....................22
1.6.2. The basic principle of atomic force microscopy 23
1.6.3. Construction of atomic force microscopy 24
1.7. Thesis structure....................25

Chapter 2

Introduction to AFM tip fabrication techniques....................26
2.1. Basics of AFM probes 26
2.1.1. AFM probe assembly....................26
2.1.2. AFM probe (tip) classification....................26
2.1.3. Cantilevers's classification 28
2.1.4. Tip holder 29
2.2. AFM tip fabrication....................30
2.2.1. Fabrication techniques of AFM probes....................30
2.2.3. High aspect ratio (HAR) tips fabrication....................33
2.2.3.1. Focused ion beam milling method 34
2.2.3.2. Electron/ion beam induced deposition (EBID/IBID) method....................36
2.2.3.3. Carbon Nanotube (CNT) attachment method 37
_2.2.3.4. "Nauga-needle formation" method 39
2.2.3.5. Angle dependant dry etching method 39
2.2.4. Edge tip fabrication 40

Chapter 3

Batch fabrication of edge and high aspect ratio AFM tips using thin film deposition and etching techniques....................42
3.1. Introduction 42
3.2. Fabrication of edge tip 43
3.2.1. Introduction 43
3.2.2. Experiment and process discussions....................44
3.2.2.1. Deposition of the mask material....................44
3.2.2.2. Dry etch to remove the silicon 46

3.2.2.3. Wet etch to remove the hard mask 47
3.2.2.4. Sharpening of the tip 48
3.2.3. Results and testing the edge tip 49
3.3. Fabrication of HAR tip 50
3.3.1. Introduction 50
3.3.2. Experiment and process discussion 51
3.3.2.1. Deposition of two materials 52
3.3.2.2. Cr_2O_3 dry etch 52
3.3.2.3. Al wet etch 53
3.3.2.4. Si RIE 53
3.3.2.5. Sharpening the tip using oxidation 54
3.3.3. Results and testing the tip 54
3.4. Conclusion 55

Chapter 4

AFM tip sharpening using oxidation technique 56
4.1. Thermal oxidation 56
4.2. AFM tip sharping by oxidation 57
4.3. AFM tip sharpening techniques 57
4.3.1. Dry and wet oxidation 60
4.3.2. Oxidation growth direction and effect 61
4.4. Experimental process of oxidation sharpening of the AFM probes 64
4.4.1. Temperature selection 65
4.4.2. Furnace calibration 66
4.4.3. Optimal oxidation time for commercial probes 67
4.4.4. Multiple oxidations sharpening to achieve sharper probes 71
4.5. Conclusion 73

Chapter 5

Fabrication of ultra-high aspect ratio (UHAR) silicon nanopillars array 74
5.1. Introduction 74
5.2. Dry etch 75

5.2.1. Reactive Ion Etch (RIE) parameter 75
5.2.2. Examples of different techniques of HAR nanostructures 76
5.2.3. Experiment and discussion 79
5.2.3.1. Effect of increasing ICP and RF power 80
5.2.3.2. The effect of oxygen plasma cleaning cycle on etching rate and profile 82
5.2.3.3. The effect of gas ratio on etching rate and etching shape 86
5.2.3.3.1. Further investigation on the gas ratio 90
5.2.3.4. Investigation on cone shape pillars using specific SF_6/C_4F_8 gas ratio of 10/50 91
5.2.4. Dry etch conclusion 93
5.3. Wet etch 93
5.3.1. Introduction 93
5.3.2. Experiment 94
5.3.3. Results and discussion 95
5.3.4. Wet etch conclusion 98

Chapter 6

Fabrication of HAR AFM tips and nano pillars using FIB (Focus Ion Beam) 99
6.1. Fabrication of HAR tip using FIB 99
6.1.1. Introduction 99
6.1.2. Experiment and process discussion 99
6.1.2.1. Deposition of two materials 100
6.1.2.2. FIB milling 101
6.1.2.3. Al RIE dry etch 102
6.1.2.4. Si RIE dry etch 103
6.1.3. Process transferred to commercial tip 104
6.1.4. Testing the tip for AFM imaging 106
6.1.5. Fabrication of HAR tip with reduced FIB milling time 107
6.1.6. Semiautomatic fabrication of HAR tip using Focused Au and Si Ion Beam 110
6.1.6.1. Fabrication of the tip 111
6.1.6.2. Results and tip testing 115
6.2. Ion implantation 116
6.2.1. Introduction 116
6.2.2. Ga ion implantation experiment and discussion 122

6.2.3. Au FIB ion implantation 124
6.2.3.1. Experiment and discussion 125
6.3. Conclusion 127

Chapter 7

Conclusion 129

References 132

List of Figures

Fig 1.1 Examples of top down and bottom-up fabrication sequences …………………………………..2

Fig 1.2 Crucible and schematic of the thermal evaporation ………………………….……………4

Fig 1.3 Schematic of e-beam generation and e-beam evaporation ..…………………….…………………4

Fig 1.4 ALD deposition steps ……………………………………………………………………...5

Fig 1.5 (left) Steps for the ALD of the Al_2O_3 , (right) Al_2O_3 film on a Si wafer with a trenches structure ……………………………………………………….…………………………………6

Fig 1.6 Isotropic / anisotropic etch ….…………………………………………………...…………...7

Fig 1.7 Crystal plans of silicone ……………………..…………………………..………………..7

Fig 1.8 Constant rate of change of die thickness as a function of the etchant composition ...………...10

Fig 1.9 Schematic of the plasma structure ………………………………………..………..……..11

Fig 1.10 RIE etch steps ……………………………………………...…………………………..…..12

Fig 1.11 Cross sectional of Oxford Instruments ICP RIE ………………………………...……..…..12

Fig 1.12 (left) (a) Ideal profile (b) real profile employing a Bosch process. (right) SEM image of a pillar etched by Bosch process ……………………………………………………………………………14

Fig 1.13 Cryo-etching physical and chemical mechanisms ……………………..…………………16

Fig 1.14 Cryogenic processes etch characteristics ………………………………………………..17

Fig 1.15 FIB construction ….………………..…………………………………………………....19

Fig 1.16 Liquid metal ion source (LIMS) ………………………………………...……………....20

Fig 1.17 Principle of FIB utilization; (a) milling, (b) deposition, (c) implantation, (d) imaging ….…..21

Fig 1.18 The intermolecular forces F(r) and the potential energy V(r) between two bodied, vs distance ……………………………………………………………………………………………....24

Fig 1.19 (left) schematic of AFM construction, (right) AFM in block diagram ……………………....25

Fig 2.1 Schematic of AFM probe assembly ……………………….…………………………...…26

Fig 2.2 Different AFM tip apex …………………………………………………………………..27

Fig 2.3 AFM tip apex shapes ……………………………………………………………....…27

Fig 2.4 Tilt / regular / rotated HAR AFM tip ……………………………………..……………....27

Fig 2.5 Edge AFM tips ……………………………………………....…………………………..28

Fig 2.6 (a) Regular tip (b) HAR tip ……………………………………..………………………..28

Fig 2.7 AFM cantilevers shapes ……………………………………….……………………....29

Fig 2.8 Different AFM cantilevers cross-section ……………………………………….……………..29

Fig 2.9 Number of AFM cantilevers per prob …..……………..…………………………………....29

Fig 2.10 Support chip of AFM tip ..………………………………………………………………….30

Fig 2.11 AFM tip fabrication using (top) molding method (bottom) etching method ………………....31

Fig 2.12 Advanced techniques for inverse pyramid cavity concept ………………….………………..32

Fig 2.13 The process to fabricate the rocket tip ………………………………………………………..33

Fig 2.14 (top) Regular AFM tip and the scanned profile of a hole/trench. (bottom) HAR tip and its scanned profile ………………………………………………………….………………………………..…33

Fig 2.15 Commercial HAR tip examples where the tips are fabricated with (a) focused ion beam milling; (b) electron beam induced deposition; (c) carbon nanotube attachment, (d) spike attachment, and (e) "Nauga-needle formation" technique ……………………………………….…………………………34

Fig 2.16 Nitride AFM tip before and after FIB milling ……………………………………….……….35

Fig 2.17 (a) A fabricated HAR tip, (b) achieved the radius of the tip ……………………..…...………36

Fig 2.18 Pyramidal nitride tip before and after depositing a carbon pillar on its apex ………………....37

Fig 2.19 Needle height as a function of carbon deposition time, (a) 20 s. (b) 10 s. (c) 5 s …………….37

Fig 2.20 (a) Surface growth CVD nanotube tip (b) single CNT attached on cantilever produce by directional growth plasma enhanced CVD (c) Nanotube attachment method through 'pick-up', (bottom) shows the TEM image of a SWNT (single walled nanotube) tip ……………………………………………..……38

Fig 2.21 Nauga-needle fabrication steps, schematic drawing, and corresponding SEM images ………39

Fig 2.22 Sputtering yield vs ion incident angle for ion milling ……………………………..……….40

Fig 2.23 Angle Dependant Dry etching steps ..…………………………………………….…..……..40

Fig 2.24 Different edge tips ...…………………………………………………………………….……41

Fig 3.1 Appnano, AIO, and rocket probes respectively (left to right) ………………………………….42

Fig 3.2 Examples of few AFM edge tips ……………………………………………..…………..43

Fig 3.3 60° Angle deposition using e-beam followed by Si RIE then wet etch for both (a) cantilever end and (b) cantilever back ..……...………………………………………………………………...…………44

Fig 3.4 The results of the mask layer consisting of (a) Cr (b) Al (c) Cr_2O_3 …….……………………….45

Fig 3.5 60° Angle deposition setup on a tip from two different sides ……………………….................45

Fig 3.6 Tip after 60° angle deposition from both (a) front, and (b) opposite side of the tips …..............46

Fig 3.7 Etch results of the tip in both cases (left) front deposition (right) back deposition ….…...........47

Fig 3.8 Tip after Cr_2O_3 wet etch ……..……………………………..………………………………..…48

Fig 3.9 Sharpening the tip by oxidation and HF etching ……………..………………………………..48

Fig 3.10 SEM image of the edge sharpened tip …..…………………..……………………………….49

Fig 3.11 Screenshot of AFM screen for front edge tip, back edge tip, and regular tip respectively from left to right ……………………………………………………………………………...…………………..49

Fig 3.12 (top left) AFM scanning result of Regular tip (top right) testing sample (bottom) AFM scanning result of edge tip …………………………………………………………………………………….…50

Fig 3.13 Some examples of HAR commercial tips ………………………………………………....51

Fig 3.14 Schematic of the process steps to make HAR tip ……………………………...…………..51

Fig 3.15 60° Cr_2O_3/Al deposition in both front and back of AFM tip …….….……….….…………..52

Fig 3.16 The final product of the HAR tip showing the 4 apexes (1, 2, 3, 4 respectively from left to right) of a single AIO probe (tips of AIO probe are numbered at the far left ……………………………..…53

Fig 3.17 HAR tip after the oxidation ………………..………………………………………………54

Fig 3.18 AFM scan for (up) regular AFM tip (bottom) our fabricated HAR AFM tip …….…………...55

Fig 4.1 Thermal oxidation curve for furness programming ……………………………….……....…..…56

Fig 4.2 Oxidation sharpening steps ………………………………………………………..……...……..57

Fig 4.3 Growing silicon oxide in a mold to sharp the tip ………………………….…..…...……...58

Fig 4.4 Tip fabrication process ……………………………………………………….…………….……58

Fig 4.5 Process flow for sharpened pyramid tip fabricating ……………………………..……….......59

Fig 4.6 Main fabrication process flow ………………………………………….……….…….…..……59

Fig 4.7 Fabrication of sharp silicon tips ……………………………………….……………..……...60

Fig 4.8 Calculation of the oxidation rate from D-G model (left) dry (right) wet ………..……..............61

Fig 4.9 Oxidation stages of silicon tip with (A) initially large half-angle θ> 20 °, (B) initially small half angle θ = ~ 5° ………………………………………………………………………….…..………...62

Fig 4.10 SEM image outcome after breaking the top tip and θ is largely resulting in multiple tips 62

Fig 4.11 Silicon tip oxidation …………………………………………………………..……..……..63

Fig 4.12 Regular commercial AIO AFM tip with 40nm apex ………………………….…..……..…64

Fig 4.13 low-cost furnace box with maximum temperature less than 1200 °C …………..…...………64

Fig 4.14 Resulting images of different temperatures of oxidation and cleaning at (A) 850 °C, (B) 900 °C, (C) 950 °C, (D) 1000 °C, (E) 1050 °C, (F) 1100 °C, (G) 1150 °C ………………..……..…...………..66

Fig 4.15 AFM blunt tips (a) pyramidal (b) spherical …………………………………………...…..66

Fig 4.16 Furnace calibration at 950 °C for a different time duration vs oxidation depth ……..…..……67

Fig 4.17 Results after removing the oxide for different oxidation duration at 950 °C (A) 0.5h, (B) 1h, (C) 1.5h, (D) 2h, (E) 2.5h, (F) 3h, (G) 3.5h, (H) 4h ……………………………………………............69

Fig 4.18 Results after removing the oxide for different time duration at 950 °C (A) 5h, (B) 6h, (C) 7h, (D) 8h, (E) 9h, (F) 10h, (G) 11h, (H) 12h, (I) 13h, (J) 14h, (K) 15h, (L) 16h, (M) 17h, (N) 18h, (O) 19h, (P) 20h …………………………………………………………………………………..……………….…70, 71

Fig 4.19 SEM images after removing the oxide surface of the probes with oxidization temperature of 950 °C and duration of 1/2h (A) 1 step (B) 2 steps (C) 3 steps (D) 4 steps ………..……………….…….…...…72

Fig 4.20 SEM images after cleaning oxidation at 950 °C for 1h oxidation time for (A) 1 steps (B) 2 steps (C) 3 steps ……………………………………………………………………...……….…………..…..72

Fig 4.21 SEM images after cleaning oxidation at 950 °C for (A) 1h then 0.5 h oxidation time (b) 2 steps of 1h and 0.5 h oxidations time (C) 3 steps of 1h and 0.5 h oxidations time ……………………………73

Fig 4.22 SEM image of the swollen tip in real time due to longer exposure time from the electron beam ………………………………………………………………………………….…..……73

Fig 5.1 The effects of the Bosch process parameters ………………………………………………76

Fig 5.2 Silicon pillar arrays masked with TiN (left) Cross-section, (middle) top and (right) tilted SEM images …………………………………………………………………………………………....77

Fig 5.3 Process flow of high aspect ratio silicon ……………...……………………………………....78

Fig 5.4 Fabrication process of the nanopillar array (a) silicon wafer (b) chrome deposition (c) photoresist layer (d) photoresist patterned by direct exposure (e) chrome etch (f) DRIE silicon etched (g) oxygen plasma etching the residual photoresist …………………………….……………….……………78

Fig 5.5 Fabrication of the sample array of masks (a) Si wafer (b) photoresist deposition and e-beam lithography (c) photoresist etch (d) Cr evaporation (e) photoresist removal …….………………..…..79

Fig 5.6 SEM image for 4 min etches with ICP 1200 for 500, 800, 1200 nm Cr mask diameters ..……80

Fig 5.7 SEM image for 3.26 min etches with ICP 1600 for 500, 800, 1200 nm Cr mask diameters ….81

Fig 5.8 SEM image for 2.48 min etches with ICP 2000 for 500, 800, 1200 nm Cr mask diameters ….81

Fig 5.9 SEM image for 10 min etches with for 1200, 800, 500 nm Cr mask diameters with gas ratio SF6/C4F8 = 22/38 respectively left to right, the lower image is the magnification of the top images .82

Fig 5.10 SEM image for 20 min etches for 500, 800, 1200 nm Cr mask diameters with gas ratio SF6/C4F8 = 15/45, respectively left to right, the lower image is the magnification of the top images…………..83

Fig 5.11 SEM image for 40 cycles etches and for 1200, 800, 500 nm Cr mask diameters with the gas ratio of SF6/C4F8 = 22/38, respectively left to right, the lower image is the magnification of the top images..84

Fig 5.12 SEM image for 40 cycles etches with 500, 800, 1200 nm Cr mask diameters, the gas ratio of SF6/C4F8 =15/45 respectively left to right, the lower image is 1200 Cr mask diameter undercut……...85

Fig 5.13 SEM image of square edge with Cr mask and SF6/C4F8 gas ratio of 40/20, 30/30, 20/40, 50/10, 55/5, 10/50, and 5/55 respectively left to right and top to bottom……………………………………..…88

Fig 5.14 SEM image with 5 µm Cr mask diameter, and SF6/C4F8 gas ratio of 40/20, 30/30, 20/40, 50/10, 55/5, 10/50, and 5/55 respectively left to right and top to bottom……………………………………..89

Fig 5.15 SEM image with 1 µm Cr mask diameter and SF6/C4F8 gas ratio of 40/20, 30/30, 20/40, 10/50, and 5/55 respectively left to right and top to bottom, 50/10 and 55/5 gas ratio did not survive…………90

Fig 5.16 SEM image with 5 μm Cr mask diameter and SF6/C4F8 gas ratio of 42/18, 44/16, 46/14, and 48/12 respectively left to right and top to bottom………..……………………………………..……...91

Fig 5.17 The pattern of each sample ...……………………………………………………….……….92

Fig 5.18 SEM image for 40 min etch with gas ratio of C4F8/ SF6 = 50/10 for 1.2, 1.5, 2 μm regular mask diameters left to right respectively…………………………………………………………….,,,,,,,…92

Fig 5.19 SEM image for 40 min etch with gas ratio of C4F8/ SF6 = 50/10 for elongated side mask diameters of 1.4, 1.8, 2.1 μm left to right respectively…..…………………………………………………………92

Fig 5.20 (a) Schematic illustration of fabrication steps (b) & (c) the outcome of the process …………94

Fig 5.21 A rough sidewall surface of the pillar before wet sharping …………………………………...96

Fig 5.22 (left) nanopillars array before sharpening process. (right) detailed information and profile of pillars before sharpening, the diameter of the pillar is 755.1nm ……………………………………….…..97

Fig 5.23 Etching rates for different Acids Concentration vs vertical and horizontal etch in nm ...………………………………………………………………………………………..…………..…97

Fig 5.24 (left) nanopillars array after sharpening process, (right) detailed information and profile of pillars after sharpening, the diameter of the pillar is 73.71nm …..…………………………….………………98

Fig 6.1 Schematic of the process flow to make high aspect ratio pillars using FIB (on Si wafer) (a) shows the wafer before processing (b) displays 30 nm of Al deposition, (c) demonstrates the 10 nm Cr deposition, (d) after FIB milling of Cr 10 nm (Cr acts as a metal mask in Al etch), (e) after Al etching using RIE, (f) after Deep Si etch. (g) after wet etch to clean the Cr and Al ……………………………………...100

Fig 6.2 The expected result when applying the technique on the regular commercial AFM tip …….100

Fig 6.3 (left) Test locations for FIB milling doses (right) close-up view of each circle with the FIB milling the red area ..……………………………………………………………………………………..101

Fig 6.4 AFM results after the FIB milling …………………………..…………………………..…102

Fig 6.5 70° Tilted SEM images right after Si etch .…………………………………………..…103

Fig 6.6 70° Tilted SEM images of individual holes arranged as shown in Fig 6.1.2.2.1. (left) ……..104

Fig 6.7 (left) Top view after 39 s FIB exposure (middle) 70° tilted SEM images after 39 s FIB exposure (right) 70° tilted SEM images of the final product after 39 s FIB, Al etch for 25 s and Si etch …,,,...105

Fig 6.8 (left) Top view after 75 s FIB exposure (middle) 70° tilted SEM images after 75 s FIB exposure (right) 70° tilted SEM images of the final product after 75 s FIB, Al etch for 25 s and Si etch ……..105

Fig 6.9 (left) top view after 75 s FIB exposure (middle) 70° tilted SEM images after 75 s FIB exposure (right) 70° tilted SEM images of the final product after 75 s FIB, Al etch for 40 s and Si etch …......105

Fig 6.10 (left) Top view after 143 s FIB exposure (middle) 70° tilted SEM images after 143 s FIB exposure (right) 70° tilted SEM images of the final product after 143 s FIB, Al etch for 25 s and Si etch…….105

Fig 6.11 70° Tilted SEM images of HAR tip using different FIB doses (left) 35 s (middle) 40 s (right) 45 s ...……………………………………………………………………………………………….…106

Fig 6.12 (top) AFM scan using regular tip (top right) test sample (bottom) AFM scan using HAR tip fabricated by FIB ..…………………………………………………………………………….....107

Fig 6.13 (A) Angle deposition (B) FIB complete circle exposure area (C) partial FIB exposure area .107

Fig 6.14 Top view SEM images for two orientations of FIB partial exposures on the metal deposition area only for (left) 200° out of 360° circle of exposure (right) 300° out of 360° circle of exposure ………108

Fig 6.15 70° Tilted SEM images show the final results of the tips after fabrication (left) using 200° out of 360° circle of exposure (right) using 300° out of 360° circle of exposure ………………………….…109

Fig 6.16 AFM scan using (top) regular tip (middle) the 200° partial exposure tip (bottom) 300 ° partial exposure tip, where (top right) is the testing sample ……………………………………………………..110

Fig 6.17 (A) Exposure pattern for FIB (B) SEM scan for Si ion experiment (C) SEM scan for Au ion experiment ……………………………………………………………………………………………112

Fig 6.18 (left) Top view of the tip after FIB exposure (right) 70° tilted SEM images of the final result of the fabricated tip with 14 pA and128 mC/cm^2 FIB dose (5 min), Al RIE etch for 25s, and Si etch for 1.45 mint ……………………………………………………………………………………………………...113

Fig 6.19 (left) Top view of the tip after FIB exposure (right) 70° tilted SEM images of the final result of the fabricated tip with 14 pA and 256 mC/cm^2 FIB dose (10 min), Al RIE etch for 25s, and Si etch for 1.45 min ………………………………………………………………………………………,,,,,,,.……113

Fig 6.20 (left) Top view of the tip after FIB exposure (right) 70° tilted SEM images of the final results of the fabricated tip with 30 pA and128 mC/cm^2 FIB dose (5 min), Al RIE etch for 25s, and Si etch for 1.45 min ...……………………………………………………………………………………….……114

Fig 6.21 (left) Top view of the tip after FIB exposure (right) 70° tilted SEM images of the final results of the fabricated tip with 30 pA and 256 mC/cm^2 FIB dose (5 min), Al RIE etch for 45s, and Si etch for 1.45min ………………………………………………………………………………….…...…114

Fig 6.22 70° Tilted SEM images of higher beam current exposure (75 pA)……………….………..…115

Fig 6.23 AFM scan using (top left) regular tip (bottom) fabricated HAR AFM tip, while (top right) is the testing sample ...……………………………………………………………………………………116

Fig 6.24 SEM image for the structural profile of the implant array after etching ………..……………..118

Fig 6.25 Ga+ implantation depth vs beam voltage …………………………………………..………..…119

Fig 6.26 The step height versus gallium dose with various DRIE etch times …….……………………119

Fig 6.27 The plot of implanted dose as a function of incident dose, with limiting value is 3×10^{17} Ga atoms cm^{-2} ………………………………………..……………………………………………....…120

Fig 6.28 SEM image of Ga implanted nanoscale dose array in silicon, the implant image for visual mark and the full-scale image ……………………………………...…………………………….………..…..121

Fig 6.29 The threshold of variable Ga implantation doses and various etch times ……………………..122

Fig 6.30 70° Tilted SEM images of the sample after the recipe is done. 2 second exposure on the two left columns and 40 seconds on the two right columns, while all the other doses come in increments doses every two columns in between ……………………………………………………………………….....123

Fig 6.31 70° Tilted SEM images of (Right) SEM image of the final result for 2 second Ga FIB exposure (Left) SEM image of the final result for 40 second Ga FIB exposure …………………..………………124

Fig 6.32 (a) Exposure pattern for FIB (b) Cr sample (c) Al sample ..………………………………...…126

Fig 6.33 Cr sample, 70° tilted SEM images of (right) top right is spot# 16, (left) top is spot# 16 ………..126

Fig 6.34 Cr sample, 70° tilted SEM images of (right) is spot# 5, (left) is spot# 9 ……………………..…126

Fig 6.35 Cr sample, 70° tilted SEM images (right) the first one from the bottom is # 1, (left) is spot# 1…127

Fig 6.36 Cr sample, 70° tilted SEM images (right) the bottom is spot# 4 (left) is spot# 4 ……………...127

List of Tables

Table 1.1 Comparison of thermal and electron beam evaporation ………..……………………………3

Table 1.2 Etching table (material and etchant) ……………………………………………….………7

Table 1.3 Hard mask materials and their deposition and patterning techniques ……….………………...13

Table 1.4 Typical settings for "Bosch process" using different ICP configurations ……………………..15

Table 1.5 Typical process parameters of the Cryo-DRIE process that results in vertical sidewalls …….18

Table 1.6 The main differences between SEM and FIB ……………………...………………..………20

Table 1.7 The FIB parameters and their possible effects …………………………,,,,,,,,,.………..……22

Table 1.8 The most familiar SPM techniques and families …….……………………………..………..23

Table 3.1 Pseudo Bosch Si etch recipe …………………….…………………………………….………47

Table 3.2 Cr_2O_3 etch recipe ……………………...……………………………………………….…53

Table 5.1 Summarizes The effect of the oxygen plasma cleaning cycle on etching rate and profile………..86

Table 5.2 Experimental results for different SF_6/C_4F_8 gas ratio …………………..…………………..87

Table 5.3 Experimental results for extra SF6/C4F8 gas ratio ……………………………………………..90

Table 6.1 The spot numbers and the depth in nm after FIB mill and Al dry etch ………………………103

Table 6.2 Hole position and related FIB dose ……………………………………………………….....111

Table 6.3 AFM depth after ion implantation, after Al RIE etch and after Si RIE etch for both Si FIB (left) and Au FIB (right) samples ….…………………...…………………………………………………....112

Table 6.4 Dose calculation for the related time of exposure ……………………………………… …….123

Table 6.5 Spot hole position and related FIB exposure dose ……………………………………………125

Chapter 1

Overview of micro-nano fabrication techniques

This chapter gives a brief introduction to the nanofabrication techniques employed in this research as well as the proposed thesis structure. The techniques cover evaporation, wet etch, dry etch using reactive ion etching (RIE), atomic layer deposition (ALD), focus ion beam (FIB), and atomic force microscope (AFM).

1.1. Nanofabrication overview

Nanofabrication [1] [2] [3] is the new generation of microfabrication. It is the fabrication of nanoscale features with sub-100 nm size. "Top down" and "bottom up" are the two processes of nanofabrication as shown in Fig 1.1. Top-down nanofabrication relies on three core techniques, which are lithography, thin-film deposition, and etching. This process is used in the industry to fabricate random access memory, integrated circuits, storage device, microfluidics, solar cells, etc. The bottom-up approach is done by self assembly nanolithography followed by pattern transfer, such as lift-off. It is the self-assembly of nanoscale blocks into an ordered array of nanostructures and nanoparticles. This process includes self assembly of block copolymers and template-based methods that utilize self formed nano porous membranes.

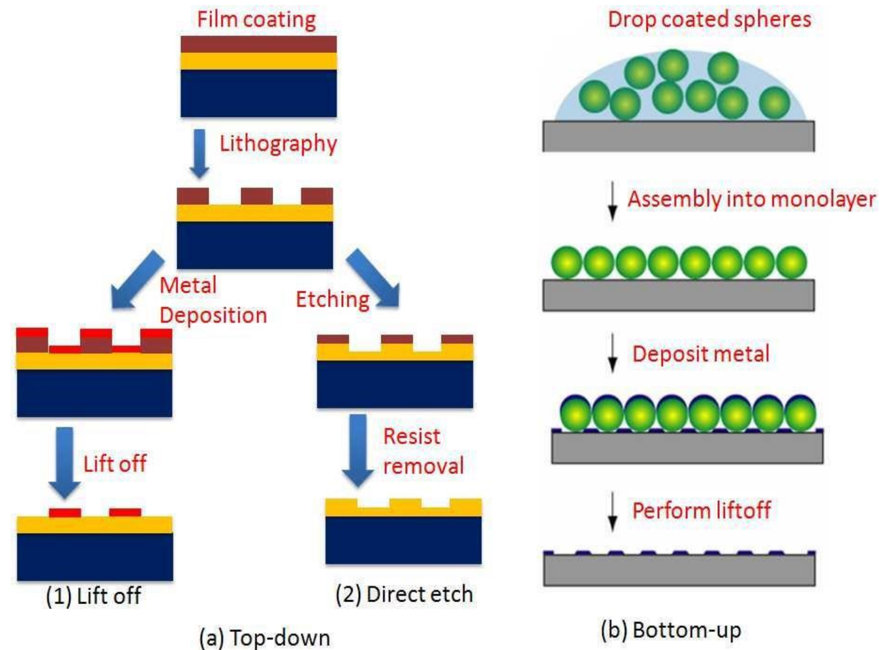

Fig 1.1 Examples of top down and bottom-up fabrication sequences [4]

Lithography [5] [6] [7] [8] [9] [10] is the transfer of the pattern to a sensitive material called resist either by mechanical force or by exposure to photons, ions, or electrons. Lithography techniques can be classified into two types. The first type uses a mask or mold, which includes x-ray lithography (XRL), deep ultra-violet lithography (DUVL), extreme ultraviolet lithography (EUVL), and nanoimprint lithography (NIL). It is good for high volume production and has a high throughput. The second type is direct patterning, which includes electron beam lithography (EBL), ion beam lithography (IBL), and scanning probe lithography (SPL). It is suitable for R&D and mask/mold production since it is time-consuming and has low throughput.

The thin film deposition is done by either physical vapor deposition (PVD) [11] [12] [13] [14] [15] [16] or chemical vapor deposition (CVD). PVD includes sputtering, e-beam, or thermal evaporation. CVD includes metal-organic CVD, plasma-enhanced CVD, and low-pressure CVD.

The etching [17] [18] [19] [20] is the technique for selectively removing material. Wet and dry etching are the two types of etching techniques. Wet etch is cheap and simple, but difficult to control and repeatability is an issued of concern. On the other hand, dry etching is the process of using a gas phase plasma etch in both chemical etching and/or physical sputtering. Etching may either be isotropic or anisotropic. Chemical etching is generally isotropic, whereas physical etching is anisotropic.

1.2. Evaporation

Evaporation [21] [22] [23] [24] [25] [26] is a physical vapor deposition technique utilizing two types of heating sources: thermal or e-beam heating. Both involve the heating of the source material to a high temperature, which results in the vaporization, traveling, and condensing of the atoms onto the substrate as a thin film. A quick difference is shown in Table 1.1.

Table 1.1 [27]Comparison between thermal and electron beam evaporation

Deposition Category	Material	Typical evaporant	Cost	Temperature Range	Impurity
Thermal	Metal, organic materials	Au, Ag, Al, Cu, Cr, Sn, Polystyrene…	Low	$\leq$ 1600°C	High
Electron-beam	Metal and dielectrics	Everything above plus: Ni, Pt, W, Ta…	High	$\geq$ 3000°C	Low

1.2.1. Thermal evaporation

In thermal evaporation, [28] [29] [30] [31] heating is conducted by filament or RF coils passing an electrical current to heat the crucible to vaporize the material inside it. Since the heat provided in this method is limited by 1600°C, this method is good for materials with low melting points and organic materials. The most common materials that are handled by thermal evaporation include Au, Ag, Al, Sn, Cr, Sb, Ge, In, Mg, Ga, CdS, PbS, CdSe, NaCl, KCl, AgCl, MgF_2, CaF_2, $PbCl_2$. It is performed in a high vacuum chamber ($P < 10^{-5}$ Torr) to minimize collisions of source atoms. The major advantage of thermal evaporation is its low-cost. However, the drawback is the heating of the crucible and the filament, cause more contamination. Fig 1.2 shows a schematic of thermal evaporation.

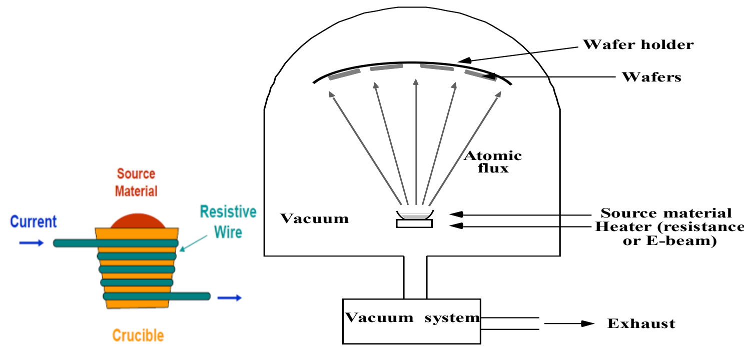

Fig 1.2 Crucible and schematic of the thermal evaporation [32]

1.2.2. Electron beam evaporation

The source of heat for this technique [33 34 35 36 37] is the focused high energy electron beam bombardment, which is generated by an electron gun and accelerated by a high electric field using high potential, as high as 10 kV. The beam is directed by a strong magnet, as shown in Fig 1.3. The crucible is not heated since there is a water-cooling system and the beam is localized at the source material surface. Together these ensure lower contamination from the crucible materials. Temperatures may reach a very high level. This is the reason for using e-beam evaporation on materials with high melting points.

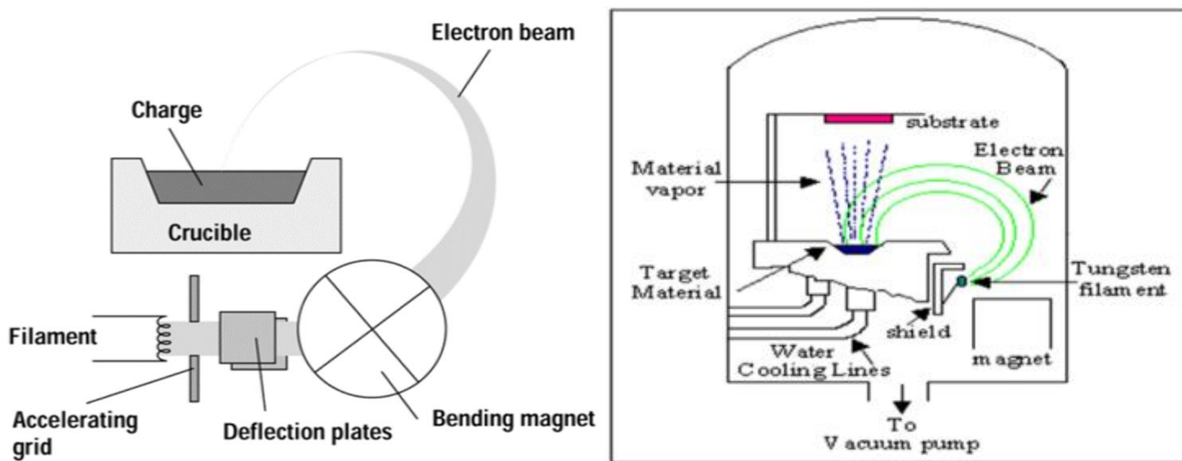

Fig 1.3 Schematic of e-beam generation and e-beam evaporation [38]

1.3. Atomic layer deposition (ALD)

The ALD history [39] goes back to the 1970s in Finland when the pioneer Tuomo Suntola demonstrated some of the first processes. Today, ALD [40] [41] has become an important process for depositing thin films in a wide range of applications. It consists of a sequential self-limiting reaction, which can control the deposition thickness one layer at a time. Fig 1.4 shows the schematic of ALD process. It is based on a binary reaction sequence where two reactions occur sequentially. The process can be repeated on the desired number of layers. Some benefits of the ALD include Angstrom thickness precision controlled by monolayer and good conformal coverage of the surface with the help of self-limiting characteristics.

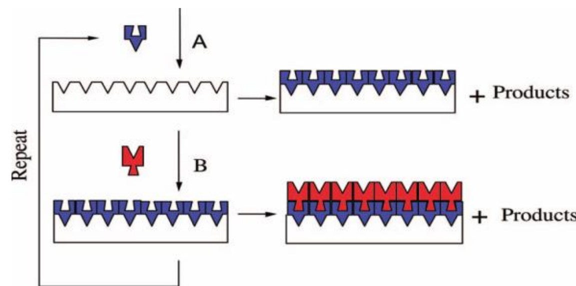

Fig 1.4 ALD deposition steps [42]

A good model of ALD is the deposition of Al_2O_3. This was done using trimethylaluminum (TMA) / ($Al_2(CH_3)_6$) and H_2O dating back to the late 1980s and early 1990s, though recently TMA and ozone are more commonly used. Fig 1.5 (left) shows the binary steps for the ALD of the Al_2O_3 while Fig 1.5 (right) shows Al_2O_3 film with a thickness of 300 nm on a Si wafer with trench structures employing ALD deposition.

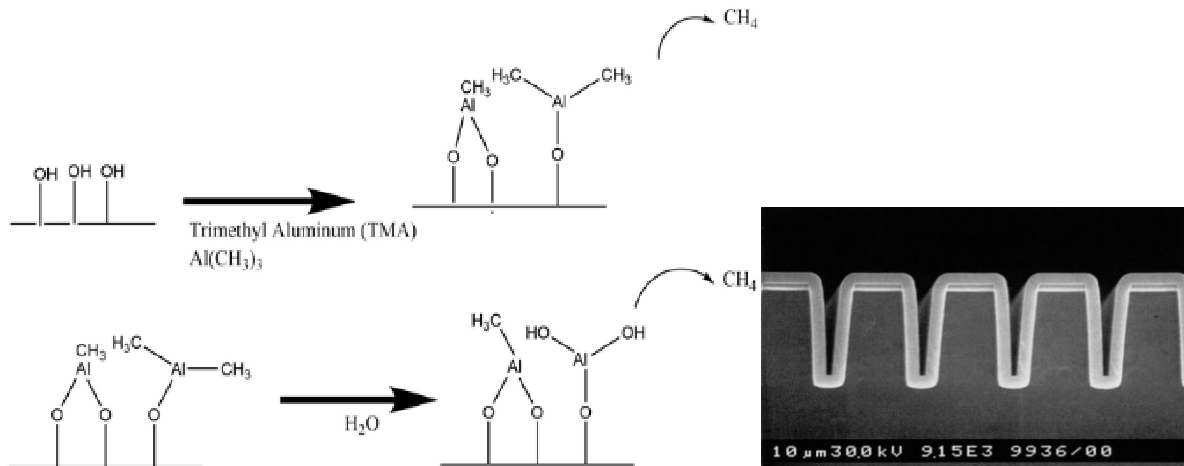

Fig 1.5 (left) Steps for the ALD of the Al_2O_3[43], (right) Al_2O_3 film on a Si wafer with trenches structure

1.4. Etching

The etching is the process that selectively removes the targeted materials while having little or no effect on the masking material on the same substrate. The etching process includes two types: wet etch and dry etch. A wet etch involves liquid chemicals, whereas a dry etch involves a gas phase to remove materials and is commonly conducted through the plasma reactive ion etchant (RIE) technique. The main parameters used in the etching process are etching profile, rate, and selectivity. The etching rate is the etched thickness per unit time and selectivity is the ratio of the etching rate between different materials.

1.4.1. Wet etch

1.4.1.1. Introduction

A wet etch [44] [45] [46] [47] [48] [49] [50] [51] is performed through immersion of the wafers into the solution of the etchant and can involve higher temperatures. Isotropic and anisotropic are the two types of wet etch profiles. As shown in Fig 1.6 (a) isotropic etching has an equal etching rate in all directions, whereas anisotropic etching has different rates in different directions as in Fig 1.6 (b). Silicon etching rate using KOH is slower in <111> crystal plane than <110> and <100> planes. The crystal plane of silicon is shown in Fig 1.7. Table 1.2 lists the popular etchants for important materials.

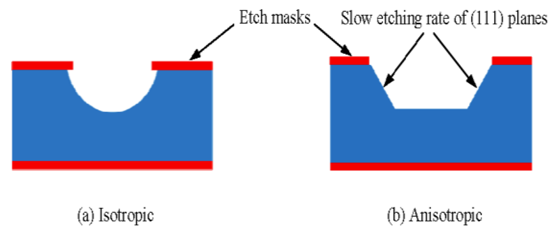

Fig 1.6 Isotropic / anisotropic etch [52]

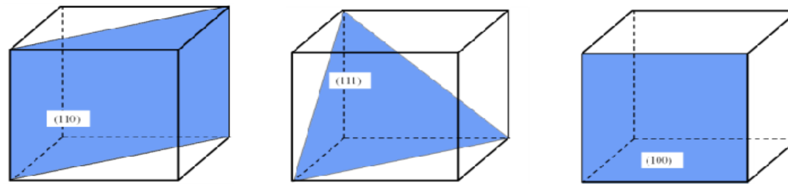

Fig 1.7 Crystal plans of silicone

Table 1.2 [53]Etching table (material and etchant)

Material to be etched	Wet etchants
Aluminium (Al)	80% phosphoric acid (H_3PO_4) + 5% acetic acid + 5% nitric acid (HNO_3) + 10% water (H_2O) at 35–45 °C[4]
Indium tin oxide [ITO] (In_2O_3:SnO_2)	Hydrochloric acid (HCl) + nitric acid (HNO_3) + water (H_2O) (1:0.1:1) at 40 °C[6]
Chromium (Cr)	• "Chrome etch": ceric ammonium nitrate ($(NH_4)_2Ce(NO_3)_6$) + nitric acid (HNO_3)[7] • Hydrochloric acid (HCl)[7]
Gallium Arsenide (GaAs)	• Citric Acid diluted ($C_6H_8O_7$: H_2O, 1 : 1) + Hydrogen Peroxide (H_2O_2)+ Water (H_2O)
Gold (Au)	Aqua regia, Iodine and Potassium Iodide solution
Molybdenum (Mo)	
Organic residues and photoresist	Piranha etch: sulfuric acid (H_2SO_4) + hydrogen peroxide (H_2O_2)
Platinum (Pt)	Aqua regia
Silicon (Si)	• Nitric acid (HNO_3) + hydrofluoric acid (HF)[4] • Potassium hydroxide (KOH) • Ethylenediamine pyrocatechol (EDP) • Tetramethylammonium hydroxide (TMAH)
Silicon dioxide (SiO_2)	• Hydrofluoric acid (HF)[4] • Buffered oxide etch [BOE]: ammonium fluoride (NH_4F) and hydrofluoric acid (HF)[4]
Silicon nitride (Si_3N_4)	• 85% Phosphoric acid (H_3PO_4) at 180 °C[4] (Requires SiO_2 etch mask)
Tantalum (Ta)	
Titanium (Ti)	Hydrofluoric acid (HF)[4]
Titanium nitride (TiN)	• Nitric acid (HNO_3) + hydrofluoric acid (HF) • SC1 • Buffered HF (bHF)
Tungsten (W)	• Nitric acid (HNO_3) + hydrofluoric acid (HF) • Hydrogen Peroxide (H_2O_2)

1.4.1.2. Silicon wet etchants

The main Si wet etchants are potassium hydroxide (KOH), tetramethylammonium hydroxide (TMAH), and the mixture of nitric and hydrofluoric acid (HNO_3 – HF).

1.4.1.2.1. Potassium Hydroxide (KOH)

For KOH etching of Si, the etching rate for the (111) plane is much slower than that of (110) and (100) planes, because the (111) plane has three of its bonds below the surface and only one dangling bond to react with the etchant. The etch rate anisotropy becomes a valuable property, as it offers low-cost, precise, and 3D shapes with smooth, shiny facets, leading to complex structures with multiple functionalities. The facets are controlled by the fastest etched orientations for convex shapes such as the square island corners [54] [55] [56].

KOH etching of silicon employs Si_3N_4, SiO_2, Cr, or Au as a mask. The selectivity is good between Si and SiO_2, the order of ~100, but it is much higher for Si_3N_4, the order of ~10000. Besides its advantage of providing excellent etching profiles, KOH is safe and easy to use. However, the presence of an alkali metal (potassium) makes it completely incompatible with MOS and CMOS processing. The etching rate ratio for KOH anisotropic etch are 160:80:1 for <100>:<110>:<111> orientations, which are done at a concentration of 35% by weight at 70°C, but the ratio changes dramatically for other conditions. The orientation-dependent etch rate of silicon in KOH has been tested at different concentrations and temperatures by many researchers. Typical concentrations and temperatures are 30-50% by weight at 60-90°C.

1.4.1.2.2. Tetramethylammonium Hydroxide (TMAH)

The TMAH water solutions are nontoxic, easy to use, and MOSFET/CMOS compatible. However, TMA+ can cause breathing difficulties and may damage the nerves and muscles. SiO_2, Si_3N_4, Cr, and Au can be used as masks. TMAH has an etch rates anisotropy of 70:35:1 for orientations of <100>: <110>:<111> at 20% by weight and 80°C. The etch profile depends on concentration and temperature, which is between 10% and 25% by weight and temperature between 60°C and 80°C. Though the TMAH etching rate

anisotropy is lower than KOH etching, TMAH has a high selectivity between Si and SiO_2 and there are no harmful ions for the electrical integrated circuits. Also, TMAH etching is more sensitive to diffusion effects, especially at low concentrations (e.g., 10 % by weight), so the repeatability of the etch rate is lower than KOH.

1.4.1.2.3. Nitric and Hydrofluoric acid (HNO_3 – HF) etch

The combination of HNO_3 and HF can etch silicon in two sequential steps [57] [58] [59] [60]. The first step is oxidation by HNO_3, followed by the oxide dissolution by HF. The ratio of the two acids is the critical factor for etching. The etching can be represented by the following chemical equation:

$$Si + HNO_3 + 6HF \rightarrow H_2SiF_6 + HNO_2 + H_2O + H_2$$

The resulting products are HNO_2 (nitrous acid), H_2SiF_6 (hexafluorosilicic acid), H_2, and H_2O.

The oxidation step is the rate-limiting factor when HNO_3 is low with rich HF, and the oxide removal is the rate-limiting factor when HF is low with rich HNO_3. In this low HF regime, crystal defect, surface orientation, and catalysis by reduced nitrogen oxide play an important role. If neither of the two components has a high concentration due to dilution by water or acetic acid, the etching rate will be low.

Fig 1.8 shows the etching rate as a function of the etchant composition. The solid curves represent the etching rate for acetic acid dilution, whereas the dashed curves represent that with water dilution. The addition of a small amount of sodium nitrite enhances the rate of reaction, but too much sodium nitrite reduces the reaction rate by the formation of a protective film.

There are three regions of interest: the high nitric acid, the high hydrofluoric acid, and the maximum etch rate region. In the high nitric acid region, the curves run parallel with lines of constant hydrofluoric acid, indicating that hydrofluoric acid plays an important role. This region gives a smooth polished etch surface. In the high hydrofluoric acid region, the curves run parallel with constant nitric acid, indicating the importance of nitric acid. In the maximum etch rate region, both components play an important role.

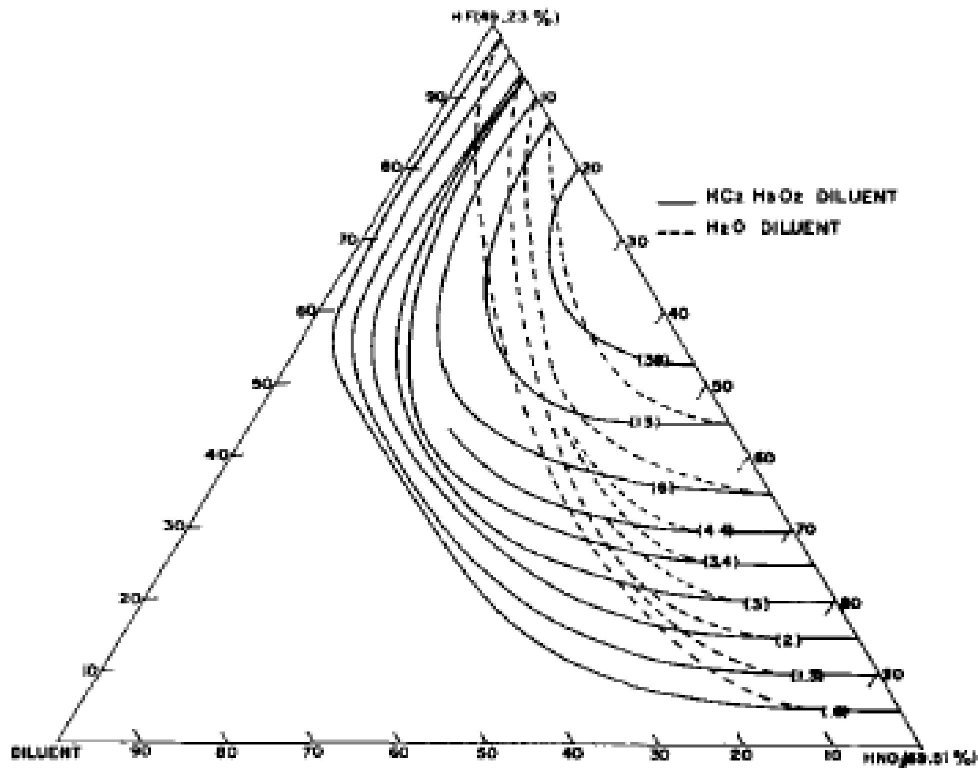

Fig. 1.8 Constant rate of change of die thickness as a function of the etchant composition

1.4.2. Dry etch

1.4.2.1. Introduction

The main three dry etching methods are [61] high pressure plasma etching, reactive ion etching (RIE), and ion milling. Ion milling employs accelerated ions like Ar+ that strike the surface to remove the material. It has a low etch rate (few nm/min) and poor selectivity and is used to etch thin layers that cannot be etched by RIE. High pressure plasma etching is the use of highly reactive species to react/etch the material. However, the most widely used etching technique is the RIE (ion assisted chemical etching), which involves a combination of physical and chemical etching.

Dry plasma etches [62 63 64 65 66 67] were introduced to nanofabrication in the 1970s. Plasma is the fourth state of matter; it is an ionic state of the gas. Strong electric fields can ionize the gas, usually a noble gas like

argon or a halogen, to free electrons from the gas atoms. DC electric fields produce DC plasma, while radiofrequency (RF) electric fields produce RF plasma. Fig 1.9 shows the schematic of the plasma structure.

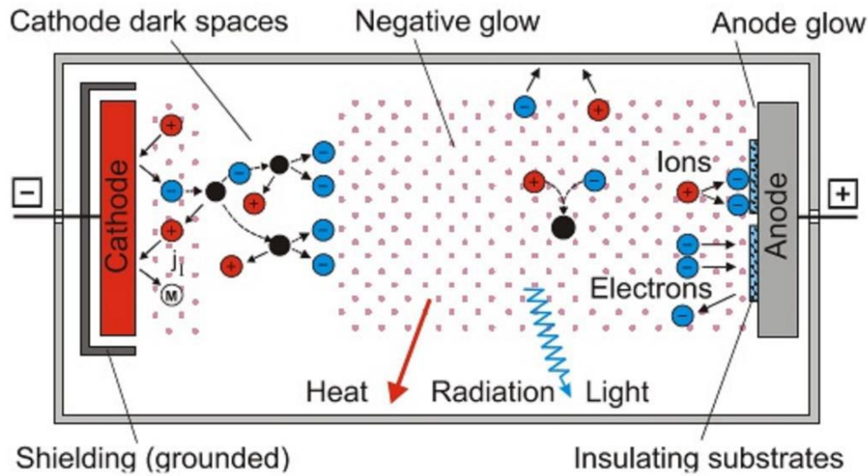

Fig 1.9 Schematic of the plasma structure [68]

The sputtering etching is a purely physical and highly directional etch, which occurs when no reactive chemical is added to the plasma. The accelerated ions move toward the wafer surface and knock off the materials. Selectivity is poor in sputtering etch and the process is inefficient and time consuming. To improve it, an assisted chemical etches (reactive ion etches (RIE)) is added. RIE process can be roughly divided into four steps, as shown in Fig 1.10. First, neutral radicals and ions are generated in the plasma, and then they are transported and get absorbed on the surface to chemically react with the wafer. Finally, a by product is produced and the etch is complete. The ion bombardment can help the etching by damaging the surface to render it more reactive or removing the residue formed inhibitors such as fluorocarbon polymer that may otherwise block the chemical etching.

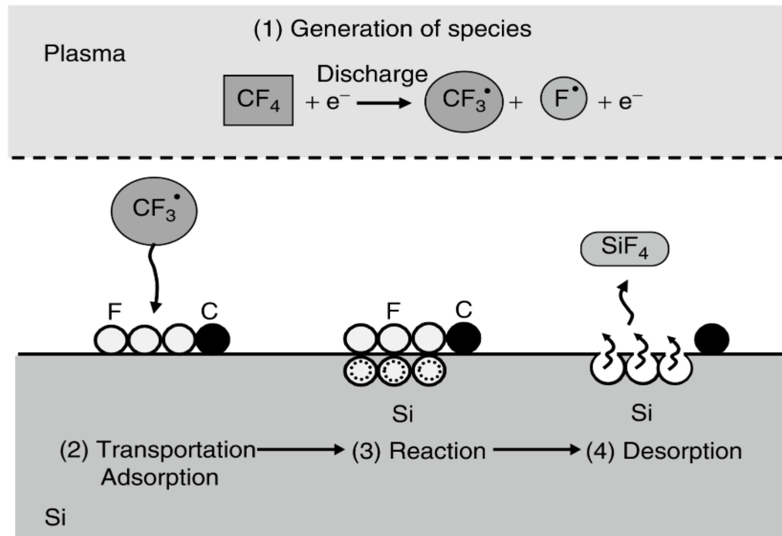

Fig 1.10 RIE etch steps [69] [70]

Compared to the conventional parallel plate (capacitively coupled plasma), inductively coupled plasma (ICP) greatly enhances the plasma density [71] [72] [73] [74] [75] [76]. As shown in Fig 1.11, ICP utilizes a coil to generate the plasma. High frequency RF power is applied to the coil, generating an AC magnetic field that induces a circular electric field to accelerate the electrons. As the electrons move in a circular path, they will not get quickly lost into the chamber walls. Instead, they are more efficient to collide with gas molecules and ionize them. In a typical ICP RIE setup, the ICP source controls the number of ions and free radicals whereas the lower bias RF power controls the ion energy.

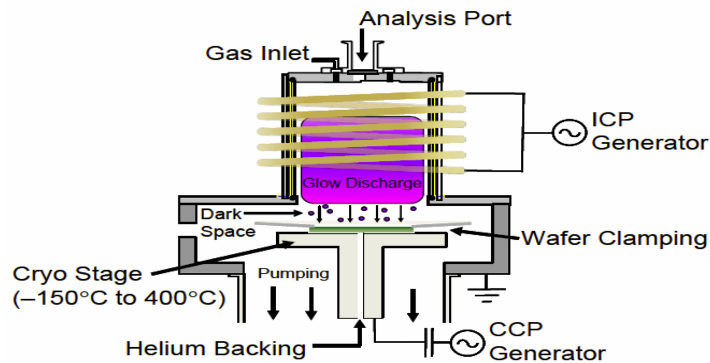

Fig 1.11 Cross sectional of Oxford Instruments ICP RIE [77]

1.4.2.2. Deep RIE (DRIE) of silicon processes

DRIE has two basic techniques which are Bosch and cryo-processes. Bosch process is known as "switched process" or "time domain multiplexed process." Both processors use fluorine-based plasma chemistry because of superior etch rates and high mask selectivity. The most popular hard mask used in the process is shown in Table 1.3[78].

Table 1.3 Hard mask materials and their deposition and patterning techniques

Material	Deposition	Patterning	Application
SiO_2	(PECVD) thermal oxidation	HF (wet), CHF_3 plasma (dry)	Deep etching, high-temperature etching
Al	Sputtering evaporation	H_3PO_4 (wet) Cl_2, plasma (dry)	Extremely high selectivity process
Al_2O_3	Sputtering ALD	HF (wet), SF_6 plasma (dry)	Extremely high selectivity process
Cr	Sputtering	$HClO_4/Ce(NH_4)_2(NO_3)_5$ (wet)	Extremely high selectivity process
Ni	Plating	Patterned plating	Quartz etching

1.4.2.2.1. Bosch process

Bosch process is an anisotropic deep silicon etching process that enables trench, hole, and pillar fabrication on various device applications. The Bosch process is a high aspect ratio plasma etching process. This process consists of cyclic isotropic etching (etching half cycle) and fluorocarbon-based protection film deposition (passivation half cycle). Passivation and etching gases are separately and alternately introduced to the chamber to form a high-density plasma, which is repeatedly done in a loop until the required depth is achieved.

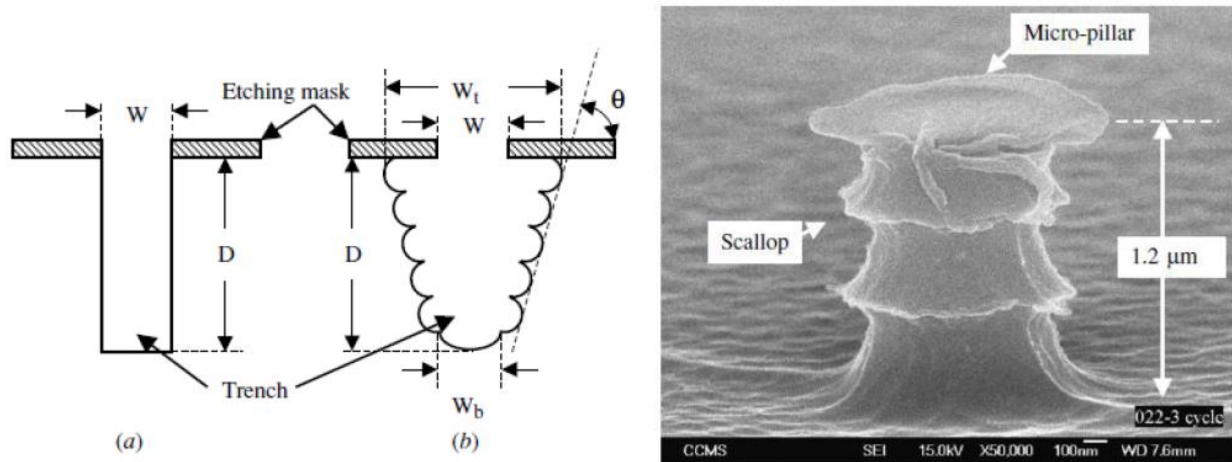

Fig 1.12 (left) (a) Ideal profile (b) real profile employing Bosch process. (right) SEM image of a pillar etched by Bosch process[79]

In a typical Bosch process, the SF_6 plasma cycle etches silicon, and the C_4F_8 plasma creates a protective layer during the passivation half cycle. To achieve deep silicon etching with a high aspect ratio, both the SF_6 plasma cycle and the C_4F_8 plasma cycle must be optimized. The protection film must be thick enough to protect the sidewall from the SF_6 plasma cycle which delivers a highly isotropic silicon etching. Since the Bosch process consists of cyclic isotropic etching and protection film deposition by quick gas switching, the sidewall is wavy and not smooth as shown in Fig 1.12, and for some applications, the rough sidewall is very undesirable. Table 1.4 shows typical etching parameters for the "Bosch process" using different ICP configurations.

There is another version of the Bosch process called pseudo-Bosch or non switching Bosch, where the two gases are introduced together into the chamber without switching. Bosch process (switching between the two cycles) leads to a rough and wavy sidewall profile while non switching gives a smooth sidewall, but the trade off is the lower etching rate and lower selectivity than regular Bosch.

For deep trench/hole etching, J. Yeom et al. [80] proves that the maximum achievable aspect ratio (critical aspect ratio) depends on the micro loading effect, which is the total exposed area during the RIE etching.

The loading effect is the variation of the etch rate depending on pattern density due to reactant depletion; the etch rate decreases when the surrounding load (etched area) increases. If the loading effect and aspect ratio dependent etch (ARDE) occur together, the investigation becomes more difficult.

Table 1.4 Typical settings for "Bosch process" using different ICP configurations

Parameters	Standard Configuration	High-Rate Configuration	High-Rate Configuration and "Ultrafast Switching"
ICP power	800 W	2700W	2700W
CCP power	8W	10W	10W
SF_6 flow	130sccm	500sccm	500sccm
Etch cycle time	7s	10s	1.6s
Etch cycle pressure	5Pa	9Pa	9Pa
C_4F_8 flow	100 sccm	200sccm	25sccm
Dep. Cycle presure	2.5Pa	4Pa	-
Dep. Cycle time	5s	5s	0.2s
Net etching rate (for wide trenches)	3µm/min	9µm/min	8µm/min
Selectivity PR:Si	40:1	140:1	120:1
Selectivity SiO_2:Si	100:1	300:1	300:1
Open Si area on 6 in.	15%	15%	15%

1.4.2.2.2. Cryogenic DRIE

Cryogenic RIE utilizes a minimum temperature of around -80 °C. It is discovered in 1988 when it was observed that the cooling of the silicon wafer during the RIE resulted in dramatically reduced etch rate on the sidewalls which improved the anisotropy [81]. Besides, selectivity between silicon and masking is improved at cryogenic temperatures [82 83]. Liquid nitrogen is used to cool down the chuck and the chuck temperature which is controlled by a proportional-integral-derivative (PID) controller. Fig 1.13[84] shows the schematic chemical and physical mechanisms for silicon cryo-etching. Reduced chemical reaction on the sidewall is due to the silicon oxyfluoride (SiO_xF_y) layer formed during the cryogenic etching process in SF_6/O_2 plasma. Cold temperature also reduces the reaction of free radicals due to the Arrhenius rate law

which improves anisotropy and/or etching selectivity. SiO_2 is the elected mask because of its very high selectivity (selectivity of 750 can be achieved) and low contamination. In the cryo-process, the sidewall is smooth, but the etch rate of silicon is lower than that in the Bosch process.

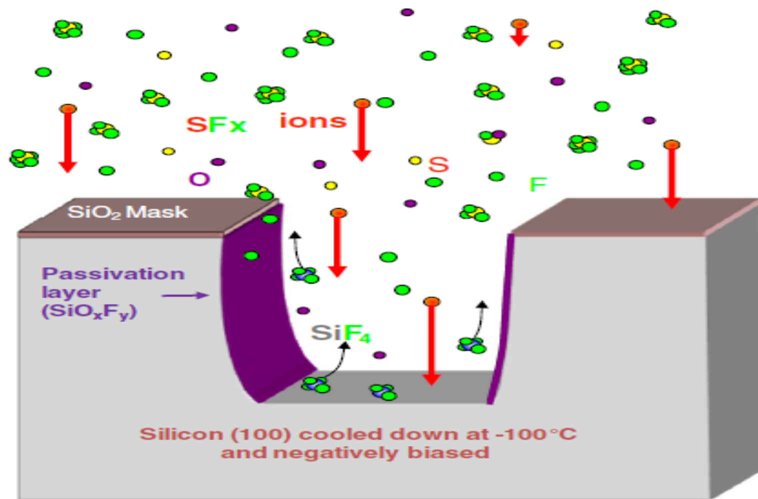

Fig 1.13 Cryo-etching physical and chemical mechanisms

A high concentration of fluorine radicals provides a high etch rate in SF_6/O_2 plasma. Oxygen controls the quality of the sidewall passivation layer, and it is the most important parameter when optimizing the sidewall slope. If oxygen flow is too low, an undercut profile will occur, whereas too high oxygen results in high passivation and silicon grass (known as black silicon).

Fig1.14 [85] demonstrates that when the temperature is increased, the silicon etches rate increases while the photoresist etches rate decreases. Temperature below −90 °C results in anisotropy without mask undercut, as lateral etch is reduced by sidewall passivation. The etch profile is mainly controlled by the temperature and oxygen flow rate. Low oxygen flow results in reduced passivation and enhances isotropic etch, whereas high oxygen flow may lead to a "pinch off" of the trench or hole when the formation of oxide at the trench bottom causes a narrowing of the trench. Temperature reduction introduces more passivation and may improve the profile. An increase in bias power or decrease in pressure can make the sidewall profile more

vertical. Increasing the oxygen flow rate will decrease the etch rate and the fluorine/oxygen ratio can modify the etch profile from a positive to a negative taper.

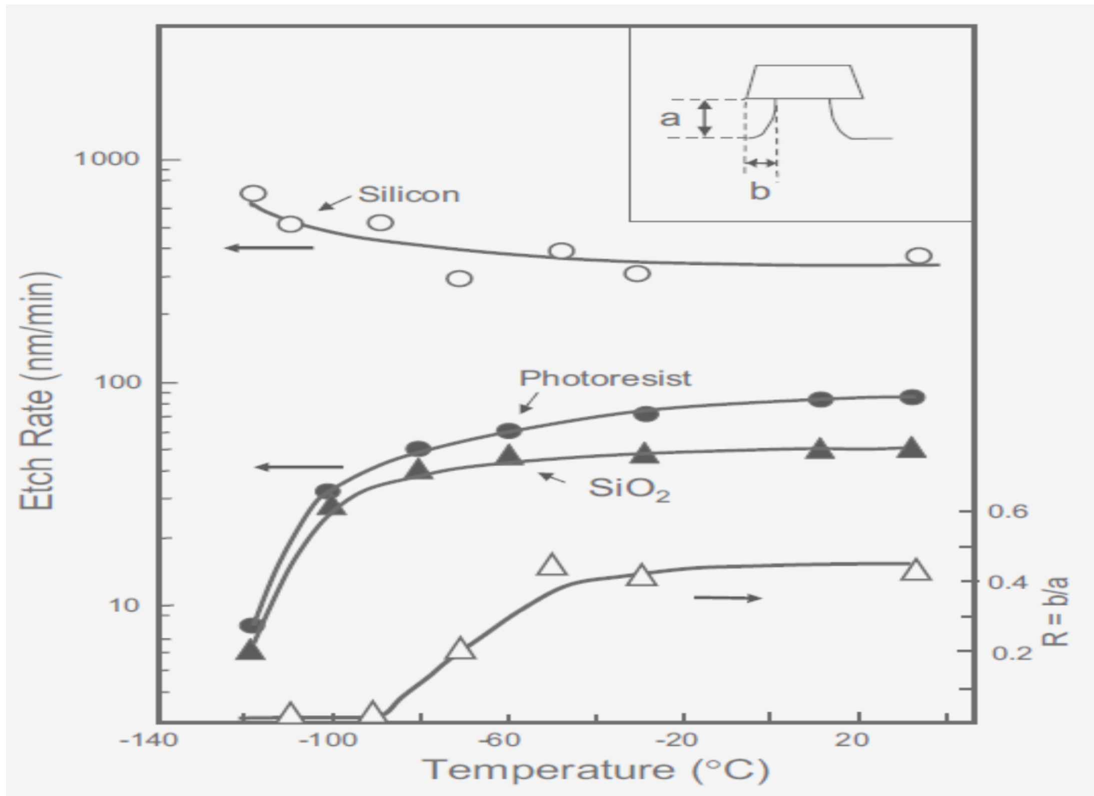

Fig 1.14 Cryogenic processes etch characteristics

As an example of the cryogenic etching process, P. Doll et al. [86] employed an Oxford Plasmalab 100/ICP 380 system with the recipe of -110 °C temperature, gas mixture of 20 sccm SF_6, 10 sccm O_2 and 10 sccm Ar, 750W ICP and 100W RF power to achieve an etch rate of ~20 nm s^{-1}. They fabricated 100, 50, and 20 nm pillar arrays using electron beam lithography and HSQ (a negative high-resolution e-beam resist) as a mask and obtained silicon nanopillars with an aspect ratio of 5 to 10.

Another three different processes are presented in Table 1.5. All these processes utilize temperatures around -100 °C and have similar process pressures, but the gas flows and RF powers are different. ICP power and SF_6 flow determine the etch rate, whereas the oxygen flow rate controls the passivation layer quality that affects the sidewall angle and undercuts, which is close to - 90° in all three processes.

Table 1.5 Typical process parameters of the Cryo-DRIE process that results in vertical sidewalls

Parameters	Process 1	Process 2	Process 3
ICP power (W)	1000	600	1200
CCP power (W)	2	2	(-80V bias)
O_2 flow rate (sccm)	6	2	8
SF_6 flow rate (sccm)	40	200	80
Pressure (mTorr)	10	14	13
Temperature (°C)	-110	-110	-90

1.5. Focus ion beam (FIB)

1.5.1. Introduction

Focused ion beam (FIB) [87] [88] is one of the most important tools for nanofabrication. The first FIB [89] [90] [91] [92] [93] [94] [95] [96] [97] [98] [99] [100] used gas field ionization sources (GFISs) and the field emission technology, and it was developed in 1975 by Levi Setti, Orloff, and Swanson. Today Ga FIB is far more popular, and the first Ga FIB was constructed in 1978 by Seliger et al. Ga FIB employs a liquid metal ion source (LMIS) to produce ions. Gallium is widely used to produce ions due to its low melting point, high mass, low volatility, and distinguishability from other materials. The ions are field evaporated and are concentrated into a narrow beam by an electrostatic lens, then passed through apertures before scanning the sample. The collisions caused by the ions hitting the sample and removing the surface atoms. This process is known as sputtering. The collisions also result in secondary electrons and secondary ions which can be collected and amplified to form the image. FIB uses low beam currents for imaging or high beam currents for sputtering or milling.

1.5.2. FIB construction

The construction of FIB is shown in Fig 1.15 which is similar to SEM components except for the ion/electron source. The Liquid metal ion source (LIMS)[101], shown in Fig 1.16, provides the ion beam. Other differences between SEM and FIB are listed below in Table 1.6.

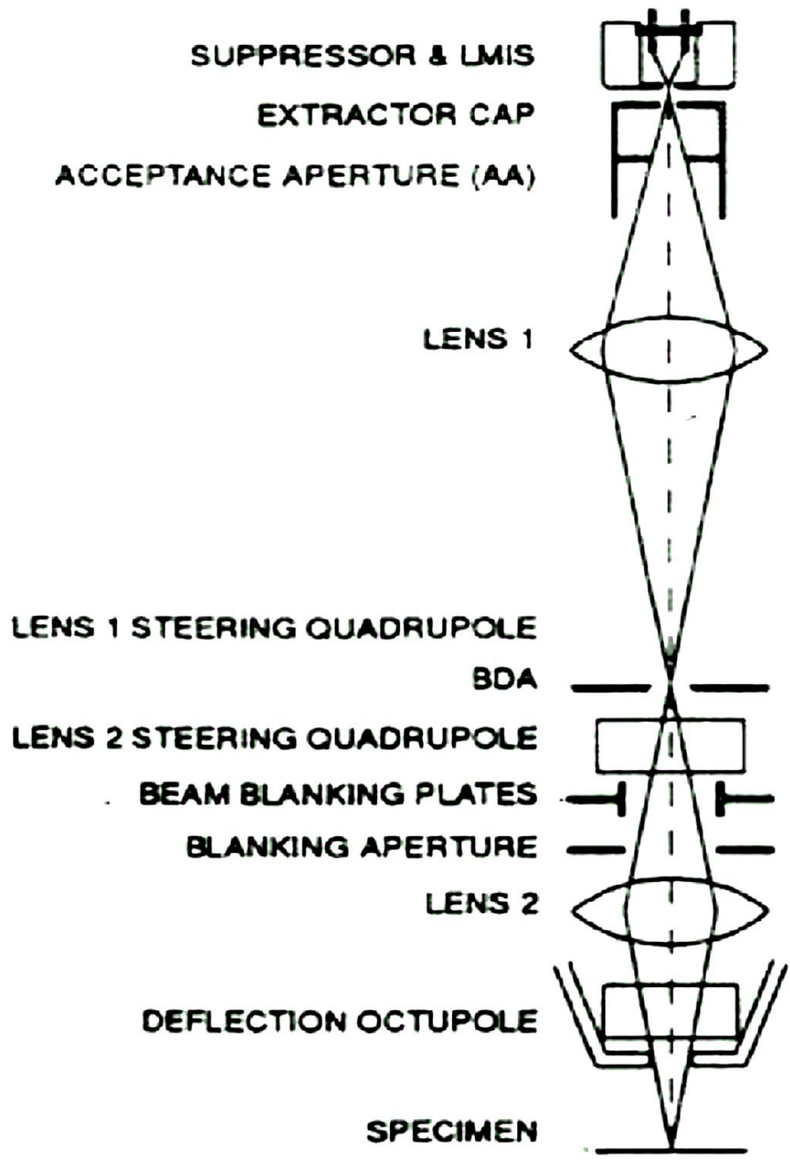

Fig 1.15 FIB construction [102]

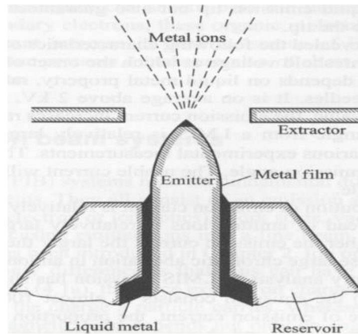

Fig 1.16 Liquid metal ion source (LIMS)

Table 1.6 The main differences between SEM and FIB [103]

Particle	FIB	SEM	Ratio
Type	Ga+ ion	Electron	
Elementary charge	+1	-1	
Particle size	0.2 nm	0.00001 nm	20000
Mass	$1.2x10^{-25}$ kg	$9.1x10^{-31}$ kg	130000
Velocity at 30 kV	$2.8x10^{5}$ m/s	$1.0x10^{8}$ m/s	0.0028
Velocity at 2 kV	$7.3x10^{4}$ m/s	$2.6x10^{7}$ m/s	0.0028
Velocity at 1 kV	$5.2x10^{4}$ m/s	$1.8x10^{7}$ m/s	0.0028
Momentum at 30 kV	$3.4x10^{-20}$ kgm/s	$9.1x10^{-23}$ kgm/s	370
Momentum at 2 kV	$8.8x10^{-21}$ kgm/s	$2.4x10^{-23}$ kgm/s	370
Momentum at 1 kV	$6.2x10^{-21}$ kgm/s	$1.6x10^{-23}$ kgm/s	370
Beam			
Size	nm range	nm range	
Energy	up to 30 kV	up to 30 kV	-
Current	pA to nA	pA to µA range	-
Penetration depth			
In polymer at 30 kV	60 nm	12000 nm	0.005
In polymer at 30 kV	12 nm	100 nm	0.12
In iron at 30 kV	20 nm	1800 nm	0.11
In iron at 2 kV	4 nm	25 nm	0.16
Average signal per 100 particles at 20 kV			
Secondary electrons	100 – 200	50 – 75	1.33 - 4.0
Backscattered electron	0	30 – 50	0
Substrate atom	500	0	infinite
Secondary ion	30	0	infinite
X-ray	0	0.7	0

1.5.3. FIB utilization

FIB[104] is utilized in nanofabrication in many techniques. When Ga ions bombarded with the surface of a solid sample, they lose energy to the solid. The effects of the incident ions on the substrate are either removal of the material by sputtering/milling, deposition implantation, or imaging by secondary electron emission effect, as demonstrated in Fig 1.17.

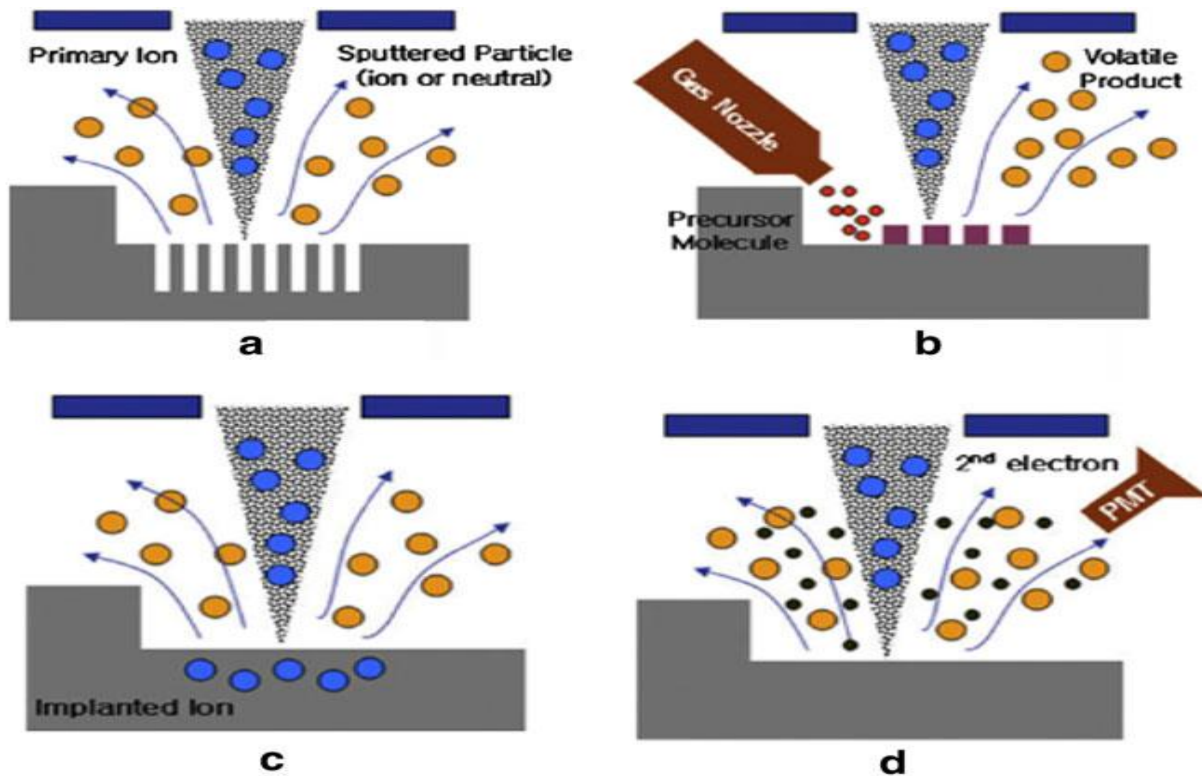

Fig 1.17 Principle of FIB utilization; (a) milling, (b) deposition, (c) implantation, (d) imaging

Many parameters influence the outcome of the FIB include but not limited to sputter yield, acceleration voltage, beam current, dwell time, the effect of raster and serpentine scan modes, pixel spacing, and pattern size. Table 1.7 summarises some of the FIB parameters and the possible effects that may occur.

Table 1.7 The FIB parameters and their possible effects

Parameter	Effect	
	Increase	Decrease
Sputter yield	Milling depth increases, low re-deposition effect (Fu et al. 2000; Lugstein et al. 2003)	Milling depth decrease, high re-deposition effect
Acceleration voltage	Fast milling, damages occur (amorphisation and implantation) (Rajsiri et al. 2002)	Slow milling, reduce damage (Einsle et al. 2011)
Beam current	Fast milling, good for lower quality of milling (Yao 2005)	Slow milling, good for fine polishing, produce finer quality of channel with increasing the number of serpentine scan (Tseng 2004)
Dwell time	Suitable for small structures (vias), high aspect ratio, re-deposition occur (Chantngarm 2008)	Require long milling time, low aspect ratio, reduce re-deposition and improved detection accuracy (Kim et al. 2008)
Pixel spacing	Larger value than 8 nm is able to mill an array of holes (Tseng 2004)	Smaller value than 1.5 nm for smooth profile (Maas et al. 2010)
Pattern size	Long dwell time required [dwell time α radius (r)] (Kim et al. 2008)	Rough damage, hole not uniform in width (Nellen and Bronnimann 2006)
Scan mode	Raster—continuously re-deposited, suitable for V-shaped channels (Tseng et al. 2004)	
	Serpentine—reduce re-deposition, suitable for high aspect ratio structures (Nellen et al. 2006)	
Milling mode	Bitmap—direct write, difficult to fabricate holes <100 nm in large area (Fu and Bryan 2005)	
	Pixel space—mill one by one, can fabricate holes <100 nm in large area (Atiqah et al. 2012)	

1.6. Atomic force microscope (AFM)

1.6.1. Introduction

Nanoscience is boosted [105] in 1980s by the invention of the scanning tunneling microscope (STM) [106], which can provide an image of the surfaces at the atomic level. Gerd Binnig and Heinrich Rohrer at IBM Zurich research laboratory invented STM in 1981. They were awarded the Nobel Prize in Physics in 1986 [107]. The first commercially available STM was accessible in 1989. Later STM became part of a family of instruments based on the scanning probe microscope (SPM), developed to measure the electrical [108] [109] [110], physical [111] [112] [113], chemical [114] [115] [116], or thermal [117] [118] [119] [120] [121] properties of the surface, based on the modification done on the basic SPM.

1.6.1.1. Microscope families

The growing need for surface examination on the nanoscale makes the atomic force microscope (AFM) one of the most important tools because of its ability to characterize surfaces of metals and semiconductors in real space at the atomic scale [122] [123] [124] [125] [126] [127] [128]. The basics of AFM are, measuring the force between

its sharp tip and the examined surface. That leads to a wide range of other devices based on the same idea such as STM, magnetic force microscope (MFM), dipping force microscope (DFM), friction force microscope (FFM), and electrostatic force microscope (EFM). There is also a tendency to combine more than one device such as STM/AFM, AFM/MFM, and AFM/EFM. Table 1.8 shows the most familiar SPM techniques used by its families. It is important to mention that Atomic Force Microscope (AFM) is the most widely used among these microscopes.

Table 1.8 The most familiar SPM techniques and families [129]

Abbrev.	Technique	Interaction type	Usage
STM	Scanning Tunneling Microscopy	Tunneling current	3-D topography: size, shape and periodicity of features, surface roughness. Electronic structure, and possible elemental identity
AFM	Atomic Force Microscopy	Interatomic and intermolecular forces	3-D topography: size and shape and periodicity of features, surface roughness.
FMM	Force Modulation Microscopy	Interatomic and intermolecular forces	Hardness and surface elasticity at various locations
LFM	Lateral Force Microscopy	Frictional forces	Differences of adhesiveness and friction at various locations.
MFM	Magnetic Force Microscopy	Magnetic forces	Size and shape of magnetic features. Strength and polarity of magnetic fields at different locations.
SThM	Scanning Thermal Microscopy	Heat transfer	Thermal conductivity differences between surface features.
EFM	Electrostatic Force Microscopy	Electrostatic forces	Electrostatic field gradients on the sample surface.
NSOM	Near-field Scanning Optical Microscopy	Reflection, absorption and Fluorescence of light	Optical properties of surface features

1.6.2. The basic principle of atomic force microscopy

In the absence of all forces, the forces between two atoms near each other is known intermolecular forces include but not limited to Van Der Waals force [130] [131] [132] [133] [134]. These forces are distance dependant on the molecular/atom level, and it vanishes quickly at a longer distance.

When an AFM tip is in contact with the object's surface, attractive force proportional to $1/r^6$ occurs. On the other hand, if the tip/object distance gets closer, the repulsive action of the force occurs, at the inverse

of twelfth power, as shown in the upper curve of Fig 1.18. In Fig 1.18, positive energy relates to repulsion, while negative energy to the attraction.

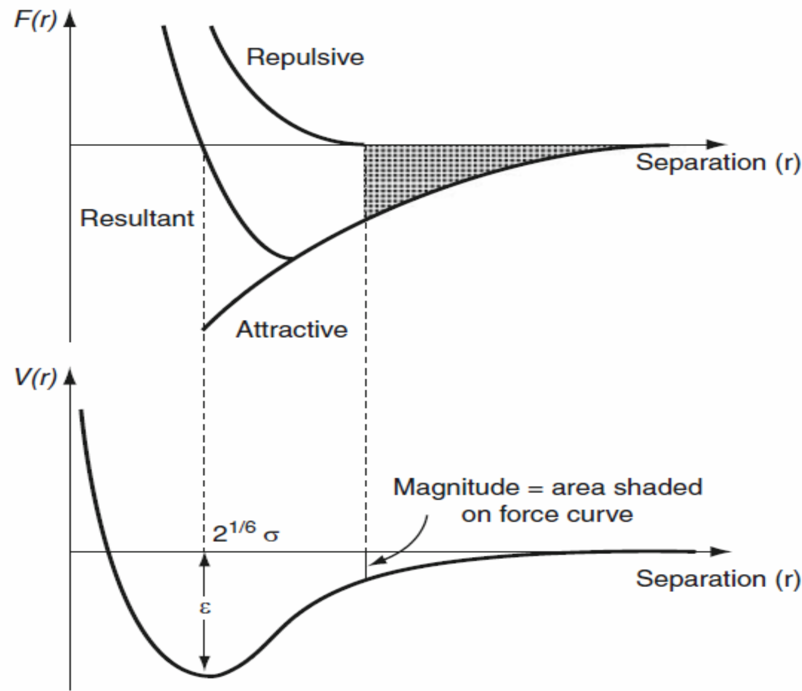

Fig 1.18 The intermolecular forces F(r) and the potential energy V(r) between two bodied, vs distance [135]

1.6.3. Construction of atomic force microscopy

As shown in Fig 1.19, AFM [136] [137] [138] [139] [140] [141] [142] employs a nanometer sharp tip located at the free end of a cantilever, which scans the object's surface. The tip bends the cantilever according to the surface topography. The cantilever bending is measured digitally by the reflection of a laser beam from the cantilever into a four-quadrant photodiode. A piezoelectric actuator is used to move the cantilever vertically providing information on the vertical topography of the scanned object. The scanned image is constructed by the piezoelectric actuator information including x-y-z movement.

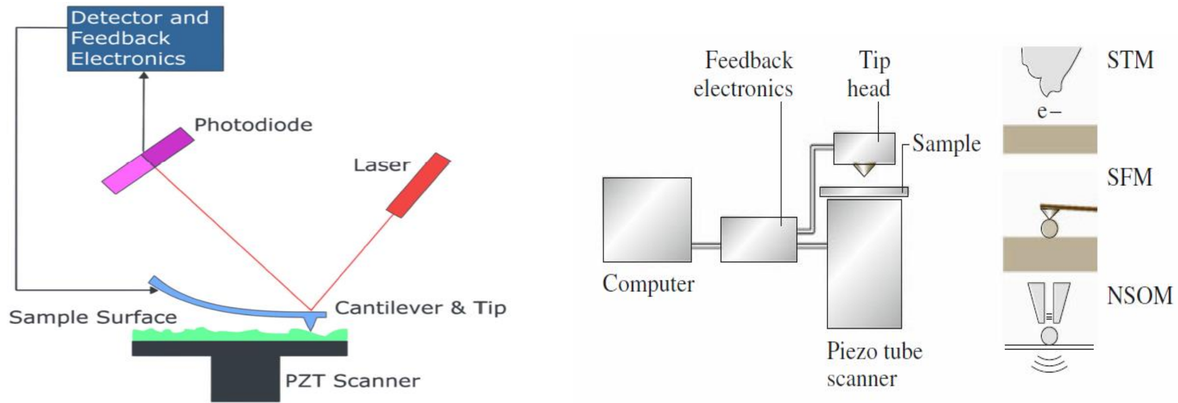

Fig 1.19 (left) Schematic of AFM construction[143],(right) AFM in block diagram [144]

1.7. Thesis structure

This thesis has seven chapters. The first two chapters cover the background review for this research. Chapter one discusses an overview of the nanofabrication techniques employed in this study. It covers evaporation, wet etch, dry etch using reactive ion etching (RIE), atomic layer deposition (ALD), focus ion beam (FIB), and atomic force microscope (AFM). Chapter two gives an overview of the AFM tip production techniques. It also reviews the different fabrication methods of the high aspect ratio (HAR) AFM tips.

The following four chapters present the experimental work for this research. Chapter three optimizes the batch fabrication process for edge and high aspect ratio (HAR) AFM tips. Chapter four demonstrates the AFM tip sharpening using oxidation which includes a study of the oxidation technique and its effect on AFM tip sharpening. Chapter five introduces the fabrication of ultra-high aspect ratio silicon nanopillars array by employing both dry and wet etch. Chapter six introduces the use of a focus ion beam (FIB) to produce HAR AFM tips and explores the ion implantation in both Ga and Au FIB to create HAR pillars. Lastly, chapter seven is the conclusion of this work.

Chapter 2

Introduction to AFM tip fabrication techniques

This chapter presents an overview of AFM tip fabrication methods to make different types of AFM probes focusing on high aspect ratio (HAR) tips.

2.1. Basics of AFM probes

2.1.1. AFM probe assembly

As shown in Fig 2.1, the AFM probe consists of a tip, cantilever, and holder.

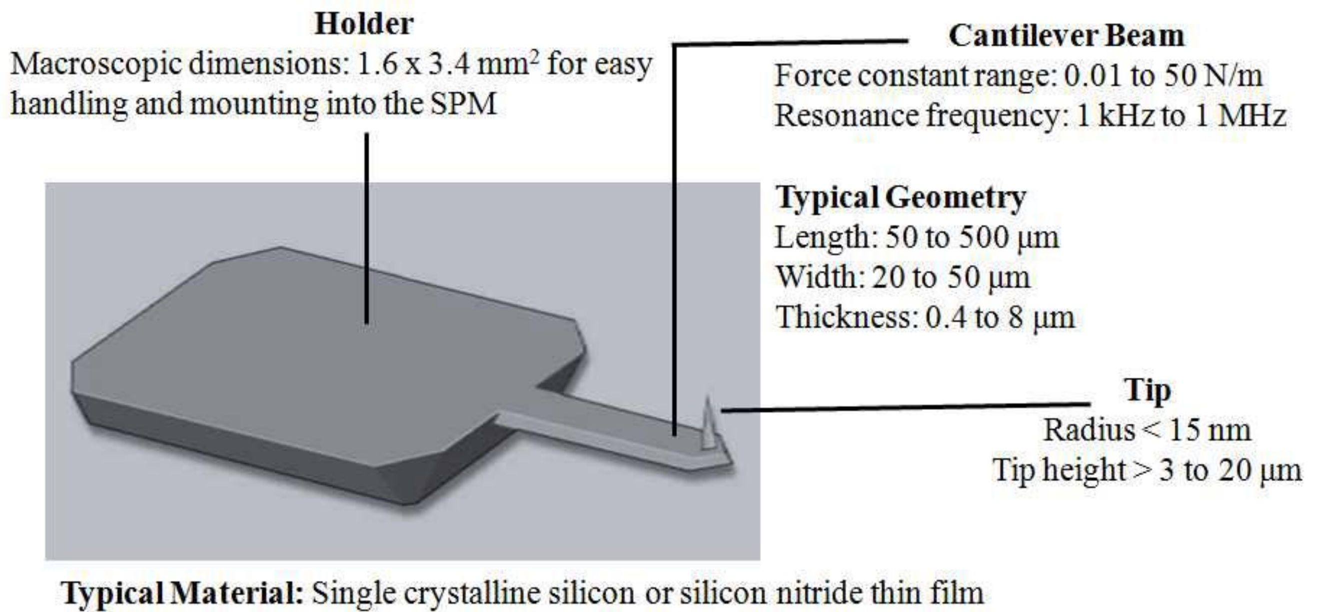

Fig 2.1 Schematic of AFM probe assembly [145]

2.1.2. AFM probe (tip) classification

There is a large variety of tip types [146] [147] [148] [149] [150] [151]. Every manufacturer tries to produce their own design with different aspects. The main two components are the tip and the cantilever. Tips can be classified

according to shape, materials, and coating. The cantilever properties include its shape, material, geometry, force constant and resonant frequency.

Typically, the tips have different heights in the range of 10-15 µm and different shapes [152 153 154 155 156]. The basic shape could be square, triangle, and circle as shown in Fig 2.2. The tip radius which is usually below 10 nm as shown in Fig 2.3, could be flat, round, ball-shaped, or spike-shape. The tip also can be tilted or rotated for better imaging as shown in Fig 2.4.

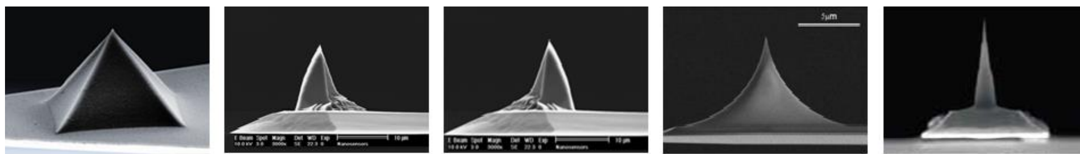

Fig 2.2 Different AFM tip apex

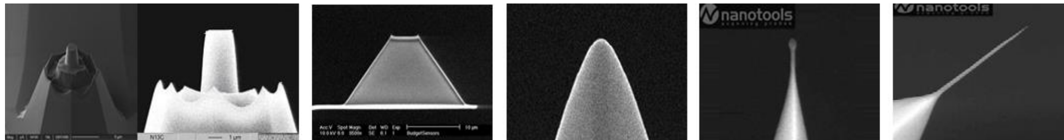

Fig 2.3 AFM tip apex shapes

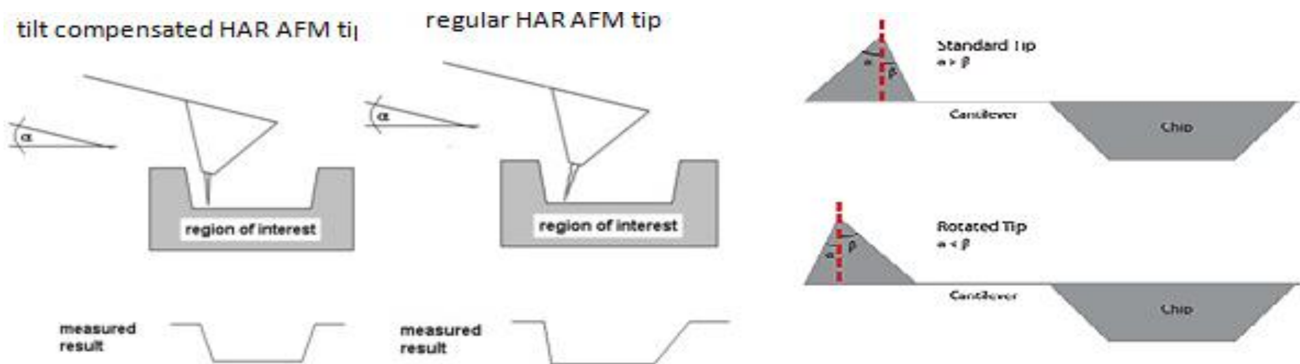

Fig 2.4 Tilt / regular / rotated HAR AFM tip

The AFM probe could be made of different materials including silicon, silicon nitrate, silicon oxide, high-density carbon, or quartz. Also, it can be uncoated or coated by gold, platinum, platinum/iridium, diamond-like carbon, diamond, conductive diamond, silicon nitrate, silicide, or cobalt alloy [157 158 159 160]. Finally, the probe can be on the edge of the cantilever as shown in Fig 2.5, which is referred to as the edge tip to help locate the scanned element directly, or high aspect ratio tip (aspect ratio = tip height/base width) to deliver a better resolution, as shown in Fig 2.6.

Fig 2.5 Edge AFM tips

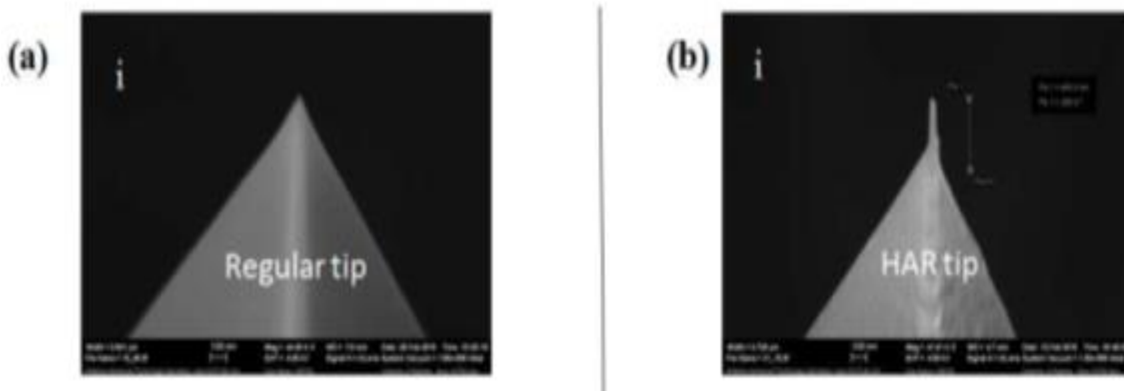

Fig 2.6 (a) Regular tip (b) HAR tip

2.1.3. Cantilever's classification

The mechanical properties of an AFM cantilever have typical ranges: force constant 0.06 to 50 N/m, resonance frequency 1 kHz to 1 MHz, length 100 to 600 µm, width 10 to 50 µm, thickness 0.5 to 8 µm. A thick and short AFM cantilever usually has a low resonance frequency and a high force constant, while a

long and thin AFM cantilever has a high resonance frequency and a low force constant. The material of the AFM cantilever can also control the spring constant and resonant frequency of the probe.

The cantilever shape [161] [162] [163] [164] [165] [166] can be rectangular or triangular as shown in Fig 2.7. Also, its cross-section can be different as shown in Fig 2.8. The tip assembly can contain one, two, three, four, or multiple cantilevers as shown in Fig 2.9. Cantilever material can be silicon or silicon nitride and it may be uncoated, backside coated with aluminum or gold to enhance the laser reflection, topside coated with gold to be electrically conductive, or overall coated with platinum, platinum/iridium, conductive diamond, or silicon to protect the cantilever from the environment of chemicals.

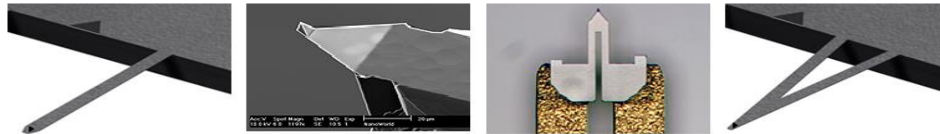

Fig 2.7 AFM cantilevers shapes

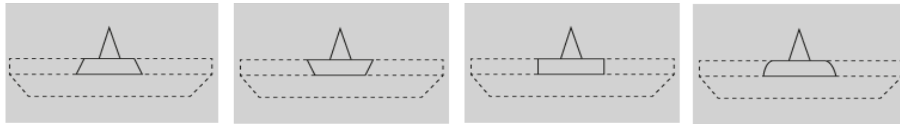

Fig 2.8 Different AFM cantilevers cross-section

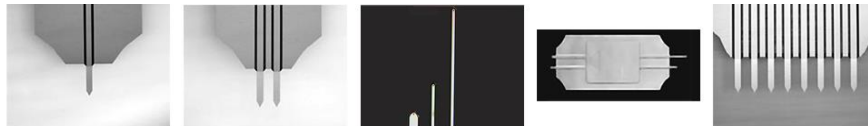

Fig 2.9 Number of AFM cantilevers per prob

2.1.4. Tip holder

Support chips are usually standardized to 3.4 X 1.6 mm with thicknesses of 315 or 500 µm as shown in Fig 2.10.

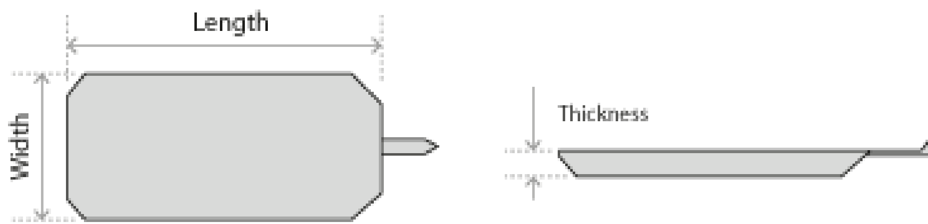

Fig 2.10 Support chip of AFM tip

2.2. AFM tip fabrication

2.2.1. Fabrication techniques of AFM probes

Generally, tip fabrication has two main methods: etching and molding, as shown in Fig 2.11. The etching method employs dry plasma etch or anisotropic KOH wet etch under the mask to create the tip pyramid or cone/pillar shape. The molding method consists of the deposition of the cantilever/tip material into a pre-patterned cavity having an inverse pyramid or cone-shape. The main advantage of the molding method is that the cantilever thickness is determined by the deposited film thickness that can be precisely controlled. Even though its thickness is well below 1μm, it is more utilized for contact mode or where a low force constant (achieved by the thin cantilever thickness) is needed such as in the peak force mode to image soft biomaterials.

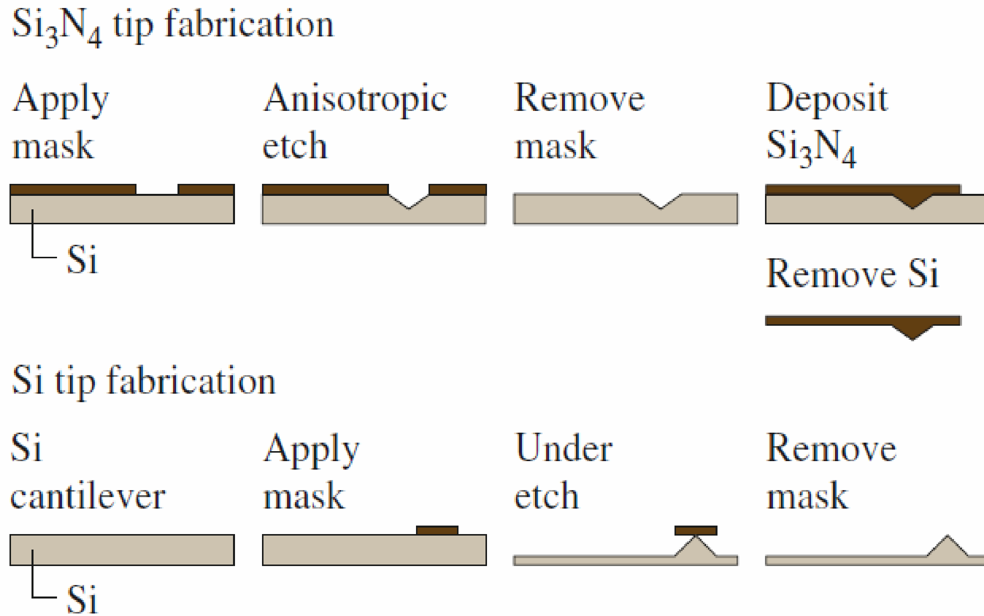

Fig 2.11 AFM tip fabrication using (top) molding method (bottom) etching method [167]

For the molding method, Albrecht et al. [168] created an inverse pyramid cavity tip by starting with a silicon wafer with a SiO_2 mask layer on the <100> silicon surface. They etched an array of small squares in the mask layer, then etched with an anisotropic etchant KOH creating a pyramidal cavity. The mask is then removed, and another mask was fabricated to define the cantilever. Using low pressure chemical vapor deposition (LPCVD), the wafer was coated with Si_3N_4 to fill the mold and create the tips. Finally, the removal of the silicon released the silicon nitride tips.

Takahashi et al. 2009 [169] demonstrated advanced fabrication techniques using the molding method (Fig 2.12). The process used a KOH solution to selectively etch the silicon then it is thermally oxidized and coated with copper. The growth of layers of graphene on copper occurred through CVD. Then it was coated with SU-8 resist where cantilever could be defined. Another thick SU-8 was used to create the tip body. Afterward, silicon was etched away by KOH, silicon dioxide by HF solution, Cu by a wet etchant, extra graphene by argon dry plasma etched, where the tip would be released.

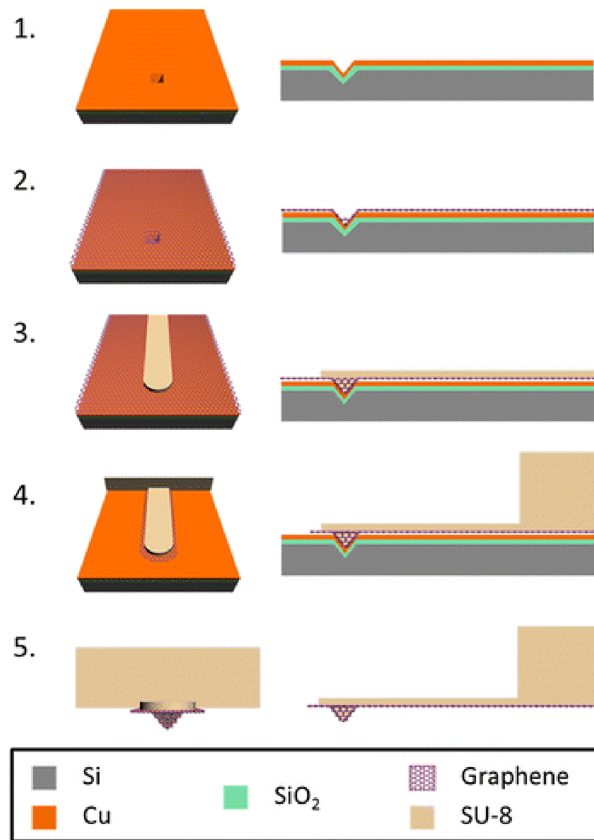

Fig 2.12 Advanced techniques for inverse pyramid cavity concept

For the etching method, Wolter et al. [170] created an undercut tip by starting with a silicon wafer with a SiO_2 mask layer on the <100> silicon surface, as the previous method. A small mask was created at the end of the cantilever. The mask was undercut etched using KOH and resulted in a pyramidal silicon tip.

On the other hand, Rocket tip fabrication [171] is shown in Fig 2.13. The process starts with a SOI (silicon on insulator) wafer. The top 15 µm thickness silicon layer undergoes thermal oxidation, then the photolithography technique is used to pattern a circular etch mask. Another photolithography technique is used to define the cantilever. DRIE is employed to create the cantilever, and wet oxidation at 1100 °C is used to sharpen the tip; then Si RIE is used to create the HAR pillar. Finally, the release of the cantilever is done by etching the silicon dioxide beneath the cantilever and holder.

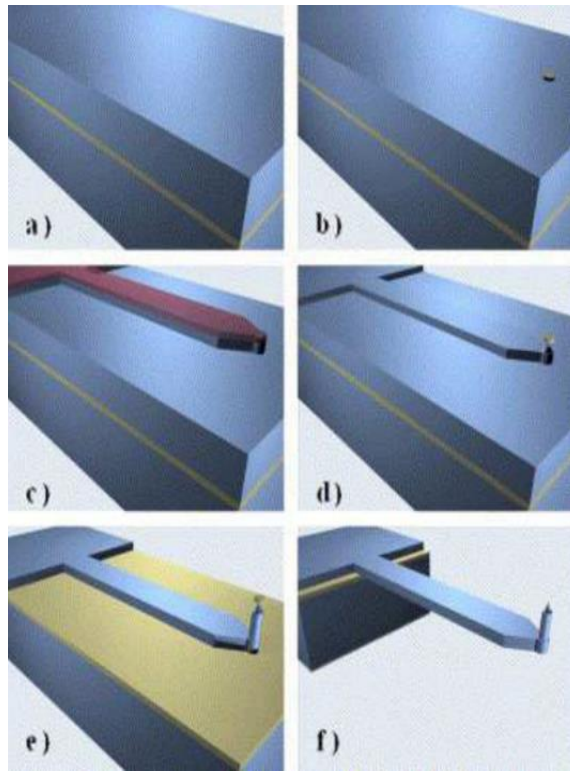

Fig 2.13 The process to fabricate the rocket tip

2.2.3. High aspect ratio (HAR) tips fabrication

The purpose of using the HAR tip is to obtain faithful topographical information across high aspect ratio structures for surface mapping, as shown in Fig 2.14.

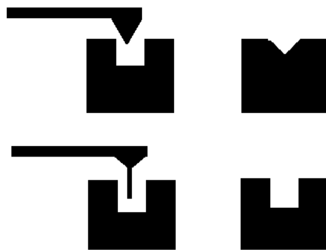

Fig 2.14 (top) Regular AFM tip and the scanned profile of a hole/trench, (bottom) HAR tip and its scanned profile

There are many methods to fabricate the HAR tips [172] [173] [174] [175], which include but are not limited to: focused ion beam milling, electron beam induced deposition, carbon nanotube attachment, "Nauga-needle formation" technique, and angle dependant dry etching. Fig 2.15 [176] shows several high aspect ratio tips which are currently available in the market where tips are fabricated with (a) focused ion beam milling, (b) electron beam induced deposition, (c) carbon nanotube attachment, (d) spike attachment, and (e) "Nauga-needle formation" technique.

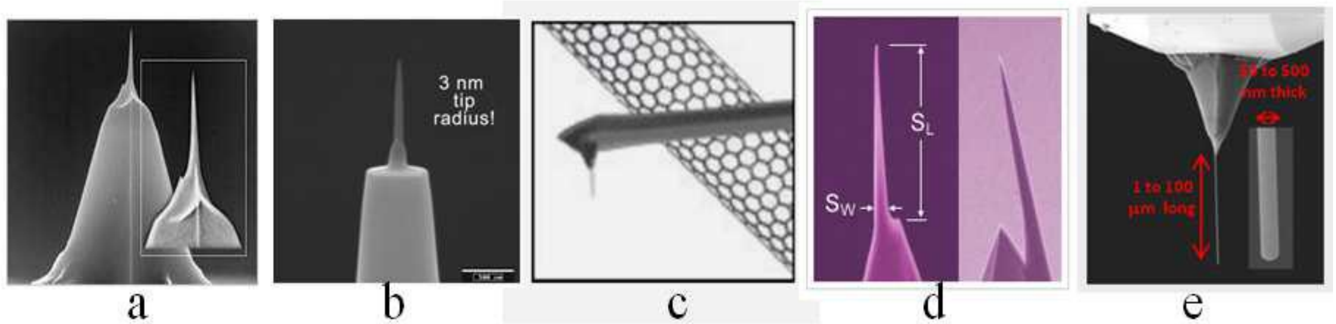

Fig 2.15 Commercial HAR tip examples where the tips are fabricated with (a) focused ion beam milling, (b) electron beam induced deposition, (c) carbon nanotube attachment, (d) spike attachment, and (e) "Nauga-needle formation" technique

2.2.3.1. Focused ion beam milling method

In this method, the focused ion beam is used to shape the tip and form a high aspect ratio pillar, up to 10:1 with a 5 nm radius [177]. The tip materials are milled to the required shape and size. A nitride tip example is shown in Fig 2.16.

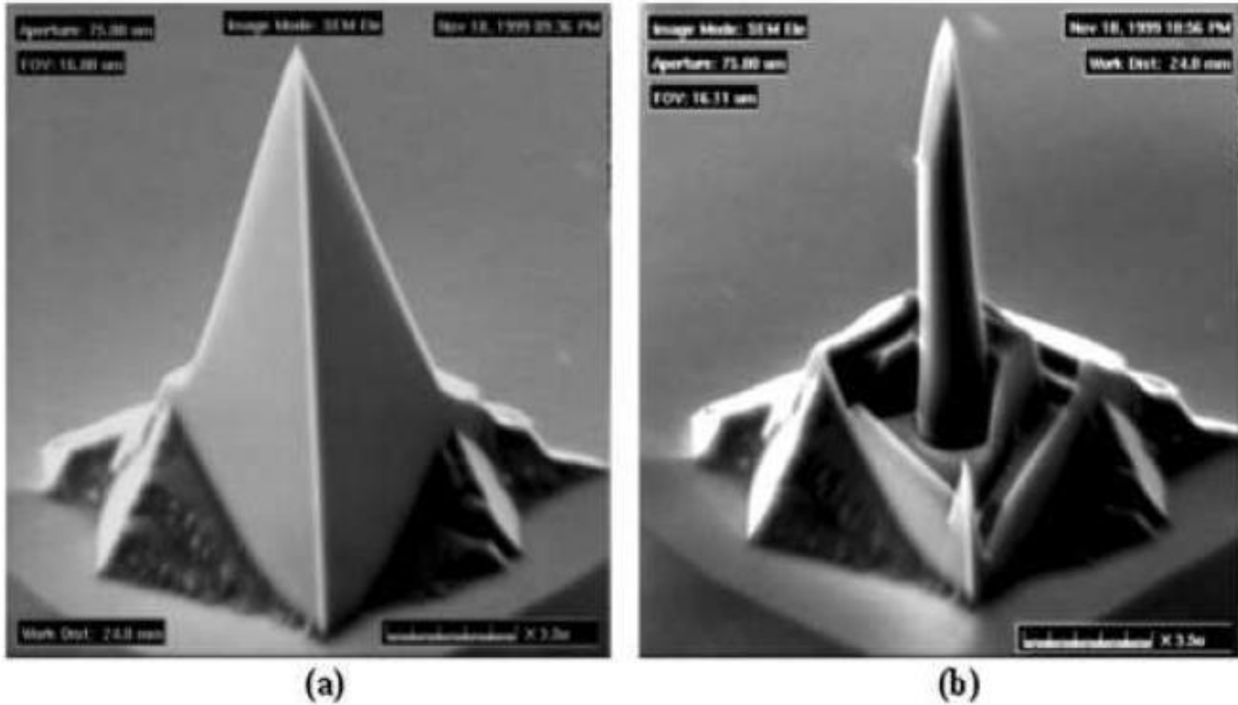

Fig 2.16 Nitride AFM tip before and after FIB milling

Also, Cockins et al. [178] established a technique to completely mill the original tip and drill a hole at any required angle, and glue a wire with the required length, diameter, and shape, as shown in Fig 2.17. The wire could be sharpened further to enhance the tip shape.

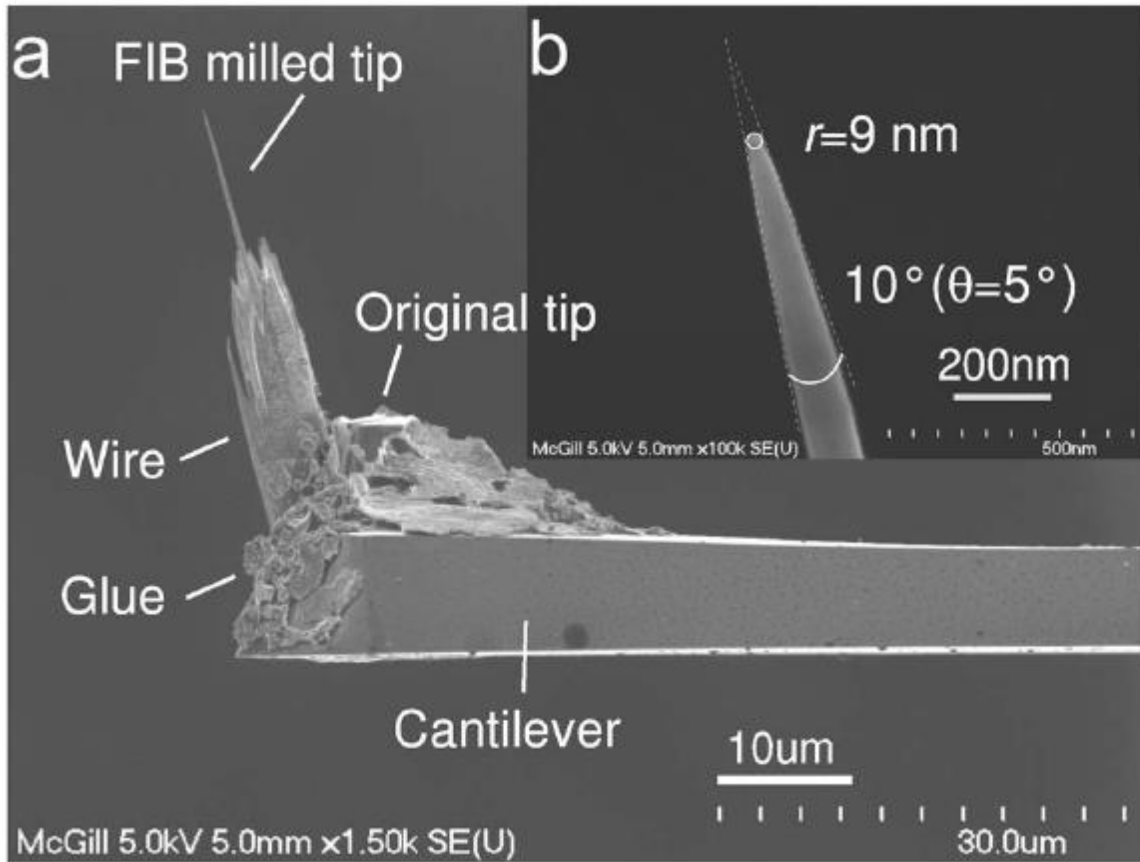

Fig 2.17 (a) A fabricated HAR tip, (b) achieved the radius of the tip

2.2.3.2. Electron/ion beam induced deposition (EBID/IBID) method

Electron/ion beam can be employed with precursor gas to produce a high aspect ratio tip. David et al. [179] fabricated a HAR tip by using Hitachi S-800 SEM tool equipped with $W(CO)_6$ organometallic precursor gas flow directly down the axis of the commercial pyramid shaped nitride tip (30 nm palladium gold coated) mounted on an aluminum stub. The SEM was switched into the spot where the beam was not in scanning mode for a particular exposure time to grow the carbon pillar at the end of the cantilever. The tip apex was approximately 30 nm in diameter and about 15° of cone angles and became cylindrical down the shank as shown in Fig 2.18.

To demonstrate the nanoneedle (by EBID method) height was tunable using different growth time, they started with a commercial pyramid shaped nitride tip with a 30 nm palladium gold coating and mounted on a regular aluminum stub, then grew the carbon pillar at the end of the cantilever by EBID. The longer the exposure time, the longer the tip pillar. Fig 2.19 shows the pillar size under different growth times using EBID [180]. However, this process is expensive and time-consuming (as the tips are individually fabricated) on large scale production.

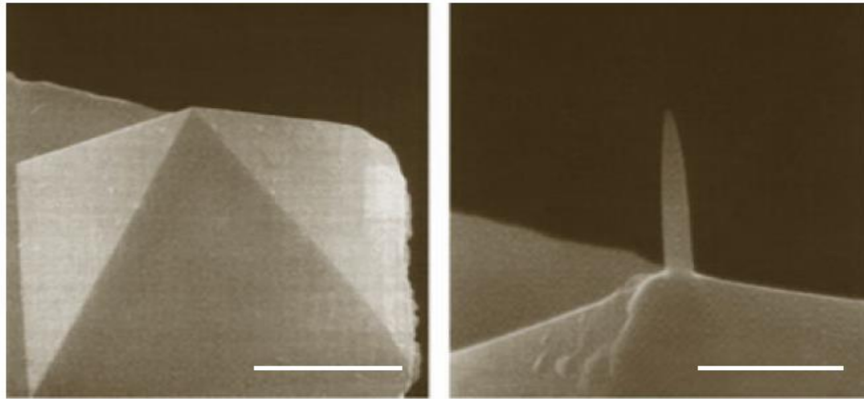

Fig 2.18 Pyramidal nitride tip before and after depositing a carbon pillar on its apex

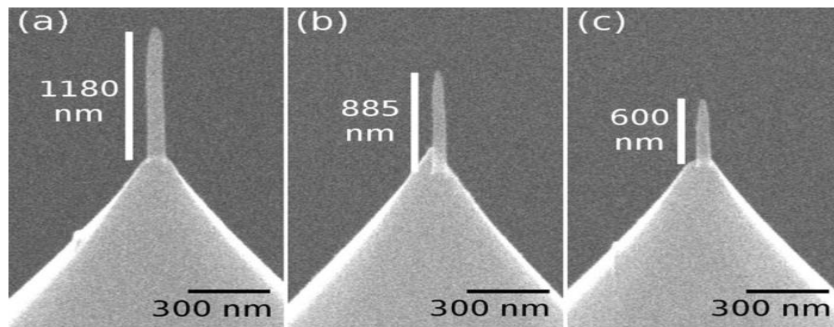

Fig 2.19 Needle height as a function of carbon deposition time, (a) 20 s. (b) 10 s. (c) 5 s

2.2.3.3. Carbon Nanotube (CNT) attachment method

Carbon nanotube tips are prepared by either attaching them or growing them at the apex of ordinary tips, [181 182 183 184 185]. The carbon nanotube has an extremely high aspect ratio and a remarkably long lifetime; it

could be ~20 times longer than the regular silicon AFM tip [186 187]. The challenge is to attach or grow a carbon nanotube in the right position, direction, and length. In practice, these tips with cantilever are often damaged during the handling process rather than being worn out after long continuous scanning.

Woolley et al. [188] introduced the CVD growth carbon nanotube tip, while Ye et al.[189] established plasma enhanced CVD directional growth of nanotube tips. Hafner et al. [190] demonstrated that carbon nanotube could be picked up by the tip coated with a thin layer of UV-cure adhesive material.

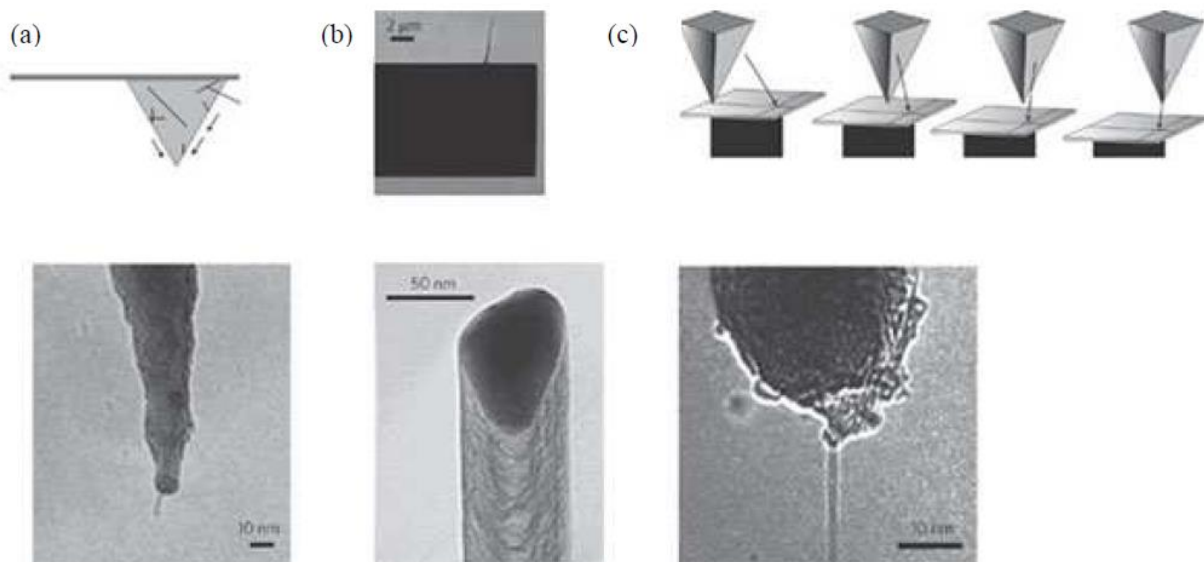

Fig 2.20 (a) Surface growth CVD nanotube tip (b) single CNT attached on cantilever produce by directional growth plasma enhanced CVD (c) Nanotube attachment method through 'pick-up', (bottom) shows the TEM image of a SWNT (single walled nanotube) tip

The top and bottom images of Fig 2.20 (a) show surface growth CVD nanotube tip, Fig 2.20 (b) top and the bottom shows a single carbon nanotube attached to a cantilever using directional-growth plasma-enhanced CVD and Fig 2.20 (c), top and bottom show a pick-up nanotube attachment tip.

2.2.3.4. "Nauga-needle formation" method

This technique is commercialized by Nauga-needle Inc[191], and it starts with a regular AFM tip coated with silver (Ag), and then it is dipped into melted gallium (Ga) and pulled out slowly to form a solid Ag/Ga alloy crystallized nanowire attached to the tip. Fig 2.21 [192] demonstrates the schematic and the corresponding SEM images for this process. However, the tip apex fabricated by this method is blunt as the nanowire (formed with solid Ag/Ga alloy) diameter is large (~50nm).

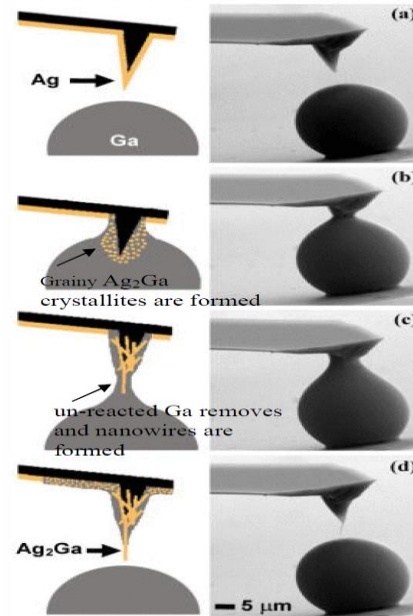

Fig 2.21 Nauga-needle fabrication steps, schematic drawing, and corresponding SEM images

2.2.3.5. Angle dependant dry etching method

The process relies on the fact that the etching/milling rate by ion bombardment is higher at a tilted ion incident angle than at a normal (perpendicular) incident angle, as shown in Fig 2.22[193]. The fabrication steps are shown in Fig 2.23, where a regular pyramid-shaped AFM tip is coated with a thin layer of a metal film of either Al, Cr, or Ti then etched using Ar ion milling, BCl_3, or Cl_2 gas plasma, depending on the metal deposited over the top surface. Because of the angle dependant etching, the metal on the pyramid sidewall (tilted incidence) is etched faster than that at the pyramid apex (normal incidence), leaving behind a metal

island mask just at the tip apex. Finally, the silicon is etched using C_4F_8/SF_6 plasma, and the remaining metal is wet etched.

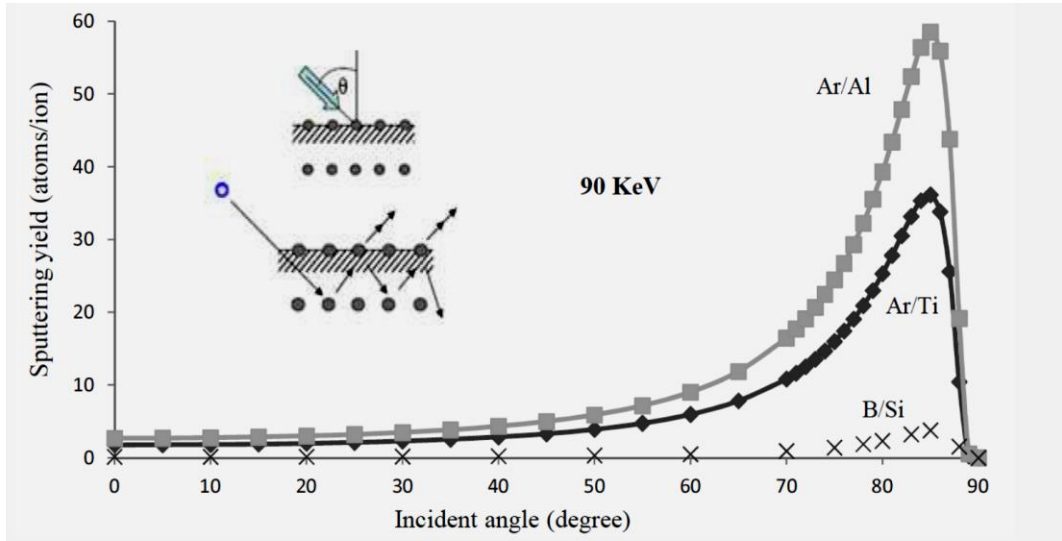

Fig 2.22 Sputtering yield vs ion incident angle for ion milling

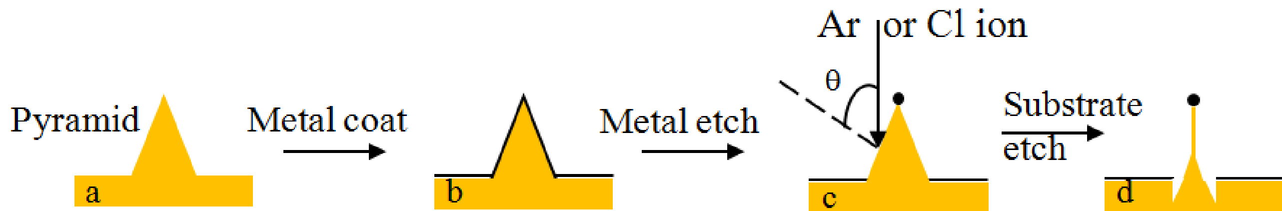

Fig 2.23 Angle dependant dry etching steps

2.2.4. Edge tip fabrication

The commercial tip has a serious issue, due to misalignment during optical lithography. The tip apex is located 5-20 μm away from the end of the cantilever, which makes the determination of the exact tip apex location impossible by the optical microscope integrated into the AFM instrument, since the optical microscope sees only the backside of the cantilever. Therefore, the tip has to engage in scanning a very large area in order to find the area of interest or engage the tip multiple times in order to locate the right

area. In some cases, such as tip enhanced Raman spectroscopy (TERS), the exact location of the tip apex is needed to shine the laser beam into it. Multiple trials may damage the TERS gold-coated tip. It will also lead to tip wear as well as sample damage to soft materials. The natural solution is an edge tip, for which the tip apex is located at the very end of the cantilever and thus its position can be determined accurately.

Several companies have developed the fabrication techniques for edge tip. Fig 2.24 (a) [194], shows one of NanoWorld Company's exact location tip products. Sharp tips apex is a product line from Nano and More company, which is demonstrated in Fig 2.24 (b) where the tip is located precisely at the free end of the cantilever. Bruker's New VTESPA-300 tip, shown in Fig 2.24 (c), has a visible tip apex for the exact location. The Oxford instrument produces AC160TS-R3 tip, illustrated in Fig 2.24 (d).

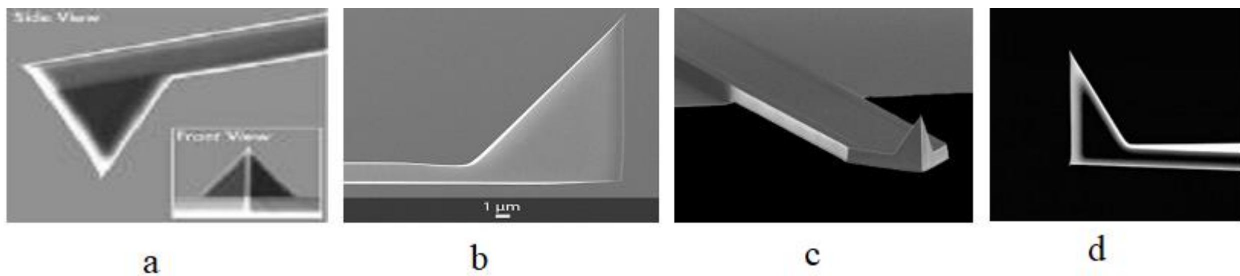

Fig 2.24 Different edge tips

Chapter 3

Batch fabrication of edge and high aspect ratio AFM tips using thin film deposition and etching techniques

3.1. Introduction

This chapter summarises the experimental work performed on regular AFM tips. It describes the fabrication of the different types of AFM probes for selective application. The process starts with one of the three regular commercial tips. The tips are Appnano tips [195], all in one (AIO) tips [196], and Rocket tips [197] shown in Fig 3.1. The process redefines its geometrical structure into the target shape in a simple low-cost batch manner.

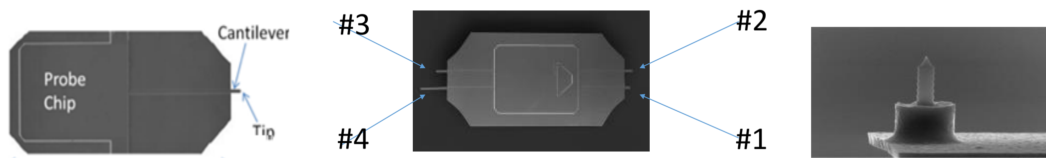

Fig 3.1 Appnano, AIO, and rocket probes respectively (left to right)

Special tips usually target a specific application, usually fabricated using FIB milling. Fabrication of special tips using focused ion beam (FIB) shaping is not cost-effective as well as a time-consuming process employing expensive machines. The fabrication is made one tip at a time and the quality depends on the fabricator's skills. Batch production is the solution to reduce the cost and produce a uniform quality product. In this chapter and chapter six, I have explored the fabrication process of the following tip/pillar in details:

1 – Edge tip (this chapter)

2 – Batch processing of high aspect ratio (HAR) tip (this chapter)

3 – HAR tip using FIB (chapter six)

4 – HAR pillar using ion implanted mask (chapter six)

In the next sections, we will explore the theory and the experimental processes involved in the fabrication of edge and HAR tips in greater detail. The major techniques used in these two projects (edge and HAR tips) are physical vapour deposition (PVD) of thin films via e-beam evaporation using Intlvac Nanochrome, wet etch, and plasma based dry etching of silicon employed Oxford ICP380, which is set for Si etch only. Plasma based dry etching of metal is done using another Oxford ICP380, set for metal etching only.

3.2. Fabrication of edge tip

3.2.1. Introduction

One of the problems of the regular commercial atomic force microscope (AFM) probes is the uncertainty of the tip location at the cantilever. The tip is typically 5–25 µm away from the cantilever end. It is difficult to detect the exact location of the tip as the AFM camera captures the backside of the cantilever and cannot see the tip directly. Difficulty to track down the exact location of the AFM tip leads to a larger scan area and/or multi-scan on the required location, this will risk damaging the scanned object especially soft samples.

The main advantage of the edge tip is the ability to detect the exact scanning location of the tip. The tip in the edge tip is located at the edge of the cantilever where the tip location can clearly be identified. Sideview SEM images of three different edge probes from different manufacturers have been presented in Fig 3.2. In the next section, we will examine the experimental result and the fabrication process of our edge probes in more detail.

Fig 3.2 Examples of few AFM edge tips [198]

3.2.2. Experiment and process discussions

Here we are exploring the method that we have experimented to develop the edge probes. Our process starts with a regular commercial tip and reforms it into the desired shape. The procedure should be simple, low-cost, and batch producible[199].

To transform the regular commercial tip into an edge tip in a batch form, four major steps are required. The first step is the 60° angle directional deposition of masking materials followed by silicon RIE, then wet etch (mask removal), and finally high-temperature oxidation sharpening. A schematic of the experimental procedures executed for reshaping the regular tip into the edge tip is shown in Fig 3.3.

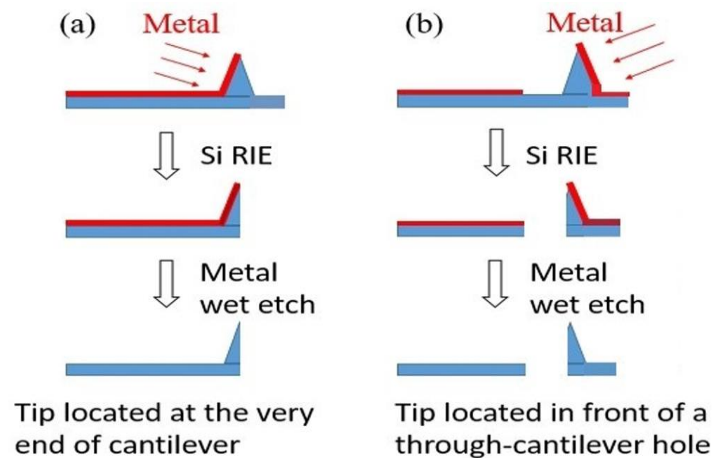

Fig 3.3 60° Angle deposition using e-beam followed by Si RIE then wet etch for both (a) cantilever end and (b) cantilever back

3.2.2.1. Deposition of the mask material

To deposit the mask materials, a decision has to be made regarding which materials to be used. Many parameters are examined in this decision. The material must be cost effective, able to be wet etched, and has low stress; otherwise, the thin film will not adhere to the substrate and will separate. Many materials will meet the first two conditions, but stress requires further investigation. There are two types of stress affecting the deposition. The first one is extrinsic stress, which represents the source as a thermal induced process during the evaporation. The second is intrinsic stress, which represents the property of the materials

like atoms' spacing, orientation, and size. Three material candidates are investigated including aluminum Al, chrome Cr, and chrome oxide Cr_2O_3. The e-beam deposition recipes of these materials are well defined in the e-beam manufacture manual. Fig 3.4 shows the deposition of 250 nm of each of these three materials to the AFM tip using e-beam evaporation technique. Fig 3.4 shows that the Cr has high stress to the point that it cracks, so the acceptable candidates are either Al or Cr_2O_3; however, Al has a rougher surface. Therefore, the more natural choice is Cr_2O_3 for the deposition because it has a smoother surface, which gives a better etching profile.

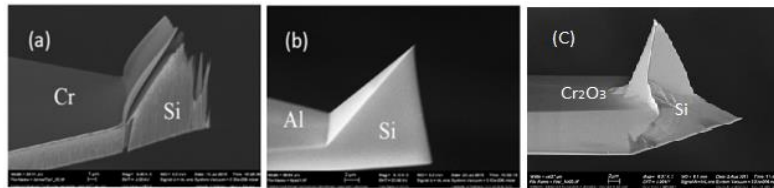

Fig 3.4 The results of the mask layer consisting of (a) Cr (b) Al (c) Cr_2O_3

For this project, we require directional deposition of the masking materials. We use e-beam evaporation as it is a highly directional deposition method. Angle evaporation is employed for the deposition of Cr_2O_3, as shown in Fig 3.5. Many angles have been tested, as we need the mask to be only on one side of the tip and fully covering the apex side while not covering the other side. A 60° angle is used after carefully reviewing many other angles to achieve the best result.

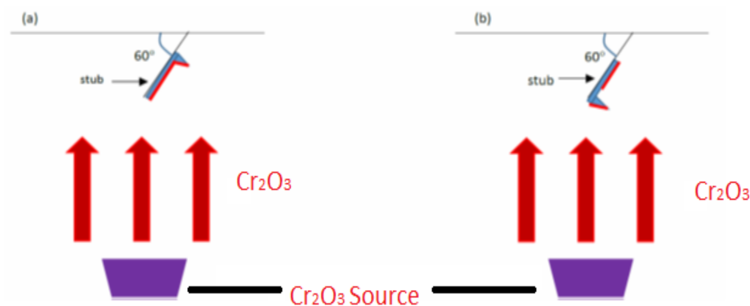

Fig 3.5 60° Angle deposition setup on a tip from two different sides

The deposition from the opposite side, as demonstrated in Fig 3.5 (b), creates an exposed area on the inner side of the tip, due to the shadow of the mask evaporation effect. Tip shadow can create a hole after RIE which detects the exact location of the tip (right in front of the hole seen by the AFM camera). A stub with a 60° angle is mounted to get the desired deposition film on the desired facet of the tip. Fig 3.6 shows the tips after the deposition of the thin film on the probe in both sides.

Fig 3.6 Tip after 60° angle deposition from both (a) front, and (b) opposite side of the tip

To complete the deposition step, two other parameters are set. First, the deposition rate, which needs to be high in theory, but practically lower deposition rate provides a smoother surface. After a careful review of different deposition rates, a 1.5 Å/sec deposition rate is selected. The second parameter is the deposition thickness. The thickness of the Cr_2O_3 deposition is chosen to be 250 nm based on the selectivity of the Si and the mask material etching rate as well as the Si thickness relative to the thickness of the materials to be removed.

3.2.2.2. Dry etch to remove the silicon

Since the tip sidewall profile should be vertical at the end of the cantilever, anisotropic etching is used and thus, silicon dry etch is selected. The etching profile depends on a lot of factors in the dry etching recipe. One of the most famous recipes to etch a vertical wall is the Bosch process, however, because it works in an alternating polymerization and etching, the etch will have a wave-like profile. To get a smooth etch profile, a non-switching process is used. Unlike the Bosch recipe, this recipe uses C_4F_8 and SF_6 continuous gas combinations without switching the etch steps. The gas ratio is set to C_4F_8: SF_6 = 38:22, which leads to a good vertical profile without ripple sidewall. This recipe is investigated by our group members in many

cases and proven to be the best fit in this case where the etching rate is 400 ± 10 nm/min for Si. The etching time will be 20 minutes to etch away the full thickness of the Si cantilever and half of the pyramid tip at one side (maximum 8 µm), while the full 250 nm Cr_2O_3 mask layer is not all etched away, knowing that the selectivity is 1:100. Finally, oxygen plasma etching is required to clean any residue. Table 3.1 shows the details of the Si etch recipe[200] (pseudo-Bosch Si etch recipe). Fig 3.7 shows the resulting tips at both front and back deposition.

Table 3.1 Pseudo Bosch Si etch recipe

RF	ICP	Pressure	Temperature	C4F8	SF6	Si Etch Rate
20 W	1200W	10 mTorr	20 °C	38 sccm	22 sccm	400 nm/min

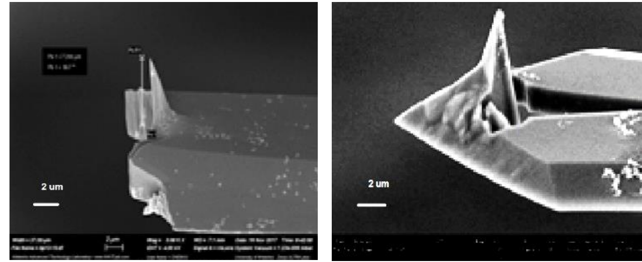

Fig 3.7 Etch results of the tip in both cases (left) front deposition (right) back deposition

3.2.2.3. Wet etch to remove the hard mask

A well-known Cr wet etchant consists of 120 g of Ceric Ammonium Nitrate ($Ce(NH_4)_2(NO_3)_6$) + 100 mL of Acetic Acid (CH_3COOH) + 500 mL of DI water (H_2O). A glass container is used to mix this etchant. Starting with the DI water, add the Acetic Acid, then add the Ceric Ammonium Nitrate, and stir the mixture until it becomes a homogeneous liquid. It needs a temperature of 45 °C and the etching rate of Cr is 240 ± 20 Å/min.

This etchant is for Cr, but it is tested for Cr_2O_3 and is found to be very effective. This etchant is employed to remove the 250 nm of Cr_2O_3 mask in 10 minutes of etching time at 60°C. Fig 3.8 demonstrates the tip after the wet etch.

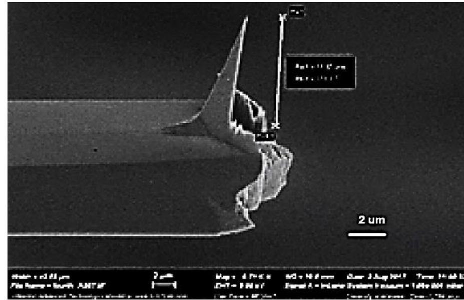

Fig 3.8 Tip after Cr_2O_3 wet etch

3.2.2.4. Sharpening of the tip

The oxidation process followed by the wet etch is employed in this step to sharpen the tip, as shown in Fig 3.9, which is performed in all our results in this chapter to enhance the apex diameter of the tip. Dry oxidation is performed in the air, where the air environment consists of H_2O vapor and O_2. Samples were oxidized at 950 °C for one hour. HF wet etch (diluted at 1:10 with DI water) was performed for 15 minutes. Fig 3.10 shows the final tip after the oxidation and HF etching.

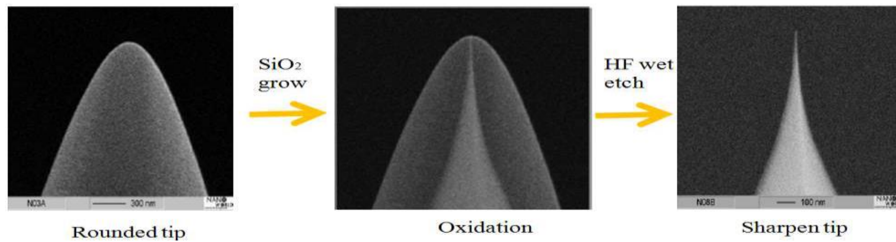

Fig 3.9 Sharpening the tip by oxidation and HF etching [201]

Fig 3.10 SEM image of the edge sharpened tip

3.2.3. Results and testing the edge tip

Optical microscope images in AFM displaying the backside of the cantilever of the regular probe, and our edge tips (front and back side deposition) are shown in Fig 3.11. The red arrow sign represents the exact location of the AFM tip while the regular tip location should be estimated.

Fig 3.11 Screenshot of AFM screen for front edge tip, back edge tip, and regular tip respectively from left to right

The quality and performance of the fabricated edge tips are done through the preparation of the testing sample of a pillar array shown in Fig 3.12 (top right), the pillars have 400 nm height and 200 nm diameter with the center-to-center distance of 400 nm. AFM tips will scan 200 nm wide and 400 nm deep gap where it is a challenge for regular commercial tips. For comparison, two scans on the same area are executed, one for a regular commercial tip, and the other one is performed using the fabricated tips.

The tip was tested using conventional AFM (Dimension 3100). Fig 3.12 (top left) demonstrates the regular tip scans in a pillar array structures where it is not able to reach the bottom. Fig 3.12 (bottom) shows the fabricated tip scans of the same sample where it reaches the bottom.

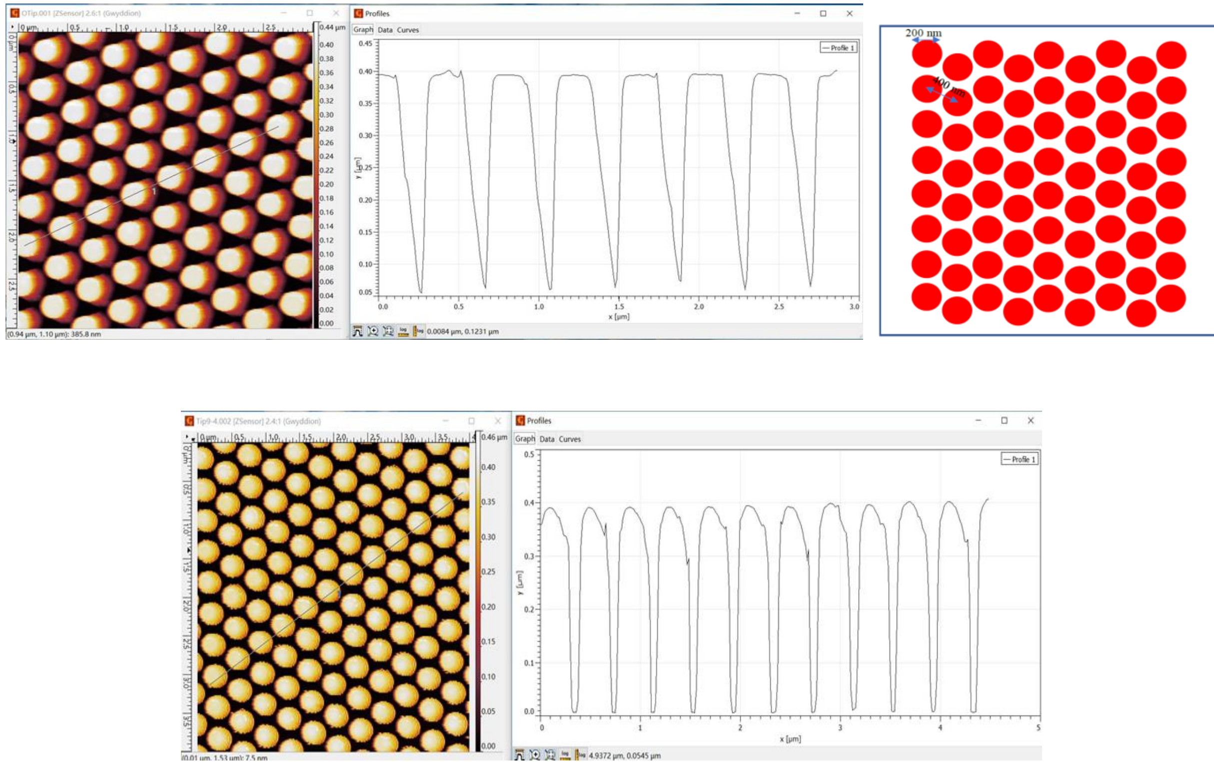

Fig 3.12 (top left) AFM scanning result of regular tip (top right) testing sample (bottom) AFM scanning result of edge tip

3.3. Fabrication of HAR tip

3.3.1. Introduction

An example of the commercial HAR tips is shown in Fig 3.13. The background for these tips is discussed in the previous chapter.

Fig 3.13 Some examples of HAR commercial tips

3.3.2. Experiment and process discussion

To convert the regular tips into HAR tips in batches, the process employs a double deposition of two different masking material at a 60° angle in a different direction and etch it vertically to produce a point mask at the apex of the tip, so we can use it to etch Si apex and create HAR structure on the apex of the regular tip. The process needs four major steps. The first step is the deposition of two materials in two different directions at 60° angle (Cr_2O_3, then Al), followed by RIE for Cr_2O_3, followed by wet etch to clean the Al, then Si RIE for shaping the HAR, and finally remove the overlap Cr_2O_3 mask material. Oxidation can be introduced as an additional step if tip sharpening is needed. The schematic of the process steps is shown in Fig 3.14. Fig 3.14 (a) represents the tip before processing, Fig 3.14 (b) the deposition of Cr_2O_3 at a 60° angle, Fig 3.14 (c) the deposition of Al at a 60° angles on the other side, Fig 3.14 (d) RIE targeting the Cr_2O_3 film, Fig 3.14 (e) a wet etch to remove the Al film, Fig 3.14 (f) Si RIE to create the HAR tip, Fig 3.14 (g) Cr_2O_3 mask is removed. The process target preparing a mask on the apex of the tip, then etching the silicon until reaching the required height resulting in a HAR tip.

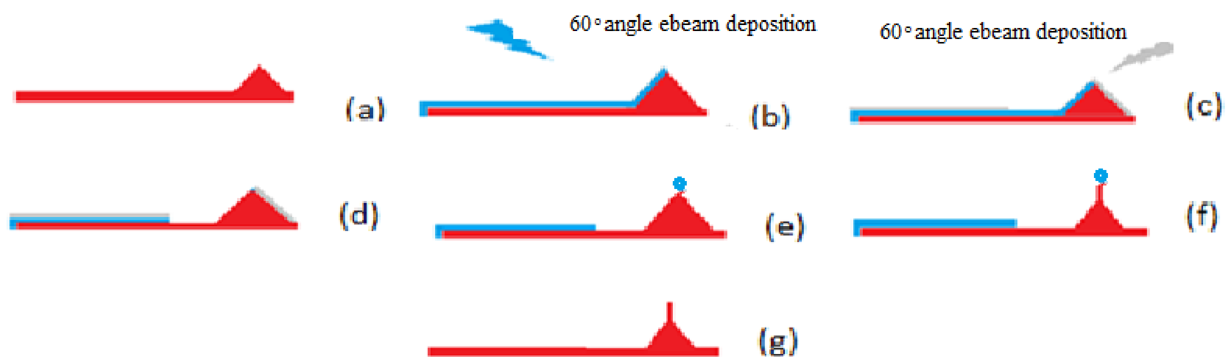

Fig 3.14 Schematic of the process steps to make HAR tip

3.3.2.1. Deposition of two materials

The main idea is to have a mask on the apex of the tip, so when the deep Si RIE etches the silicon, it will create a HAR pillar. To do that, we first deposit Cr_2O_3 with 60° on the tip's back, while the second deposition of Al is at 60°on the other side of the tip pyramid, as shown in Fig 3.15, which leads to a small overlap of the two materials at the tip apex, and no overlap at the three/four sides of the tip pyramid. The Cr_2O_3 is chosen to be 30 nm, while the Al is 60 nm. The reason is the RIE etch for Cr_2O_3 has almost the same etching rate for both materials. So, when etching the Cr_2O_3, the Al will still have about 30 nm left. The evaporation recipe for Cr_2O_3 is exactly like the one performed on the edge tip described above.

Al provides a rougher surface, which means it does not have a good etching profile using RIE and that is why we use wet etch, while Cr_2O_3 has a good etching profile. The deposition in both tip sides (back and front) are shown in Fig 3.15.

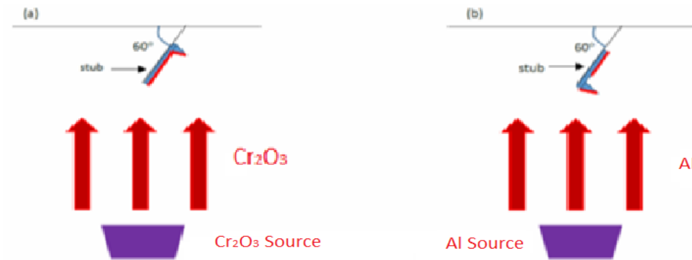

Fig 3.15 60°Cr_2O_3/Al deposition in both front and back of AFM tip

3.3.2.2. Cr_2O_3 dry etch

In this step, once we had successfully masked the tip apex by Al we can remove the excess Cr_2O_3 by ICP plasma RIE, except at the overlap area where the Al is protecting the Cr_2O_3 (at the apex of the tip). To etch 30 nm of Cr_2O_3 knowing that the recipe has an etching rate of 70nm/min, a 30 sec etch time is calculated. However, the Cr_2O_3 is coated at the angle of the tip sidewall and thus a slight over etch is needed to ensure the Cr_2O_3 is completely removed. Many different etching times have been experimented, and it is found

that 70 seconds gives the best result. The recipe of the Cr_2O_3 etch is shown in Table 3.2 which consists of a mixture of two gases Chlorine gas (Cl_2) 50 sccm, and Oxygen gas (O_2) 5 sccm.

Table 3.2 Cr_2O_3 etch recipe

RF	ICP	Pressure	Temperature	Cl_2	O_2	Cr_2O_3 Etch Rate
200 W	600 W	5 mTorr	40 °C	50 sccm	5 sccm	70 nm/min

3.3.2.3. Al wet etch

Al is used as a masking layer to protect the Cr_2O_3 on the apex of the tip and we need to completely remove it after the Cr_2O_3 dry etch. One of the common etchants extensively used to etch Al is PAN etchant (short term for phosphoric, acetic, and nitric acids). It consists of phosphoric acid H_3PO_4 (85% wt), acetic acid CH_3COOH (glacial), nitric acid HNO_3 (70%), and DI water H_2O in a 16:1:1:2 volumetric ratio. Al etching rate using PAN is 100 ± 15 nm/min at a temperature higher than 30 °C. A 60 nm of the Al needs to be etched. To be on the safe side, two minutes of etching is used at 40°C.

3.3.2.4. Si RIE

In this step, the same pseudo-Bosch recipe, previously applied on edge tips, is being employed. As mentioned before, the pseudo-Bosch recipe has an etching rate of 400±10 nm/min for Si. Two minutes of etching time is decided to make the HAR pillar/spike above the tip part. The result of this recipe is shown in Fig 3.16.

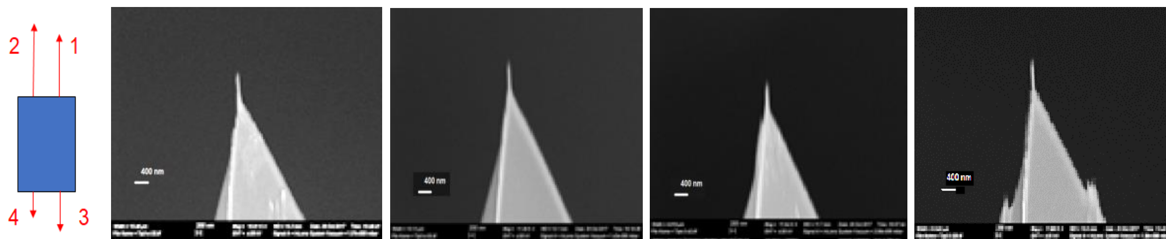

Fig 3.16 The final product of the HAR tip showing the 4 apexes (1, 2, 3, 4 respectively from left to right) of a single AIO probe (tips of AIO probe are numbered at the far left)

3.3.2.5. Sharpening the tip using oxidation

This step is optional depending on the resulting tip. Fig 3.17 shows the HAR tip after oxidation. The oxidation process is the same as the edge tip. Dry oxidation is used with air, which contains H_2O vapor and oxygen O_2, to oxidize the silicon at 950 °C for about one hour. HF etchant (with a concentration of 1:10 of HF: H_2O) is conducted using a plastic beaker for 15 minutes (about 100 nm of SiO_2 and the etching rate is 20 nm/min, over etch is recommended).

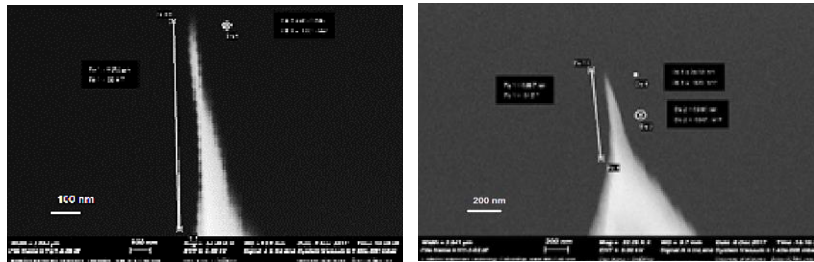

Fig 3.17 HAR tip after the oxidation

3.3.3. Results and testing the tip

We used the same scanned sample as in the edge tip. AFM tips will scan 200 nm wide and 400 nm deep gaps in between the pillars where it is a challenge for regular commercial tips. The fabricated HAR tip is tested by an AFM tool (Dimension 3100) under tapping mode. The height, width, and length of cantilevers of the fabricated tip (AFM scan shown in Fig 3.18 (bottom)) were similar to the regular commercial tip which performs the AFM scan shown in Fig 3.18 (top). As demonstrated in Fig 3.18, the regular tip scans of the pillar array structures show that it is not able to reach the bottom while our fabricated tip reaches the bottom. Also, the fabricated HAR tip shows a much better scan profile and higher vertical resolution than the regular commercial tip.

To test the reliability of the fabricated tip, we scanned the same sample ten times employing the same fabricated HAR tip and compared the gap depth obtained from all AFM results. The results didn't show any significant change, which proves that the fabricated tip can maintain the performance for enough scans.

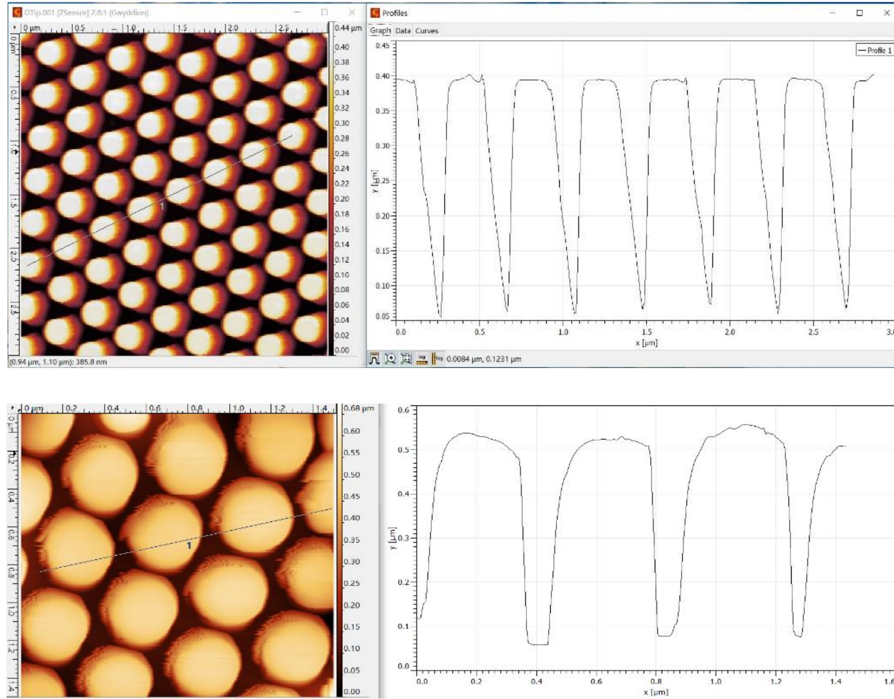

Fig 3.18 AFM scan for (up) regular AFM tip (bottom) our fabricated HAR AFM tip

3.4. Conclusion

We have developed a simple and cost-effective process that can be applied in batches to regular commercial probes to be converted to edge probes. This tip could be thermally oxidized to produce sharper tips. An AFM test is performed and shows a clear location of the probe.

Besides, we successfully introduced a method to fabricate the high aspect ratio AFM probes out of the regular commercial probes, which can be fabricated in batches. The main procedure is to form a small Cr_2O_3 dot mask on the tip apex of each tip, then etch the apex Si around the mask to reveal the HAR tip. This process has successfully accomplished the aspect ratio tips in the range of 15:1. AFM test shows that the fabricated HAR tips have a significantly better image quality compared to regular commercial tips. This method is a batch and lithography free process at a lower cost and higher throughput.

Chapter 4

AFM tip sharpening using oxidation technique

4.1. Thermal oxidation

Thermal oxidation [202] [203] [204] [205] [206] [207] is a process in which there is an initial growth on the surface until complete coverage is achieved, followed by diffusion of the oxygen through the oxidized layer and continued oxidation to the following layer. Oxidation is usually employed either through oxygen found in air or water; these are called dry and wet oxidation respectively.

In this research, dry oxidation is used with air, which contains vapor (H_2O) and oxygen (O_2), to oxidize the silicon at 950 °C for about one hour. Programming the furnace is according to the curve shown in Fig 4.1.

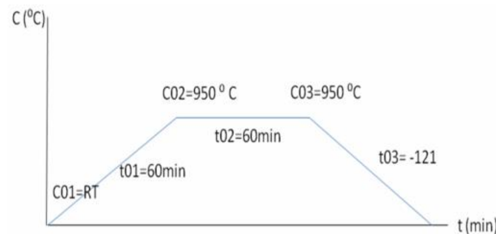

Fig 4.1 Thermal oxidation curve for furness programming[208]

The silicon oxidation chemical equation is $Si\ (s) + O_2\ (g) \rightarrow SiO_2\ (s)$

The result is growth in size, based on the following equation:

$$\frac{\text{Thickness of Si}}{\text{Thickness of SiO}_2} = \frac{\text{Molar volume (Si)}}{\text{Molar volume (SiO}_2\text{)}} = \frac{\frac{\text{Molecular weight (Si)}}{\text{Density (Si)}}}{\frac{\text{Molecular weight (SiO}_2\text{)}}{\text{Density (SiO}_2\text{)}}} = \frac{\frac{28.9\ \text{g/mol}}{2.33\ \text{g/cm}^3}}{\frac{60.08\ \text{g/mol}}{2.21\ \text{g/cm}^3}} = 0.46$$

4.2. AFM tip sharping by oxidation

Si tips can be sharpened [209] [210] [211] [212] by thermal oxidation of Si to SiO_2 at temperature <1050° C, then etching the SiO_2 layer with HF. The stress reduces the oxidation rate at a high curvature resulting in sharping a cone of silicon at the tip apex, as shown in Fig 4.2. Marcus et al. [213] used oxidation to sharpen a tip with aspect ratios of 10:1 to 1 nm curvature at the apex. Oxide sharpening is not quite effective for Si_3N_4; it has been reported to have an apex of 11 nm radius of curvature [214]. However, oxidation sharpening limits control over the height and width of the tip [215].

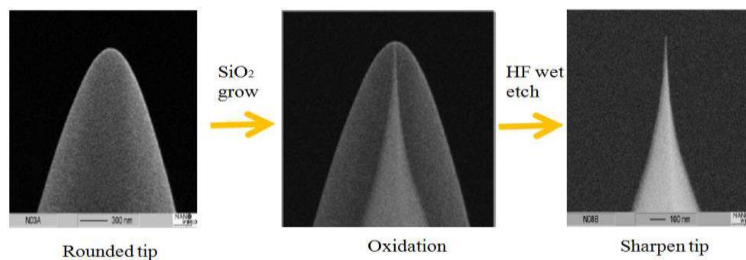

Fig 4.2 Oxidation sharpening steps

4.3. AFM tip sharpening techniques

Sharp silicon tips are critical for many applications including but not limited to electron emission display, nanoelectronics mechanical systems, probes for biological microneedle array, electrical propulsion, and atom probs. Also, sharp tips are essential for high-resolution atomic force microscopy (AFM) imaging. Many techniques are introduced to fabricate sharp tips like neon ion sputtering and dry plasma etch. However, thermal oxidation sharpening is the most widely sharpening method used for commercial AFM tip fabrication.

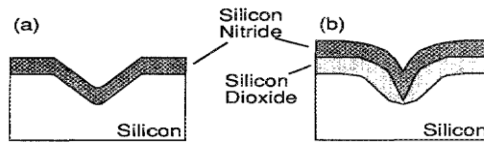

Fig 4.3 Growing silicon oxide in a mold to sharp the tip

Many researchers are working in the oxidation experiments to understand more about this technique. S. Akamine et al. [216] fabricate casting shown in Fig 4.3 and modify it by low temperature thermal oxide for a sharper tip, then deposit the tip material into the mold. This process results in the modification of the curvature from 500 to 110 Å and aspect ratios from 0.5 to 0.95 with an oxide thickness of 3888 Å. As shown in Fig 4.4, N. Sakuma et al. [217] build on the same idea and fabricate sharp tips by creating a thermally oxidized mold and deposit a diamond film using hot filament CVD and then transferred it to a glass substrate.

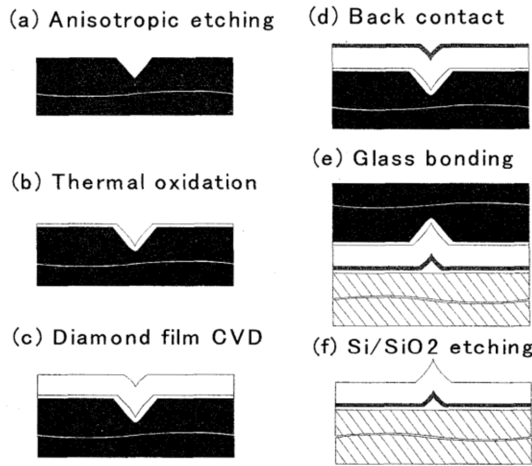

Fig 4.4 Tip fabrication process

As shown in Fig 4.5, H. Im et al. [218] employ the same idea, then a thin film of Au or Ag is deposited on the template followed by an optical adhesive, the peeled off reveals the sharp tip which has a smooth top surface. This tip is good for tip enhanced Raman spectroscopy (TERS).

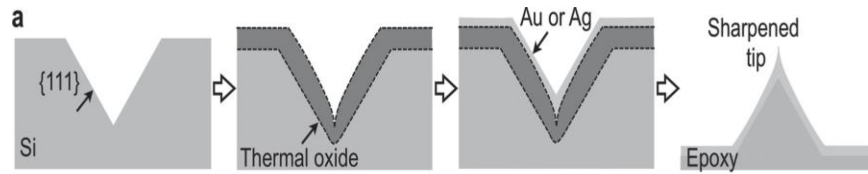

Fig 4.5 Process flow for sharpened pyramid tip fabricating

As shown in Fig 4.6, H. Takemura et al. [219] fabricate a tip with a configuration that has a two steps cone to shape. The upper and lower cone are independently controlled. The upper cone controls the tip sharpness and the apex angle which is determined to be between 10 and 30 degrees, while the lower part controls the tip height by using two steps thermal oxidation. They produced 1944 tips within a full six inches wafer.

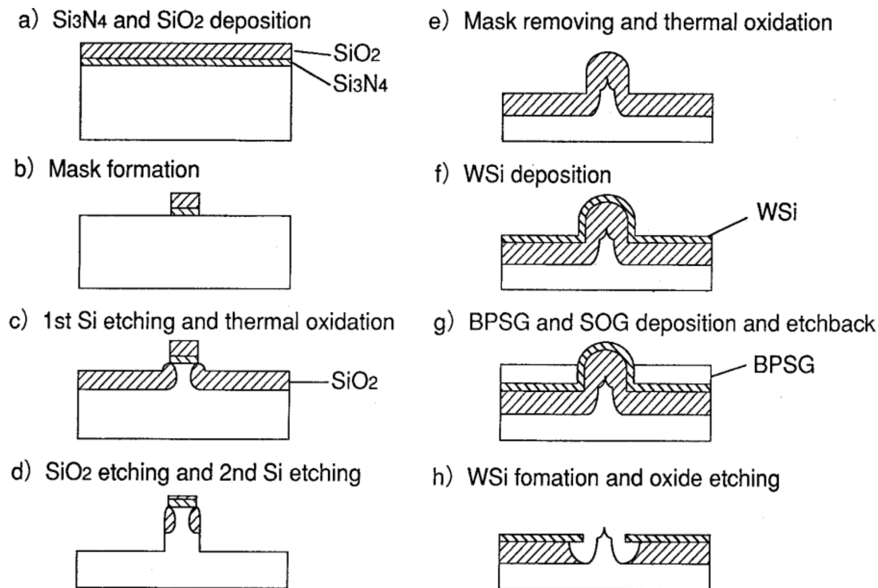

Fig 4.6 Main fabrication process flow

A.B. Janssen et al. [220] uses neon ion sputtering under a high vacuum to sharpen tungsten tips. B. Tang et al. [221] fabricate sharp silicon tips with a high aspect ratio without additional thermal oxidation sharpening. They use wet anisotropic etching to create a narrower tip curvature radius of 20 nm and steep sidewalls front angle of 18°. M. Alves et al.[222] replace the high temperature thermal oxidation technique with a mask of amorphous hydrogenated carbon films for silicon etching followed by SF_6 plasma reactive ion etching to sharpen the tips.

M. R. Rakhshandehrooa et al. [223] employ dry etch to sharpen the tip. The dry etches of Cl_2 plasma generated at 0.7 mTorr for 7 min, reduce the tip radius from 67 to 22 nm. The use of plasma oxidation results in a reduction of the tip from 67 to 8 nm where 257 nm of room temperature plasma oxidation is grown.

Many other researchers [224] [225] [226] [227] [228] [229] report further sharpening of the tips to be below 20 nm by thermal oxidation and the removal of the oxide. V. Agache et al.[230] perform dry oxidation resulting in very sharp silicon tips at 1000 °C and 1100 °C.

H. He et al. [231] study the thermal oxidation with four groups at 900, 950, 1000, and 1050 °C. They conclude a trade-off between the aspect ratio and tip diameter and recommend the optimal oxidation at 1000 °C where a tip diameter of 6.3 nm is fabricated as shown in the process of Fig 4.7.

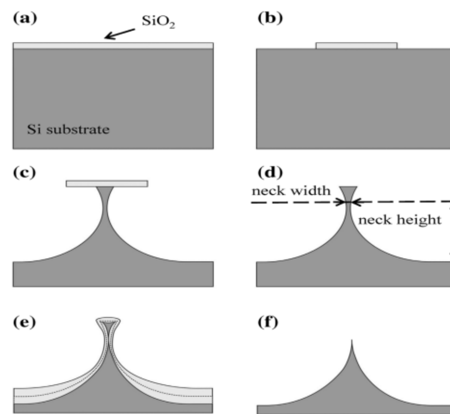

Fig 4.7 Fabrication of sharp silicon tips

4.3.1. Dry and wet oxidation

There are two main types of Si oxidation, dry and wet oxidation. Dry oxidation: have a slow rate and a higher quality than wet oxidation. Wet oxidation: is a mixture of O_2 and H_2O (O_2 bubble through hot water) used as the oxidant. Fig 4.8 shows the silicon oxidation thickness vs oxidation time in different temperatures according to Deal and Grove (D-G) mathematical model calculation in both dry and wet oxidation [232].

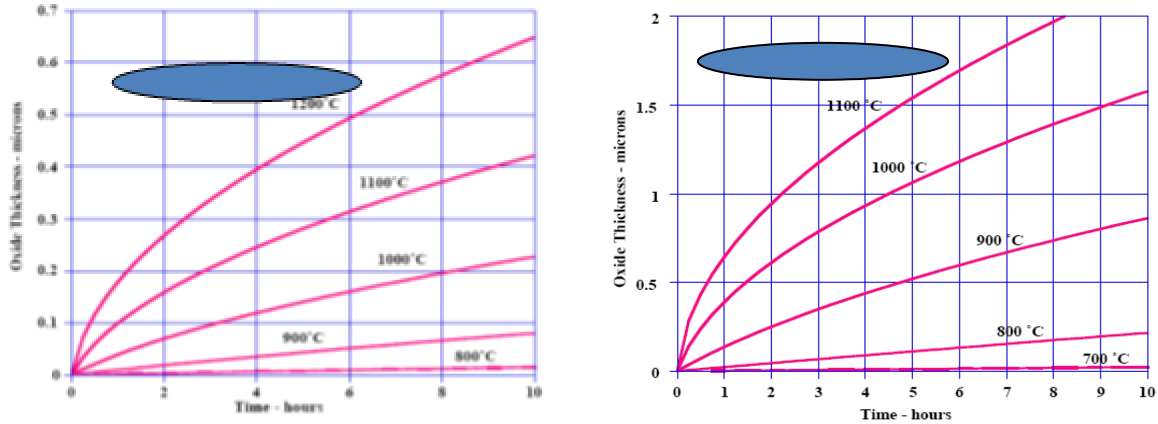

Fig 4.8 Calculation of the oxidation rate from D-G model (left) dry (right) wet

4.3.2. Oxidation growth direction and effect

Surface oxidation rate, oxidant diffusivity, and oxide viscosity are the three parameters that affect the stress according to experimental results obtained by Kao et al. [233] where the mechanical stress effects, clarify the mechanism of the oxidation interface of concave and convex geometries. M.Y. Jung et al. [234] grow 100 nm of oxide at 900 °C and etched by H_2O: HF = 7:1 which results in a 10 nm sharp tip.

The oxidation of silicon happened in two mechanisms [235]. The first mechanism is linear oxidation which is the direct reaction of the oxygen with the silicon surface. The second mechanism happens after reaching critical oxide thickness where the oxidation by the diffusion of oxygen through the grown oxide reacts with the silicon surface beneath the oxide and the reaction follows a parabolic rate law. These two mechanisms are sufficient to predict the oxide thickness, but the oxidation rate is slower on wedges and curved surfaces because of the high stress factor at the wedges and curves due to the volume differences of the growing oxide. The high viscosity of the oxide at temperature < ~ 1050 °C keeps the stress high; however, temperature > ~ 1050 °C reduces the viscosity and relieves the stress which causes some deformation to the shape of these wedges and curved surfaces.

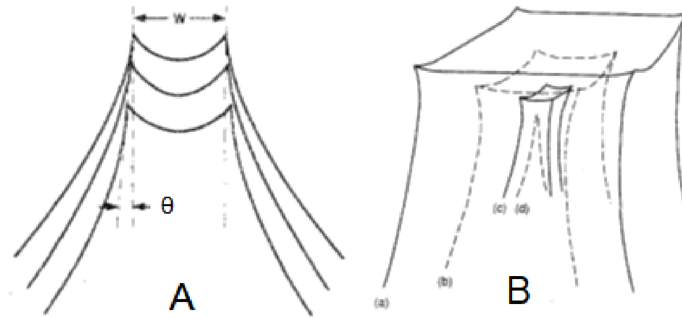

Fig 4.9 Oxidation stages of silicon tip with (A) initially large half angle θ> 20 °, (B) initially small half angle θ = ~ 5°

According to T. S. Ravi et al.,[236] there is another factor that affects the output of the oxidation experiments. The half angle θ (which is measured a distance equal to the tip width w below the tip), as shown in Fig 4.9 (A), is the key for lateral etching direction. For their oxidation sharpening experiment, they used a temperature of 950 "C and oxidation times of 2.5 h. Fig 4.9 (A) shows the sample with half-angle θ > 20 ° after three consecutive oxidations and oxide stripping using HF. It is realized that instead of sharpening a single tip, two sharp tips have formed with the distance between the tips ~ 20% greater than the initial tip width. Fig 4.10 shows the SEM image outcome after breaking the top tip with large θ resulting in multiple tips. Fig 4.9 (B) demonstrates the same experiment with the half angle θ = ~ 5 °. The result is shown after four consecutive sharpening cycles a, b, c, and d.

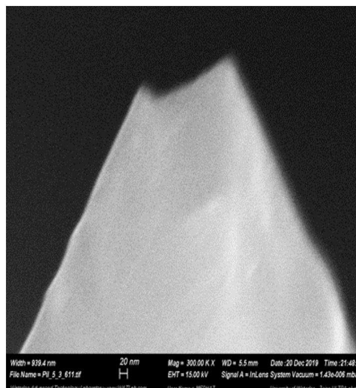

Fig 4.10 SEM image outcome after breaking the top tip and θ is largely resulting in multiple tips

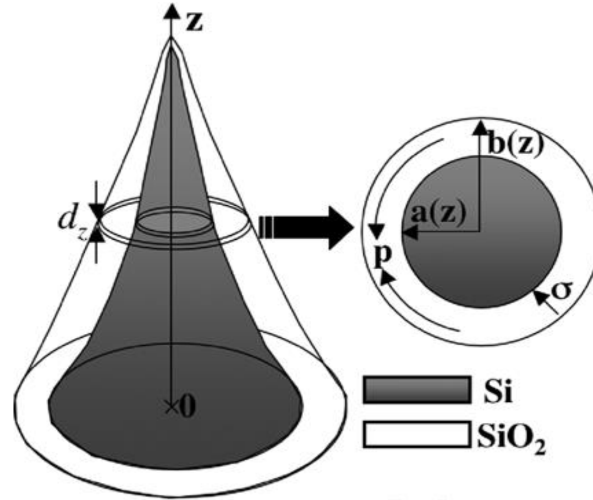

Fig 4.11 Silicon cone oxidation

V. Agache et al. [237] model a silicon cone as a pile of constant thickness circular slices with two coordinates a(z) (the radius of curvature of the silicon surface) and b(z) (radius of the oxide surface), both are a function of vertical position as shown in Fig. 4.11. They study the normal stress to the Si/SiO_2 interface and the pressure over the oxide ring to calculate the lateral growth of silicon oxide in each slice according to Kao et al. They conclude that the larger the curvature radius, the thicker the oxide growth. Since the thickness decreases at the apex and the oxide decline, this mechanism sharpens the AFM tip.

Oxidation sharpening works best when the oxidation rate is limited by chemical reaction for which stress is not important. This is the case for thin (<100nm) oxide growth. When the oxide is thick (well beyond 100nm), diffusion of O_2 or H_2O through the already grown oxide layer becomes the rate limiting factor, and diffusion is affected by stress.

Thermal oxidation is the most widely used process to sharpen the tip due to the different oxidation rates on different tip parts. The smaller the curvature, the more stress, and the lower rate. For pyramid shape AFM tip, the bottom part has a much faster oxide growth rate than that of the apex part resulting in tip sharpening.

4.4. Experimental process of oxidation sharpening of the AFM probes

This oxidation study is focused on sharpening regular commercial AFM tip (AIO tips) with a 40 nm apex shown in Fig 4.12. We need to create a method to produce batches of tips with a sharp apex using thermal oxidation. Thermal oxidation sharpening of silicon tips is the most employed tip sharpening method and it is used for commercial AFM tip fabrication [238].

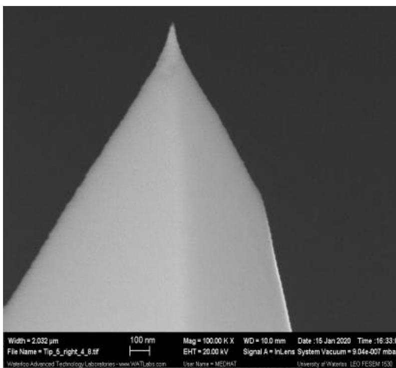

Fig 4.12 Regular commercial AIO AFM tip with 40nm apex

In this research thermal oxidation is performed in a low-cost furnace box as shown in Fig 4.13. [239]. The furnace chamber size is 10cm x 10cm x 12cm and is heated by resistive heating to a maximum temperature of less than 1200 °C and the heating up rate is accurately controlled within a range of 0–15 °C /min with no control of the cooling down rate.

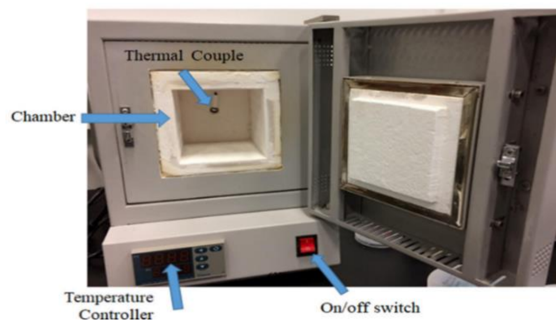

Fig 4.13 low-cost furnace box with maximum temperature less than 1200 °C

4.4.1. Temperature selection

To select the optimum oxidation temperature, we start with 7 regular commercial AIO tips, clean them with solvent (acetone + IPA), then dry oxidize them with different temperatures (850/ 900/ 950/ 1000/ 1050/ 1100/ and 1150 °C) for 30 min (the growth rate is expected to be less than 200nm according to Fig 4.8) then etch away the oxide by HF 1:10 diluted with water for 12 min (over etching is accepted as the etching rate is 20 nm/min and HF has no noticeable effect on silicon). We image the resulting tips under high resolution helium microscope (Zeiss ORION Plus HIM). The resulting images after oxidation and cleaning with different temperatures are shown in Fig 4.14. Fig 4.14 (A) represents 850 °C, (B) 900 °C, (C) 950 °C, (D) 1000 °C, (E) 1050 °C, (F) 1100 °C, (G) 1150 °C.

Oxidation at 1050 °C and above this temperature has a reduced viscosity, where the oxide tends to flow relieving stress at the tip, and the oxidation at the small tip will be faster, resulting in radius increase of the tip with corresponding half angle increase. By analyse the different tip radiuses presented in Fig 4.14 where the smallest and more uniform tip is the probe presented in Fig 4.14 (C) with an oxidation temperature of 950 °C which represents the optimal oxidation temperature.

Although this is out of the scope of this research, it is important to mention that AFM cantilevers with a controllable blunted tip (like Fig 4.14 (E), (F) and (G)) pyramid or spherical shape[240], are utilized for the nano mechanical study of biomaterials where a sharp tip may puncture into the cell membrane and cause damage. An example of these tips is shown in Fig 4.15.

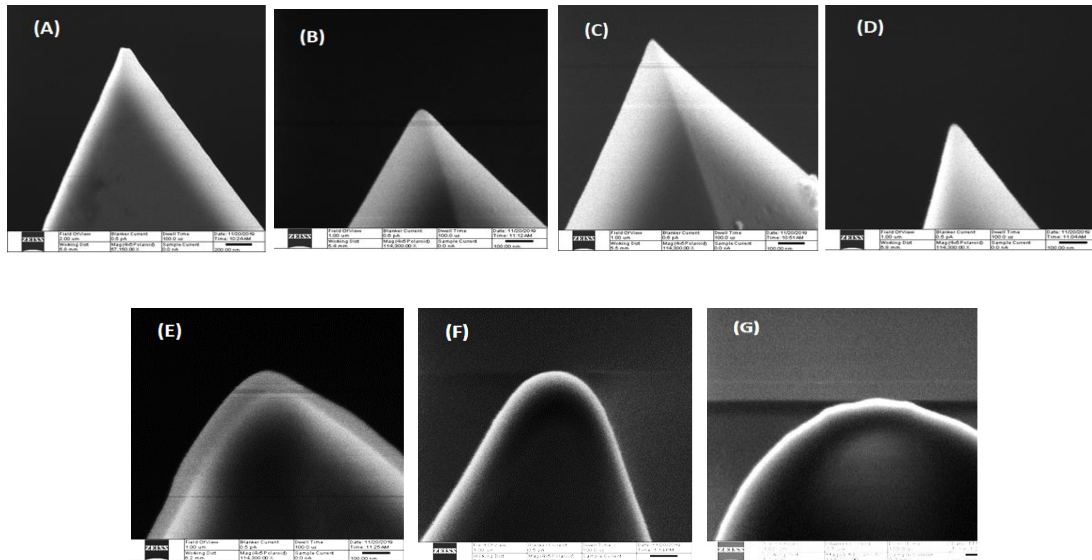

Fig 4.14 Resulting images of different temperatures of oxidation and cleaning at (A) 850 °C, (B) 900 °C, (C) 950 °C, (D) 1000 °C, (E) 1050 °C, (F) 1100 °C, (G) 1150 °C

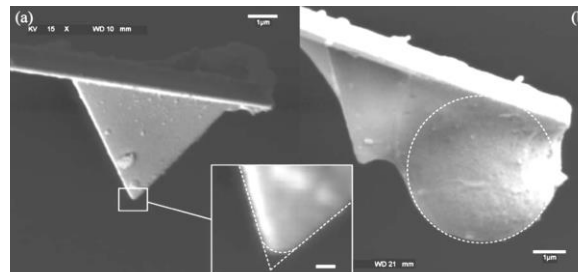

Fig 4.15 AFM blunt tips (a) pyramidal (b) spherical

4.4.2. Furnace calibration

once we know the optimal temperature to oxidize the probes, we need to select the optimal oxidation time. We started with the silicon oxide growth calibration of our furnace. 2x2 cm pieces of silicon wafers are cleaned with a solvent (acetone + IPA), then oxidized them in the furnace at 950 °C for different times. We then coat the photoresist on the half of the chip and bake it for 10 min at 120 °C, and then etch away the oxide by HF 1:10. The photoresist is removed by acetone and IPA, then dried by nitrogen. The etching depth is measured by Bruker Dektak 150 surface profiler, and the resulting oxidation depth vs oxidation

time at 950°C is demonstrated in Fig 4.16. It is noticeable that there are two slopes, the first is up to 4h represent the direct oxidation, while the second slop start at 4h which represent oxidant diffusivity through oxide layer and oxidize the silicon underneath, but the curve never hit the saturation.

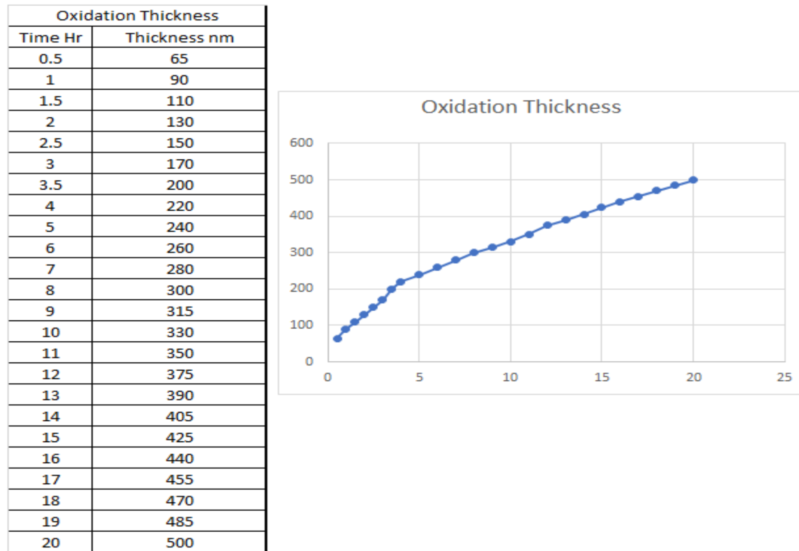

Oxidation Thickness	
Time Hr	Thickness nm
0.5	65
1	90
1.5	110
2	130
2.5	150
3	170
3.5	200
4	220
5	240
6	260
7	280
8	300
9	315
10	330
11	350
12	375
13	390
14	405
15	425
16	440
17	455
18	470
19	485
20	500

Fig 4.16 Furnace calibration at 950 °C for a different time duration vs oxidation depth

4.4.3. Optimal oxidation time for commercial probes

To test for optimal oxidation time, we started with many regular commercial AIO tips, clean them with solvent (acetone + IPA), then oxidize them at 950 °C temperature for different durations between 30 min to 4h (the temperature was increased in 30min increment) and from 5 to 20h (every one-hour increment) followed by etching away the oxide by HF 1:10 (with the etching rate of ~20 nm/min).

Thermal oxidation has the advantage of a self-limiting characteristic. At 950 °C oxidation temperature and lower, the remaining silicon at the apex will be very thin. When the radius of curvature becomes a few nanometers, oxidation will be practically stopped with rates <0.2 nm/h without further oxidation. Longer oxidation will not change the sharpened silicon tip to a blunt. This is because the oxidation rate is slower on a curved (concave or convex) surface due to high stress for a cone or pyramid structure AFM tip. The

silicon apex will be less oxidized than the silicon farther away from the apex which will be sharper after HF removes the oxide.

The resulting SEM images presented in Fig 4.17 were taken with Zeiss Leo 1530 SEM after removing the oxide using HF. The images show tips with oxidation temperature of 950 °C at varying time intervals from 30 min to 4h in half hour increments. Fig 4.18 demonstrate the tips with the same oxidation temperature but the oxidation time from 5h to 20h in one-hour increment. Examination of the images presented in Figure 4.17 shows that the radius of the apex of the AFM tips after removing the oxide layer seems to be reduced from 40 nm to a constant size of around 10 nm (between 0.5 and 11 h of oxidation time) which is logical based on the discussion above. However, from 12 to 20 h oxidation time, the apex size is increased gradually from 10 to 25 nm.

We do not have a clear explanation on why the radius increases at these time intervals, but it could be due to a random factor, broken apex, contamination, or even stress relief due to annealing for a long time (following the over 1050 °C model).

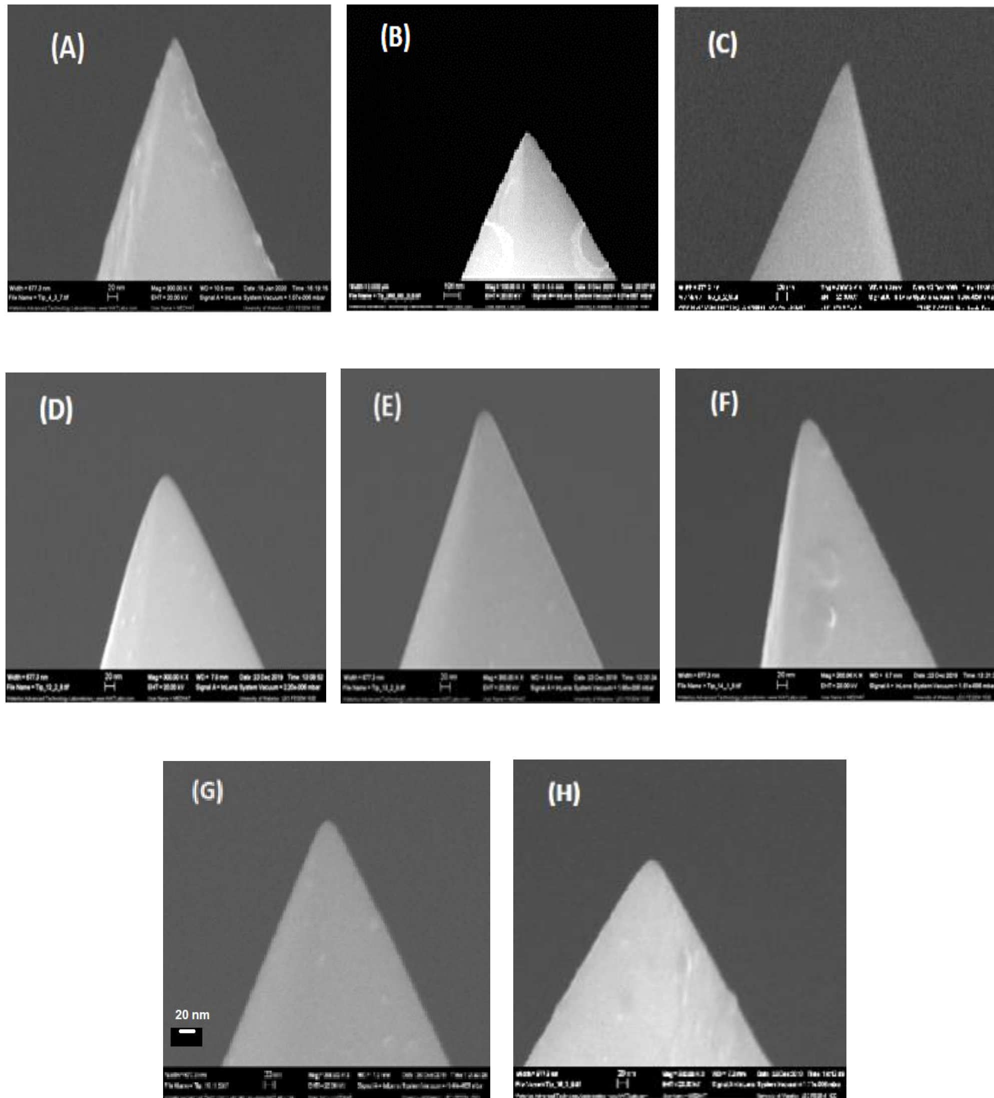

Fig 4.17 Results after removing the oxide for different oxidation duration at 950 °C (A) 0.5h, (B) 1h, (C) 1.5h, (D) 2h, (E) 2.5h, (F) 3h, (G) 3.5h, (H) 4h

In conclusion, the optimal oxidation time is between 0.5 to 1h inclusive, which delivers the smallest radius of curvature at the apex with minimum oxidation time.

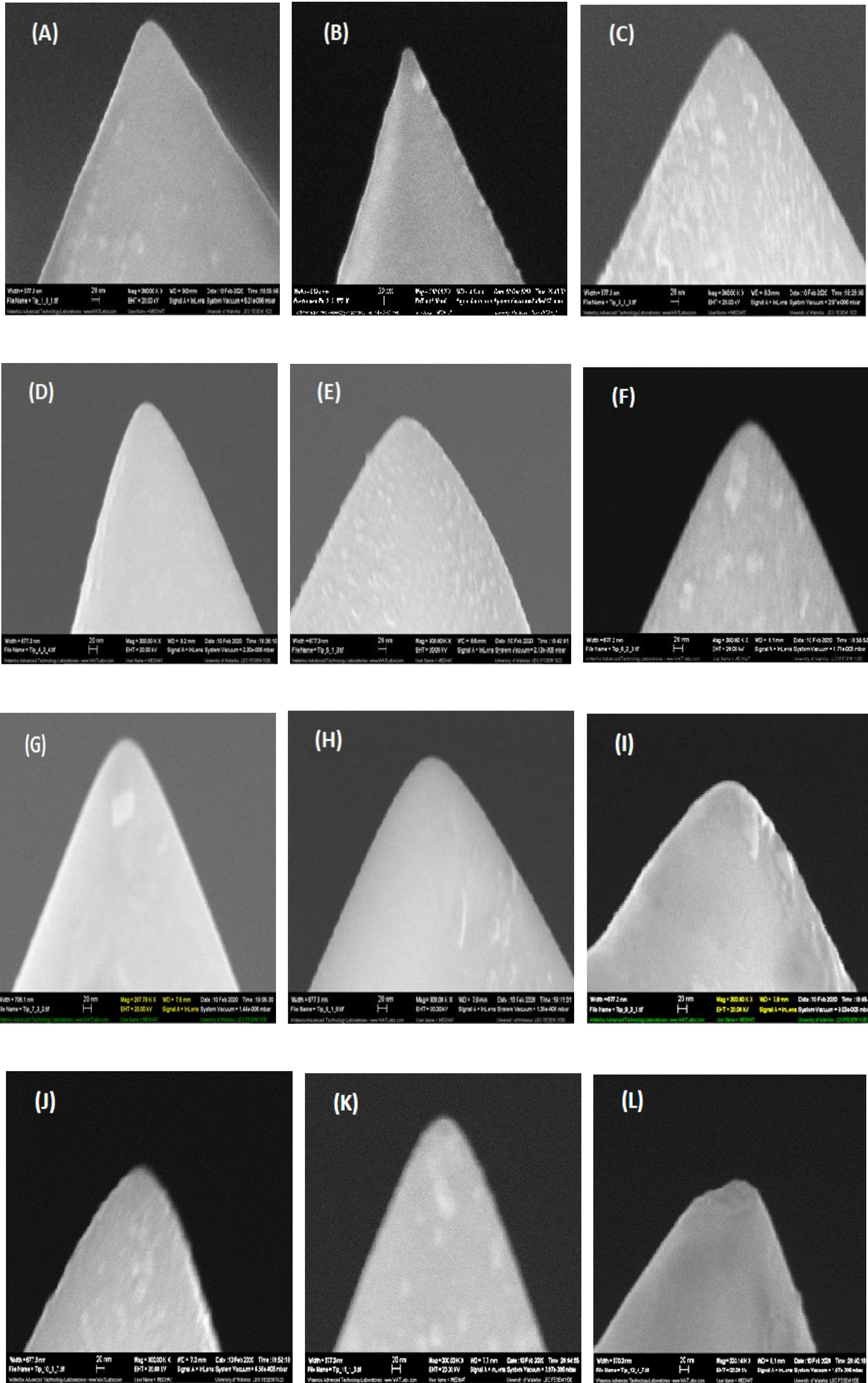
(A)
(B)
(C)
(D)
(E)
(F)
(G)
(H)
(I)
(J)
(K)
(L)

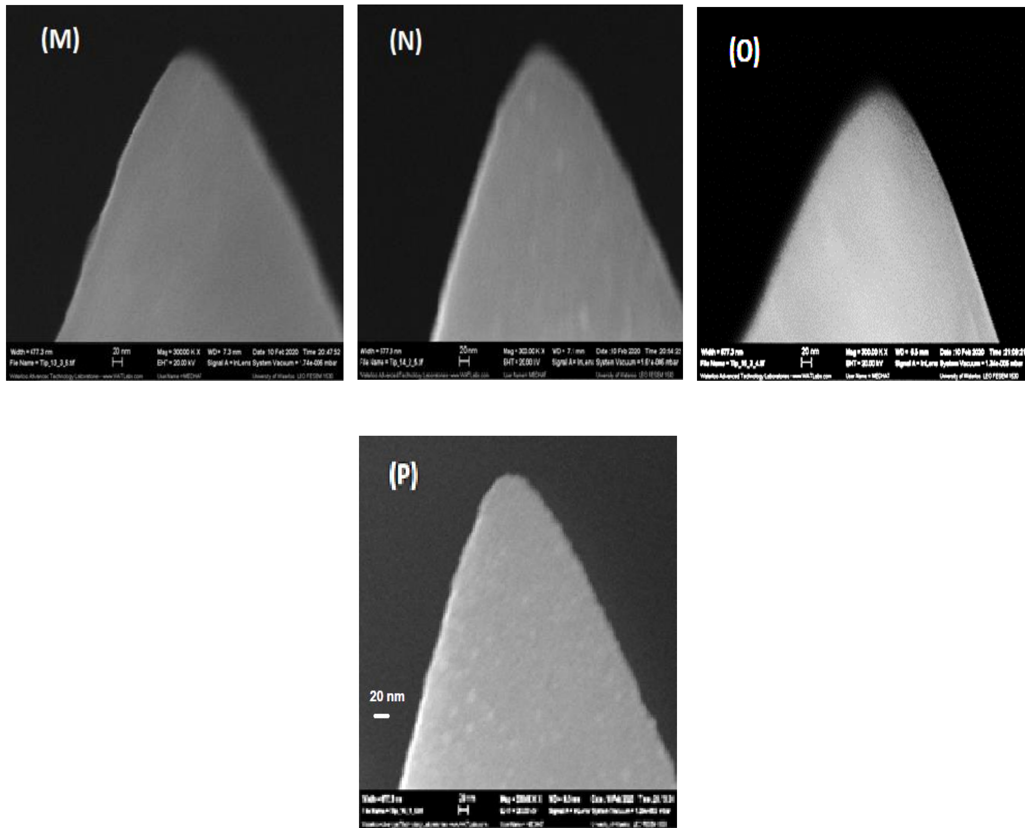

Fig 4.18 Results after removing the oxide for different time duration at 950 °C (A) 5h, (B) 6h, (C) 7h, (D) 8h, (E) 9h, (F) 10h, (G) 11h, (H) 12h, (I) 13h, (J) 14h, (K) 15h, (L) 16h, (M) 17h, (N) 18h, (O) 19h, (P) 20h

4.4.4. Multiple oxidations sharpening to achieve sharper probes

For the best sharpening outcome, the oxide film should be below 80 nm [241 242]. Multiple cycles of oxidation and removal should be performed to avoid the growth of a thick layer. The oxidation thickness of the apex should be less than the oxidation on the surface. Experiment shows that the optimum temperature is 950 °C and the optimum time is 0.5 to 1h.

Based on the above, further sharpening must be done by stripping the oxide in concentrated HF and re-oxidizing at the same temperature and for a similar duration. Multi step oxidation must be tested for the best sharpening oxidation results. Fig 4.19, Fig 4.20, and Fig 4.21 demonstrate the SEM images of probes

that were oxidized on multi step oxidation periods. Fig 4.19 shows the SEM images after removing the 1/2h oxide layer growth for the tip (A) after the first run of the oxidation (B) after the second run (C) after the third run and (D) after the fourth run. Fig 4.20 shows the SEM images of the apex of the probes after removing the oxide layer for the 1h oxidation time for the tip (A) after the first run of the oxidation (B) after the second run (C) after the third run. Fig 4.21 represent the SEM images after cleaning oxidation at 950 °C for (A) 1h then 0.5 h oxidation times (B) 1h, 1h, and 0.5 h oxidations times (C) 1h, 1h, 1h, and 0.5 h oxidations times.

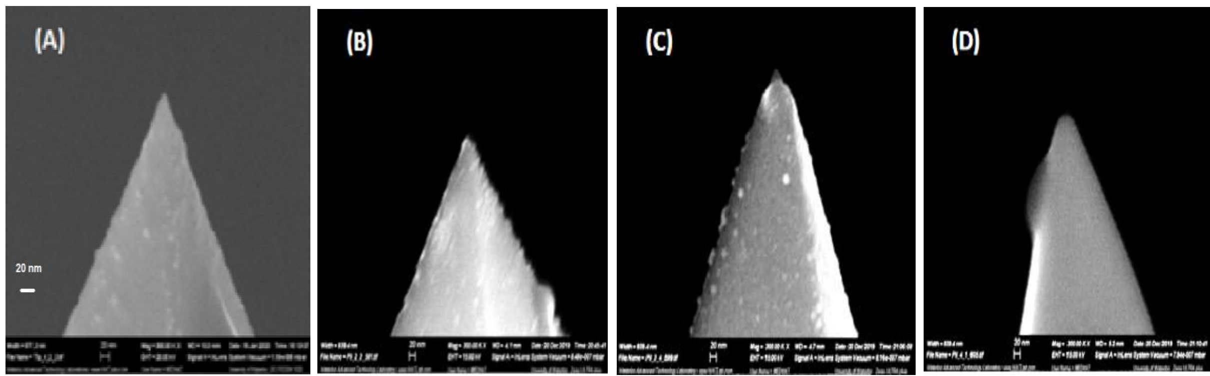

Fig 4.19 SEM images after removing the oxide surface of the probes with oxidization temperature of 950 °C and duration of 1/2h for (A) 1 step (B) 2 steps (C) 3 steps (D) 4 steps

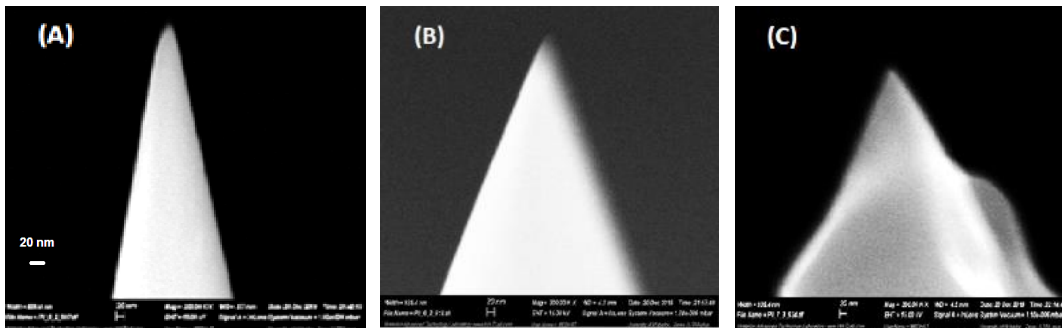

Fig 4.20 SEM images after cleaning oxidation at 950 °C for 1h oxidation time for (A) 1 step (B) 2 steps (C) 3 steps

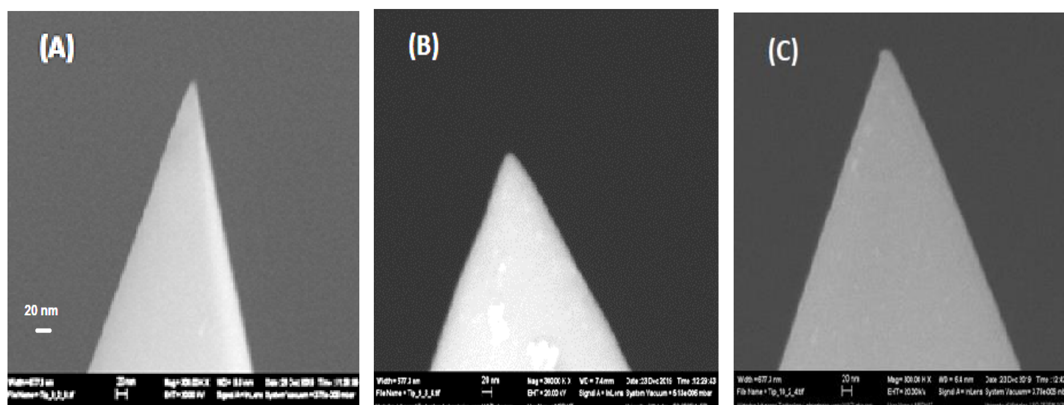

Fig 4.21 SEM images after cleaning oxidation at 950 °C for (A) 1h then 0.5 h oxidation time (b) 2 steps of 1h then 0.5 h oxidations time (C) 3 steps of 1h then 0.5 h oxidations time

4.5. Conclusion

To conclude the result from multiple oxidations runs, we achieve the best results when we repeat the oxidation and the oxide removal process for 2 times consecutively at 950°C for ½ to 1h. We accomplish an apex diameter between 2 to 5 nm. Any further steps are either redundant or the apex may get wider. The SEM cannot be accurate in the range of 2 – 5 nm measurement despite the fact that we went for 300k magnification. Besides, the high charging effect at the apex of the tip at 20K volt cause instability in the imaging and thus taking an image promptly was difficult. High charging effect and longer exposure time would result in SEM images to look like Fig 4.22. For more accurate images we should try TEM shadow imaging.

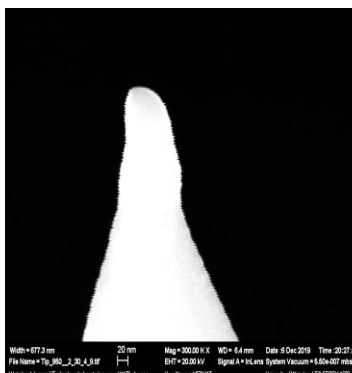

Fig 4.22 SEM image of the swollen tip in real time due to longer exposure time from the electron beam

Chapter 5

Fabrication of ultra-high aspect ratio (UHAR) silicon nanopillars array

5.1. Introduction

High aspect ratio Si nanopillars are employed in the production of the electronic and photoelectronic [243] devices and their applications, include but not limited to, integrated circuits, quantum and strain engineered devices/sensors, nanoscale high mobility field effect transistors, photovoltaics, lasers, and infrared detectors. Besides, HAR structures improve the applications in the biomedical field such as microneedle as well as AFM tips application by increasing the aspect ratio and sharpening the tip apex to enhance the image and extend the AFM use. Techniques for HAR fabrication can be categorized into two approaches: wet and dry etch.

Wet etch is subject to the solubility of etch products while dry etch product is volatile. In dry etching, if silicon or metals are etched with SF_6, CF_4, Cl_2, BCl_3, or $SiCl_4$, typical volatile etching products such as SiF_4, $SiCl_4$, NF_3, WF6 or $AlCl_3$ will be generated.

Dry etching is considered a state of the art [244] in fabrication, due to the vertical nature of the output, as vertical anisotropic structures are needed for nanoscale devices. The downside is the rough surface from the generated ions and electrode biasing. The bombardment breaks the surfaces causing roughness and implementing unwanted materials on the surface. Reactor cleanliness, mask materials/influences, loading effect, the formation of grass on the surface are some of the drawback issues.

On the other hand, wet etch is simple and inexpensive, as well as it delivers a smooth surface. For some materials that are hard to dry etch, it is quite easier to use wet etch, with good selectivity. The main downsides to wet etch are the large undercut, the crystal plane dependant, and the increase in complexity of anisotropic etching. That pushes the etching of HAR structures toward dry etching [245].

5.2. Dry etch

5.2.1. Reactive Ion Etch (RIE) parameter

For RIE [246] [247], the main issue is that any change in one of the parameters will affect all other parameters, and the process must be recalibrated on each change. Five parameters need to be optimized simultaneously: gas ratio, pressure, temperature, RF power, and ICP power.

Bosch based gases SF_6/C_4F_8 are the main gases for silicon etch. For the gas balance ratio optimization of SF_6/C_4F_8 gases, the increase of SF6 will result in a higher etching rate but will decrease the smoothness, while increasing C_4F_8 gas will smoothen the sidewall and reduce the etch rate.

Increase in pressure or temperature will escalate the etching rate but may worsen the sidewall while lowered pressure reduces the undercut on the sidewall. In contrast, a very high temperature causes a thermal damage while lower temperature limits the chemical reaction of the gases, suppresses the lateral etching, improves the selectivity, and reduces the undercut. However, very low temperatures will result in gas condensation.

The increase in RF power will increase the etching rate, reduce the selectivity and the smoothness of the sidewall. Meantime, reduce ICP power lowers the etching rate and enhances the smoothness of surfaces.

The main difference between ICP mode and RIE mode is that in an ICP system, the plasma is remotely generated away from the wafer, disconnecting ion generation and applied bias.

The conclusion of the RIE parameters employing the Bosch process is shown in Fig 5.1.

Response \ Increase	SF6 Flow	C3F8 Flow	Power	Pressure	Passivation duration	Etching duration	Bias Power
Etch Rate	Increase	Little or no effect	Increase	Strong increase	Decrease	Strong increase	Increase
Mask Selectivity	Little or no effect	Little or no effect	Decrease	Strong increase	Increase	Strong decrease	Strong decrease
Uniformity	Strong increase	Little or no effect	Little or no effect	Decrease	Little or no effect	Little or no effect	Little or no effect
Profile Angle*	Decrease	Little or no effect	Decrease	Decrease	Increase	Decrease	Decrease
ARDE Variation	Strong decrease	Little or no effect	Little or no effect	Increase	Little or no effect	Little or no effect	Increase
Sidewall smoothness	Decrease	Increase	Decrease	Strong decrease	Strong increase	Strong decrease	Decrease

Strong increase in response; Strong decrease in response; Little or no effect in resonse; Increase in response; Decrease in response

Fig 5.1 The effects of the Bosch process parameters

5.2.2. Examples of different techniques of HAR nanostructures

HAR can be fabricated by using different techniques, I. Cornago et al. [248] produced high aspect ratio nanopillars arrays with height of 2.5 µm, diameter of 200 nm, and aspect ratio up to 9.8 by laser interference lithography and reactive ion etching. T. B. Kirchner et al [249] use photolithography and anisotropic deep reactive ion etching to produce uniform high aspect ratio silicon pillars. The heights of Si pillars are 15−20 µm, the diameters are 1−3 µm, and the pitches are 2−6 µm. A. Frommhold et al. [250] introduce a multilayer process into nanosphere lithography where lateral and vertical dimensions are independently controlled. They employ reactive ion etching with SF_6/C_4F_8 gases to transfer the nanosphere pattern to the silicon and achieve pillars of 1.3 µm height and 75 nm diameter with aspect ratio of 15.

In the process of HAR Si nanostructures, different masks can be used. D. R. Lincoln et al. [251] employed porous silicon oxide (PSO) as a phase modifier for pillar array. They prove that increasing PSO thickness results in improved the efficacy of pillar array systems. S. Kalem et al. [252] fabricated black Si with high density and high aspect ratio nano whiskers on thermal oxide grown Si by using ICP/RIE in Cl_2 plasma. The properties of whiskers are controlled by several variables such as the time of the process and the chemistry on the surface. Y. Li et al. [253] fabricate high aspect ratio and dense sub-50 nm pillars employing polysiloxane and polystyrene (PS) polymer blend composed of phase separation. The characters of the nanopillars are determined by the spin speeds, the weight ratio, and the concentration of the polysiloxane/PS mixture selected. A high aspect ratio of 1000 is achieved with the etching mask. Y. Zargouni et al. [254] create an array of silicon micro-pillars with 2 μm diameter and 2 μm spacing. They fabricate 55–60 μm high pillars with an aspect ratio of 30 by employing 600 nm TiN as a hard mask where the hard mask remains on top of the pillars after DRIE as shown in Fig 5.2.

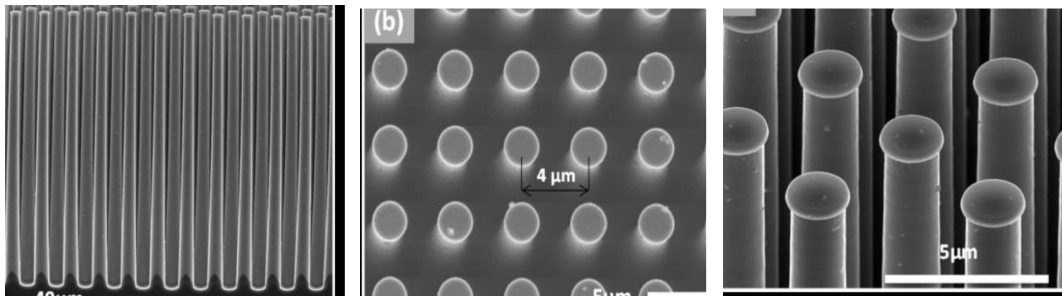

Fig 5.2 Silicon pillar arrays masked with TiN (left) Cross-section, (middle) top and (right) tilted SEM images

L. V. Asquez-Garc et al. [255] use thin film deposition lithography and reactive ion etching to create 100 μm tall and 106 high aspect ratio arrays with an area of 1 cm^2 as shown in Fig 5.3.

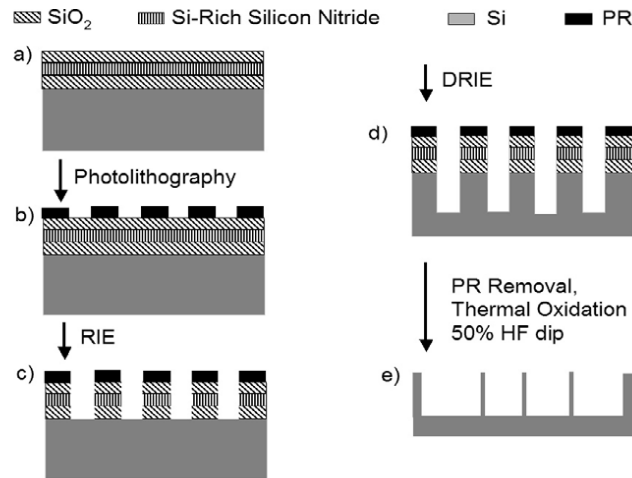

Fig 5.3 Process flow of high aspect ratio silicon

J. Aebersold et al [256] use direct writing exposures instead of traditional photolithography to create a nanopillar array with aspect ratios of 129.9, lengths of 50 µm, and width of 380 nm. The process is demonstrated in Fig 5.4.

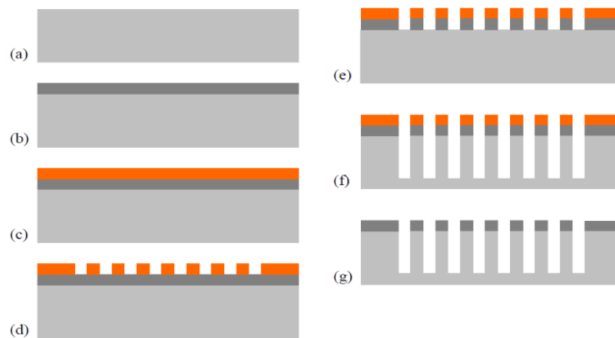

Fig 5.4 Fabrication process of the nanopillar array (a) silicon wafer (b) chrome deposition (c) photoresist layer (d) photoresist patterned by direct exposure (e) chrome etch (f) DRIE silicon etched (g) oxygen plasma etching the residual photoresist.

Soft imprint is another technique used for high aspect ratio structures. M. A. Verschuuren et al. [257] use the soft imprint to create a stamp which is employed in conjunction with a novel tetra methyl ortho siloxane/methyl tri methoxy siloxane sol gel imprint resist material to the features of the rigid silica at room temperature. The imprinted lines are achieved with 10 nm resolution, 5:1 aspect ratio, 6 nm gaps. For

patterning hard mask, RIE pattern transfer processes are used. The fabrication process for high aspect Si structure using nanoimprinted on hydrogen silsesquioxane (HSQ) masks and DRIE is performed by K. Nakamatsu et al. [258]. The DRIE gas sources alternately switching from SF_6 to C_4H_8 results in high aspect ratio Si of 6.5µm height and 43 aspect ratios.

5.2.3. Experiment and discussion

We start with the cleaning process on a silicon wafer with <100> surface orientation to remove the ionic and organic contaminations and the natural oxide layer. Followed by double layer spin coating of positive tone resist which are 250 nm ZEP 520A and 220 nm PMMA resists and pre-baked for 3 min at 180 °C as shown in Fig 5.5. Electron beam lithography using Raith at 20 kV with 500 µC/cm^2 dose is performed to define many circular dot arrays with different diameters (diameter size will be mentioned at each experiment). Both electron beam resists were developed with xylene for 2 minutes. According to the different dissolution rates of ZEP and PMMA in the developer, it can create an overhang resist pattern which is favorable for the lift-off process. After development, 150nm Cr is evaporated by Intlvac e-beam evaporator and the lift-off process is followed by acetone bath with ultrasonic agitation to fabricate the Cr mask. Each sample is etched with different recipes (as each of the following experiments will indicate) by using ICP 380 etcher (Oxford instrument).

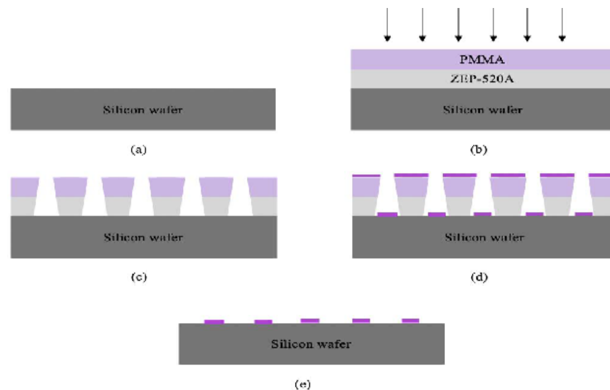

Fig 5.5 Fabrication of the sample array of masks (a) Si wafer (b) photoresist deposition and e-beam lithography (c) photoresist etch (d) Cr evaporation (e) photoresist removal

5.2.3.1. Effect of increasing ICP and RF power

We use a pseudo-Bosch recipe, and its parameter is as follow:

ICP 1200W, RF 20W, pressure 10 mTorr, temperature 15 °C, SF_6/C_4F_8 = 22/38 sccm)

The Si etching rate for this recipe is 400 nm/min. To increase the etching rate, we raise the RF from 20 W to 50 W. The etching rate is increased accordingly to 500 nm/min. The time needed to etch 2 µm is 4 minutes. The result for 500 nm, 800nm, 1200nm Cr mask diameters is illustrated in Fig 5.6, while the ICP power is fixed as 1200W. The resulting diameters are 527 nm, 747 nm, and 1.6 µm, respectively.

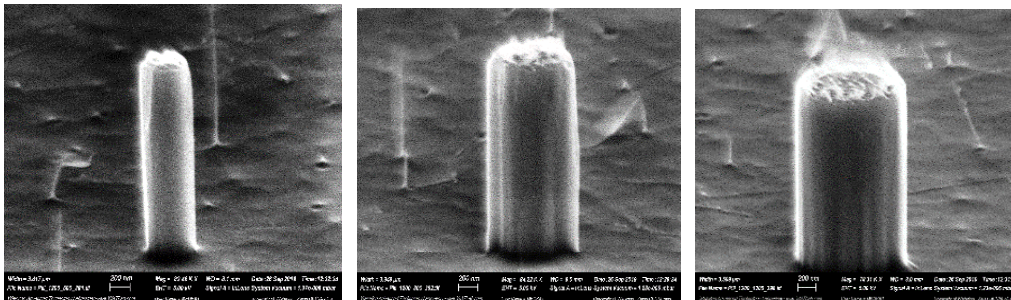

Fig 5.6 SEM image for 4 min etches with ICP 1200 for 500, 800, 1200 nm Cr mask diameters respectively left to right

Next step, we investigate the impact of ICP power on the etching rate. We change ICP power from 1200W to 1600 W and 2000 W while RF is fixed as 50 W. The results show that the etching rates are 580 nm/min for ICP 1600 and 715 nm/min for ICP 2000W.

We test the effect of the modified recipe on the shape of the outcome. To etch 2 µm for ICP 1600W, the time needed is 3.26 min, while for ICP 2000W, the time is 2.48 min. In comparison, the results for 500 nm, 800nm, 1.2 µm Cr mask diameters are shown in Fig 5.6 for ICP 1200W, while Fig 5.7 shows the SEM images for ICP 1600W. The structures are 2 µm high with the Cr mask diameters 500, 800, 1200 nm and the result diameters are 396–699 nm, 747-963 nm, and 1.26-1.400 µm consecutively. The two diameter values on each step represent the upper diameters and the lower diameters which represent the positively tap pillars shown.

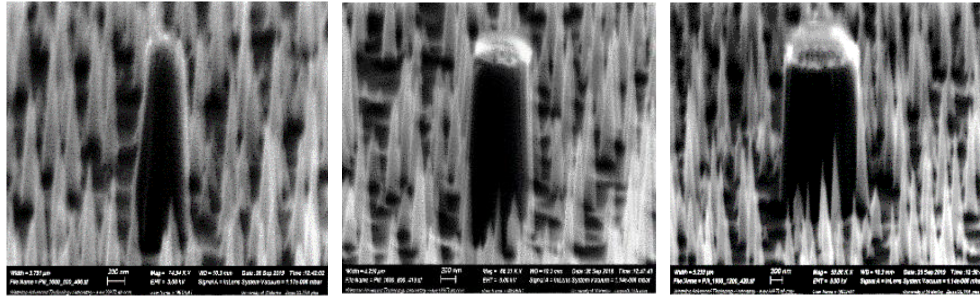

Fig 5.7 SEM image for 3.26 min etches with ICP 1600 for 500, 800, 1200 nm Cr mask diameters respectively left to right

Fig 5.8 shows the SEM images of Si pillars at ICP of 2000 W and Cr mask diameters of 500, 800, 12000 nm. The results have 2 µm height and 448 – 673 nm, 736 - 939 nm, and 1.170 -1.400 µm diameters, respectively. The two diameter values on each step are the upper and lower diameters, respectively.

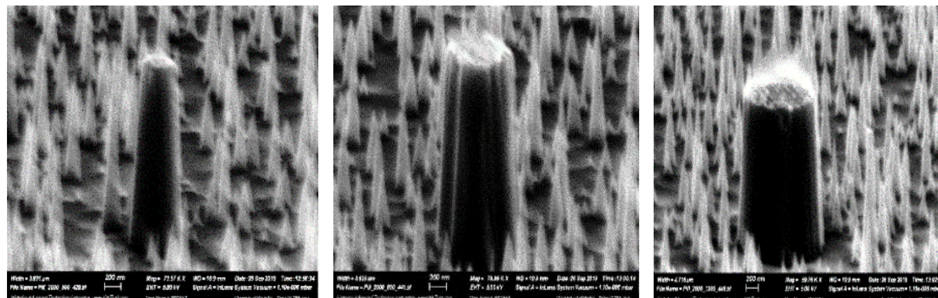

Fig 5.8 SEM image for 2.48 min etches with ICP 2000 for 500, 800, 1200 nm Cr mask diameters respectively left to right

Based on the above figures, the slope is enhanced with the increasing ICP power from 1200W to 2000W. That is because when the ICP power increases at a higher rate than the DC bias, the distribution of the DC bias will allow more reactive ions on the top than the bottom. More ions will result in more etch. This explains the fact that increasing the ICP power will result in a more positive tap pillar.

In conclusion, raising RF from 20 W to 50 W and the ICP from 1200 W to 2000 W increases the etching rate and changes the etching shape. Fig 5.7 and Fig 5.8 show a rough surface that needs extra cleaning

between each etching cycle in which case we can introduce oxygen cleaning into the substrate at the end of the etching cycle.

5.2.3.2. The effect of oxygen plasma cleaning cycle on etching rate and profile

To be able to detect the effect of the oxygen cleaning we have to run the recipe with/without the oxygen cleaning then compare the results. The first cycle is a modified pseudo-Bosch as follows:

Pseudo Bosch (Si Etch cycle): ICP 2000W, RF 50W, pressure 10 mTorr, temperature 15 °C, SF_6/C_4F_8 = 22/38 sccm).

We change the RF to 50 W and ICP to 2000 W as demonstrated in the previous section for the pseudo-Bosch recipe. For the pseudo-Bosch recipe with ICP 2000W RF 50W, the etching rate is 715 nm/min. Fig 5.9 shows SEM images of samples etched for 10 minutes. The diameters of Cr masks are 1200 nm, 800 nm, and 500 nm.

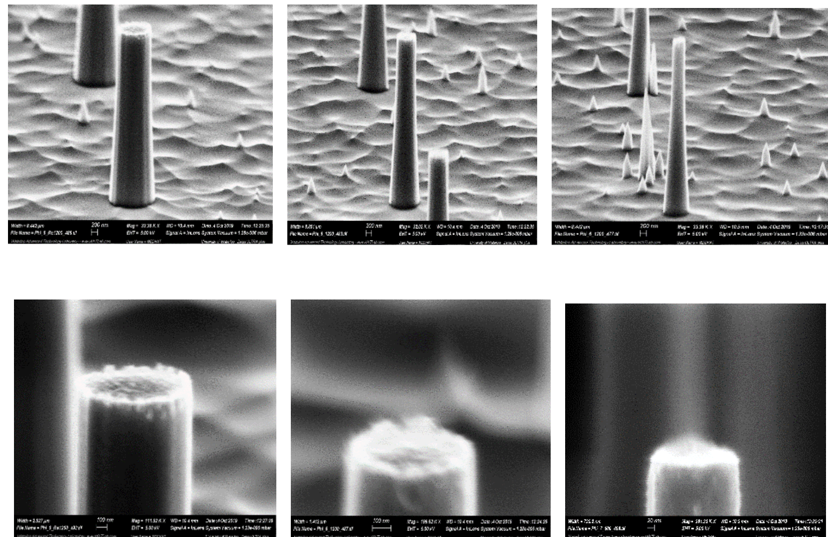

Fig 5.9 SEM image for 10 min etches with for 1200, 800, 500 nm Cr mask diameters with gas ratio SF_6/C_4F_8 = 22/38 respectively left to right, the lower images are the magnification of the top images

For 1200 nm diameter Cr mask, pillars are about 5µm high and the diameters are 1.14-1.5µm; for the 800 nm diameter Cr mask, pillars are 5µm high and 0.67-1.14µm in diameters; while for the 500 nm diameter Cr mask, the structures are 4.66 µm high and 814-348nm diameters as shown in Fig 5.9. The upper images represent the pillars, and the lower images represent the top part to check the Cr mask residue.

When the gas ratio C_4F_8/SF_6 is changed to 45/15, The recipe will be as follows:

Pseudo Bosch (Si etch cycle): ICP 2000W, RF 50W, pressure 10 mTorr, temperature 15 °C, SF_6/C_4F_8 = 15/45 sccm).

To achieve the etching height of around 5 µm, the etching time is increased to 20 minutes. Fig 5.10 shows the result for gas ratio of C_4F_8/ SF_6 = 45/15 with 1200 nm diameter Cr mask, the height is 5.46µm, and the diameters are 1.1-1.5µm. For the 800 nm diameter Cr mask, the height is 5.58µm and the diameters are 627-983nm. For the 500 nm diameter Cr mask, the height is 5.7µm and the diameters are 300-400 nm.

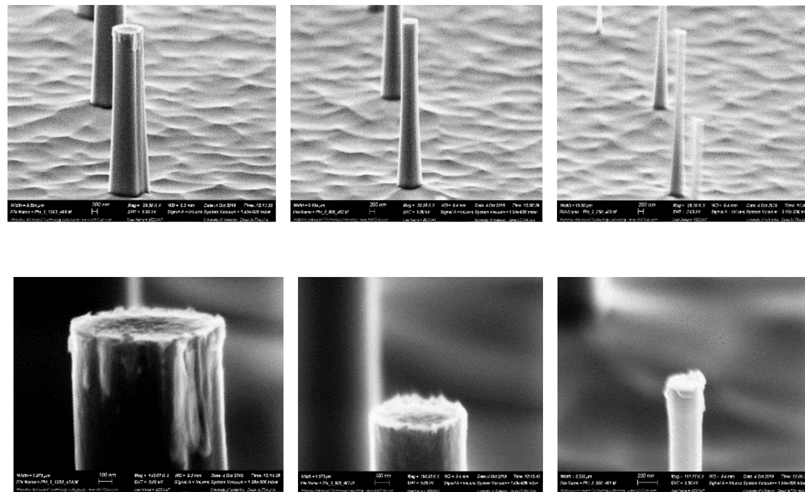

Fig 5.10 SEM image for 20 min etches for 500, 800, 1200 nm Cr mask diameters with gas ratio SF_6/C_4F_8 = 15/45, respectively left to right, the lower images are the magnification of the top images

To add the oxygen cleaning cycle, an alternate between the pseudo-Bosch recipe (a mixed gases of C_4F_8 and SF_6) and the oxygen cleaning take place. It consists of a loop of two cycles that can be run alternatively.

The first cycle is a modified pseudo-Bosch recipe while the second cycle is an oxygen clean cycle. The recipe is as follows:

Pseudo Bosch (Si etch cycle): ICP 2000W, RF 50W, pressure 10 mTorr, temperature 15 °C, SF_6/C_4F_8 = 22/38 sccm), 1 min.

O2 clean cycle: ICP 2000W, RF 50W, pressure 10 mTorr, temperature 15 °C, O_2 20 sccm), 10 s.

The experiment will repeat the pseudo-Bosch and the oxygen cleaning cycle for 40 cycles, (in each cycle, the etching time is 1 minute, and the cleaning step is 10 sec). After 40 cycles of etching, with SF_6/C_4F_8 gas ratios of 22/38 and 15/45, the etch results are 10 µm and 5 µm respectively. While the RF power is still 50 W and ICP power is 2000 W in both cases. The result is shown in Fig 5.11 for SF_6/C_4F_8 gas ratio of 22/38 and in Fig 5.12 for SF_6/C_4F_8 gas ratio of 15/45. For SF_6/C_4F_8 gas ratio of 22/38. All the pillars have a common height of 9.8µm, while the diameters of 1200 nm Cr mask, is 1.07-1.79 µm with an undercut of 88 nm. The 800 nm Cr mask diameter has a 0.6-1.422µm diameters with undercut 101nm and the 500 nm Cr mask diameter has a 0.311-1.1µm diameters with the 92-138nm undercut. The upper images for Fig 5.11 show the pillars while the lower ones show the undercuts.

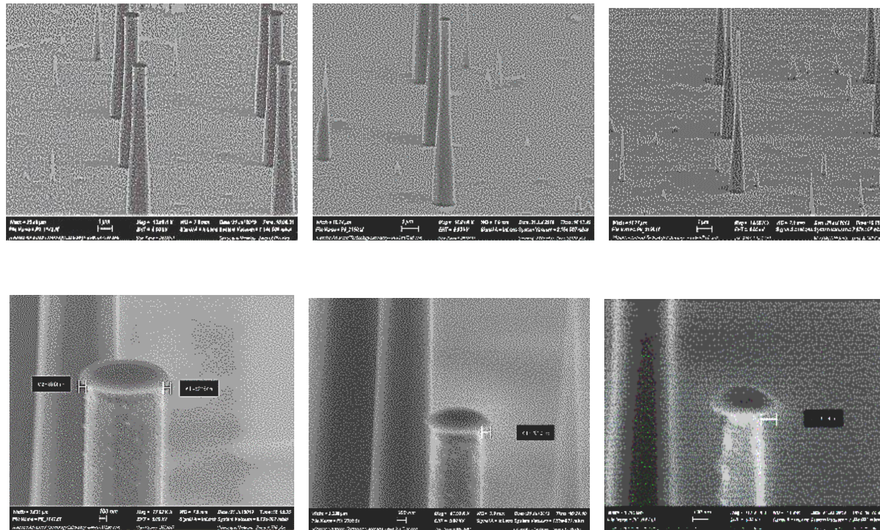

Fig 5.11 SEM image for 40 cycles etches and for 1200, 800, 500 nm Cr mask diameters with the gas ratio of SF_6/C_4F_8 = 22/38, respectively left to right, the lower images are the magnification of the top images

For gas ratio SF_6/C_4F_8 =15/45, the 1200 nm diameter Cr mask has the height of 4.55μm with 0.745-1.259μm diameters and 227 nm undercut while the 800 nm diameter Cr mask has 4.8μm height with 397-827nm diameters and almost no undercut. For the 500 nm diameter Cr mask, the height is 1.86μm, the lower diameter is 426nm. The height is shorter because the letteral etch shortens it. The upper images in Fig 5.12 represent the pillars while the lower ones have the undercut (only the 1200 Cr mask has an undercut). More C4F8 results are in a slower etch due to more passivation in the etch process.

The conclusion of the experiment is summarized in Table 5.1. It is observed that the oxygen cleaning cycle on the substrate results in a more grass free smooth surface and has no effect on taper angle, but there has been a reduction in the etching rate as the cleaning process can reduce the polymer layer accumulated during the etching process and introduce an oxide layer leading to undercut.

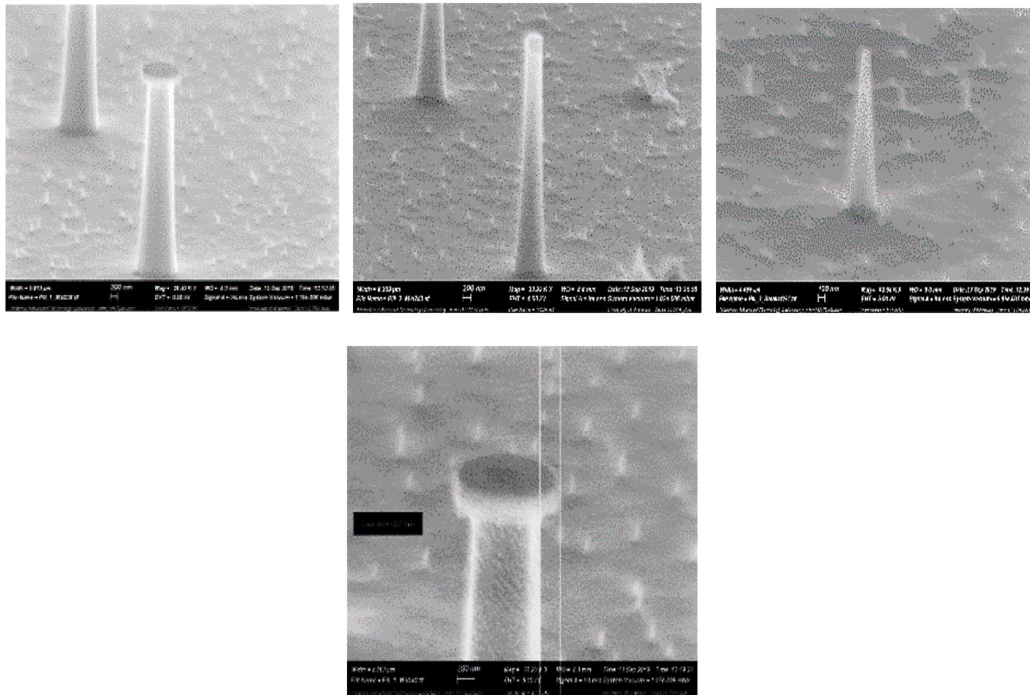

Fig 5.12 SEM image for 40 cycles etches with 500, 800, 1200 nm Cr mask diameters, the gas ratio of SF_6/C_4F_8 =15/45, respectively left to right, the lower image is 1200 Cr mask diameter undercut

Table 5.1 Summarizes the effect of the oxygen plasma cleaning cycle on etching rate and profile

Oxigen Cleanining	SF6/C4F8	Etching Rate (nm/min)	Duration (min)	Mask diameter (nm)	Hight (µm)	Diameter (µm)		Under_Cut (nm)
						top	bot	
No	22/38	715	10	1200	5	1.14	1.5	No
No		715	10	800	5	0.67	1.14	No
No		715	10	500	4.66	0.348	0.814	No
No	15/45	325	20	1200	5.46	1.1	1.5	No
No		325	20	800	5.58	0.627	0.983	No
No		325	20	500	5.7	0.3	0.4	No
Yes	22/38	300	40+7	1200	9.8	1.07	1.79	88
Yes		300	40+7	800	9.8	0.6	1.422	101
Yes		300	40+7	500	9.8	0.311	1.1	138
Yes	15/45	150	40+7	1200	4.55	0.745	1.259	227
Yes		150	40+7	800	4.8	0.397	0.827	No
Yes		150	40+ 7	500	1.86	0	0.426	No

5.2.3.3. The effect of gas ratio on etching rate and etching shape

To test the gas ratio effect on the etching rate and shape, we employ the pseudo-Bosch recipe and change the RF power from 20 W to 50 W, and ICP power from 1200 W to 2000 W, and the SF_6/C_4F_8 gas ratio being 55 / 5, 50 / 10, 40 / 20, 30 / 30, 20 /40, 10 / 50, and 5 / 55. To achieve 3µm depth, a different etching duration is executed for each gas ratio of SF6/C4F8.

There are two main gases in the Bosch process, SF_6 which is responsible for etching while C_4F_8 responsible for passivation. When the sidewall etching exceeds the passivation rate, the isotropic process is more significant as the etching rate is faster. In contrast, when the passivation rate surpasses the etching rate, a thick passivation coating accumulates on the sides, resulting in a mask that reduces the ion exposure area and slower the etch rate. At a critical balance between the etch and the passivation, a vertical wall occurs where the passivation growth is balanced by the etching rate. The process has some limitations such as bottom grass formation, loading effect, and aspect ratio dependent etching. The main two factors are the etch/passivation gas flow rate and time. The same factors forming the outcome etched shape profile. Low SF_6 flow rate results in a smooth surface. In contrast, increasing the SF_6 flow leads to surface roughness.

The etch surface profile is changed from positive to the negative profile when the SF_6 flow rate increased. Also, the etching/passivation ratio cycles are critical for the prevention of grass formation. DRIE parameters need to be optimized for smooth and vertical sidewalls.

There are two main etching directions vertical, and lateral etch. The lateral etch affects the sidewall profile, and it is achieved by a higher flux of ions reaching the sidewalls. The vertical etch is controlled by ions that reach the surface to remove passivation, activate chemical reactions, and enhance sputtering yield. The etch is affected by the bias voltage, the ion density, the gas composition, and the mean free path.

In the pseudo-Bosch process, the etch and passivation steps (as Bosch process) are combined into a single continuous etch. The etching and passivation gases are driven down to the substrate. The ratio is selected to balance the milling rate for the vertical direction ions with extra ions to etch the horizontal passivation layers and go further into the substrate. If lateral direction ions are less than passivation, a protective sidewall layer is developed. Balancing the etch and passivation gas ratios controls both the undercut and the etching angle. The experimental results for the pseudo-Bosch process are tested with different gas ratio and the results are summarised in Table 5.2, square edge in Fig 5.13, pillar with 5µm Cr mask diameter in Fig 5.14, and 1µm Cr mask diameter in Fig 5.15.

Table 5.2 Experimental results for different SF_6/C_4F_8 gas ratio

	SF6/C4F8	Etching Rate	Mask (µm)	Etch time. (min)	Hight (µm)	Diameter (µm)		
						Top	Middle	Bottom
1	55 / 5	2.4 µm/min	5	1.15	1.6	3.6	2.1	3.6
2	50 / 10	2.1 µm/min	5	1.26	1.56	3.8	2.9	3.6
3	40 / 20	1.5 µm/min	5	2.02	1.86	5	4.9	3.8
4	30 / 30	1.1 µm/min	5	2.47	1.9	3.9	3.9	3.9
5	20 /40	600 nm/min	5	5.05	2.2	3.9	4	4.1
6	10 / 50	229 nm/min	5	13.1	2.1	3.9	3.9	4
7	5 / 55	169 nm/min	5	17.1	1.88	4.4	4.5	4.6

The experiment results show that increasing SF_6 will increase the etching rate while low C_4F_8 will result in a heavy undercut. On 30/30 gas ratio, the balance makes the pillar vertical with equal diameters at the full pillar, while more SF_6 will provide a negative taping angle and less SF_6 will provide a positive taping angle. The balance must be between the C_4F_8/ SF_6 adjustment.

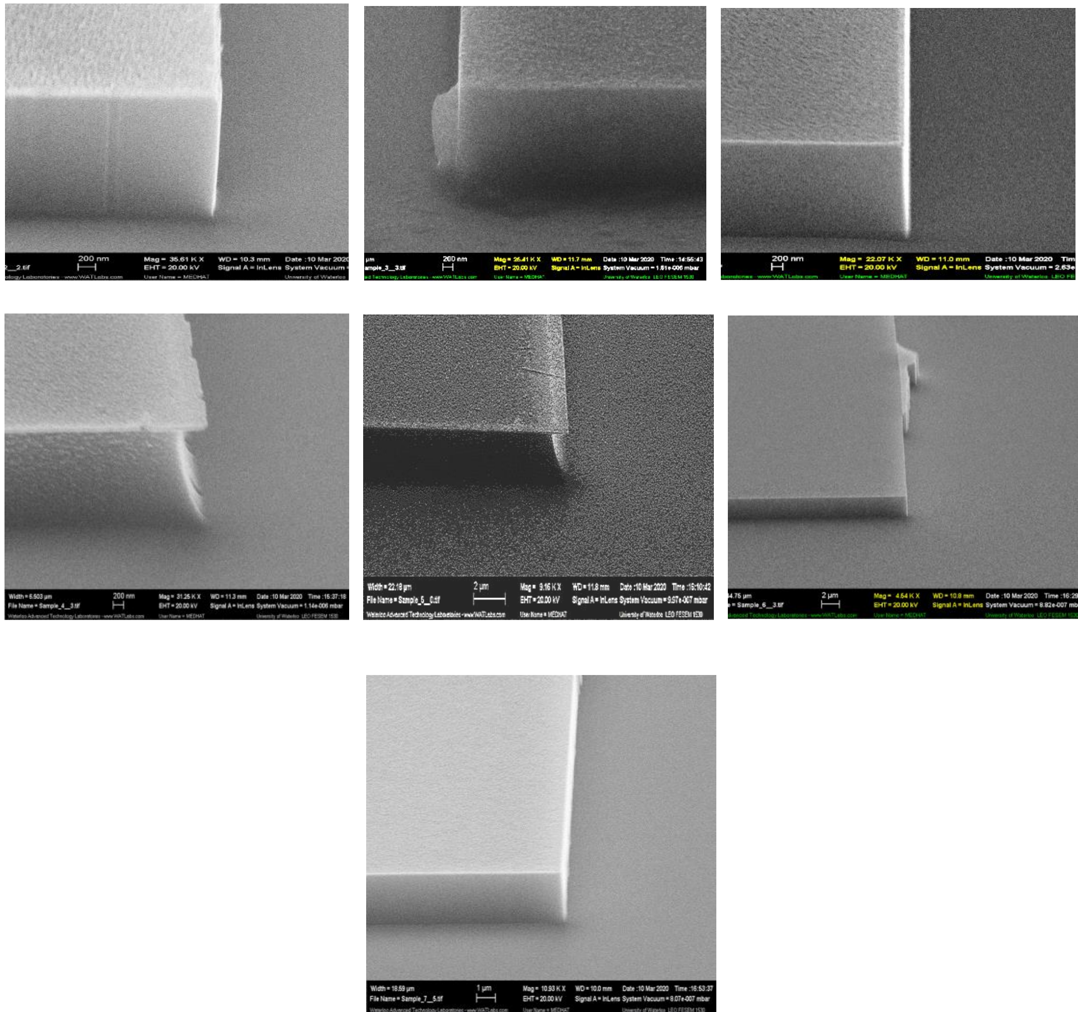

Fig 5.13 SEM image of square edge with Cr mask and SF_6/C_4F_8 gas ratio of 40/20, 30/30, 20/40, 50/10, 55/5, 10/50, and 5/55 respectively left to right and top to bottom

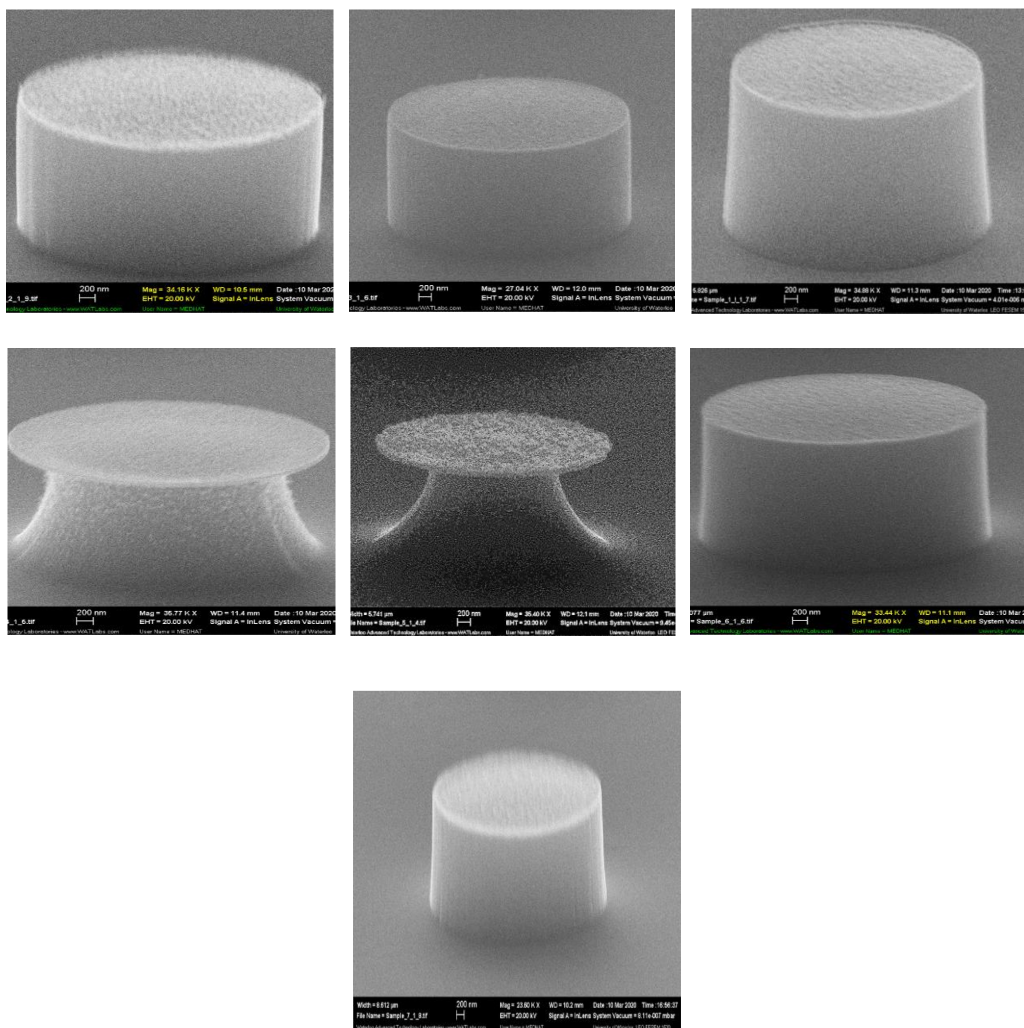

Fig 5.14 SEM image with 5 µm Cr mask diameter, and SF_6/C_4F_8 gas ratio of 40/20, 30/30, 20/40, 50/10, 55/5, 10/50, and 5/55 respectively left to right and top to bottom

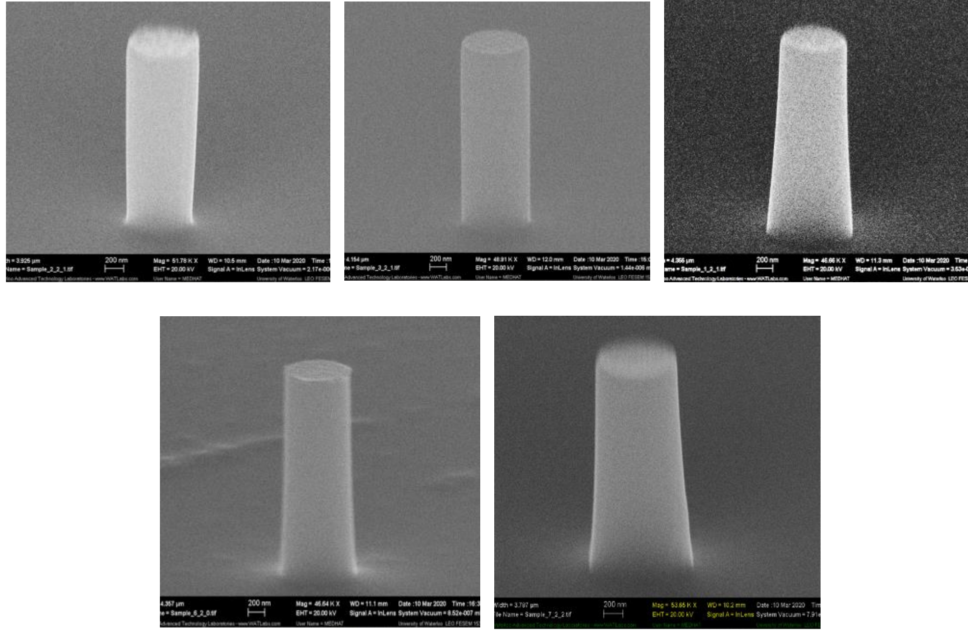

Fig 5.15 SEM image with 1 µm Cr mask diameter and SF_6/C_4F_8 gas ratio of 40/20, 30/30, 20/40, 10/50, and 5/55 respectively left to right and top to bottom, 50/10 and 55/5 gas ratio did not survive

5.2.3.3.1. Further investigation on the gas ratio

Based on the previous result the boundary between the big undercut and no undercut was between the SF_6/C_4F_8 gas ratio of 40/20 and 50/10. This boundary requires further investigation and will be tested in the SF_6/C_4F_8 gas ratio of 42 / 18, 44 / 16, 46 /14, and 48 / 12 with 2 min etch. The results are summarised in Table 5.3, pillar with 5µm mask diameter in Fig 5.16.

Table 5.3 Experimental results for extra SF_6/C_4F_8 gas ratio

	SF_6/C_4F_8	Etching Rate (µm/min)	Mask (µm)	Etch time (min)	Hight (µm)	Diameter (µm)		
						Top	Middle	Bottom
1	42/18	1.2	5	2	2.3	4.1	2.5	4.4
2	44/16	1.2	5	2	2.4	3.9	2.6	2.6
3	46/14	1.3	5	2	2.5	1.8	2.1	3.9
4	48/12	1.4	5	2	2.7	1.2	1.3	3.8

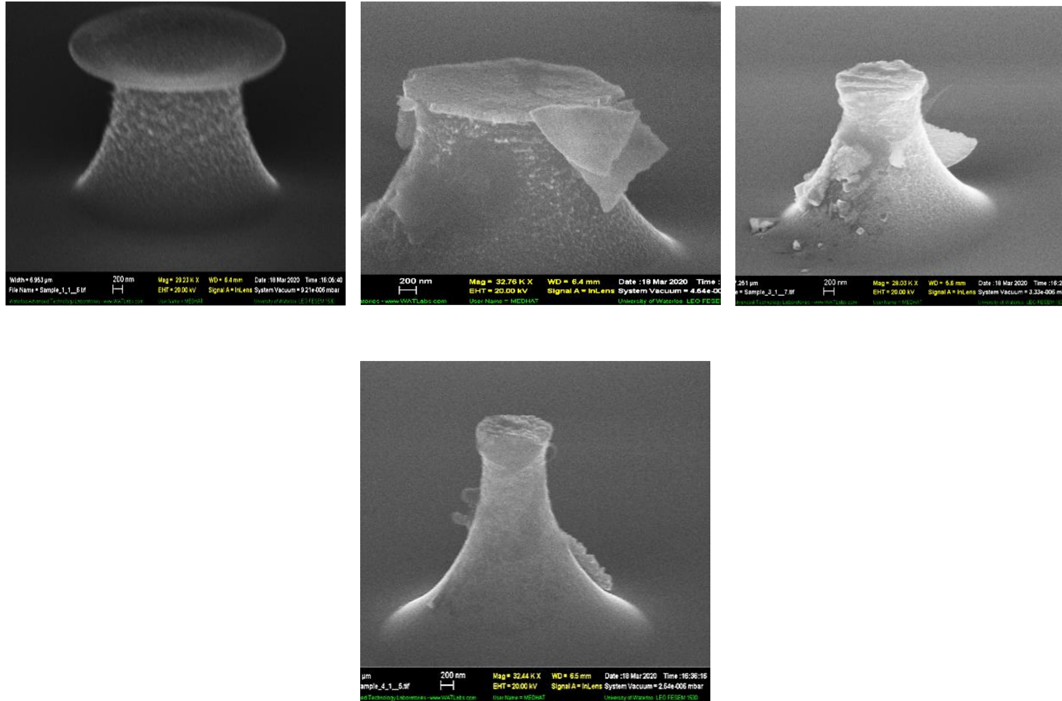

Fig 5.16 SEM image with 5 µm Cr mask diameter and SF_6/C_4F_8 gas ratio of 42/18, 44/16, 46/14, and 48/12 respectively left to right and top to bottom

5.2.3.4. Investigation on cone shape pillars using specific SF_6/C_4F_8 gas ratio of 10/50

We have to investigate the cone shape provided by the gas ratio of SF_6/C_4F_8 = 10/50, as well as the effect of elongated shape on the etching. We create a new sample for this investigation.

Electron beam lithography and lift-off of 80 nm thick chromium (Cr) are executed to form circular patterns with 1.2, 1.5, 2 µm diameters, and elongated circular patterns from one horizontal axis to be 1.4, 1.8, 2.1 µm diameters while the other perpendicular axis is the same. This is performed in a full 4 inches wafer and diced in 1cmx1cm. The pattern is shown in Fig 5.17.

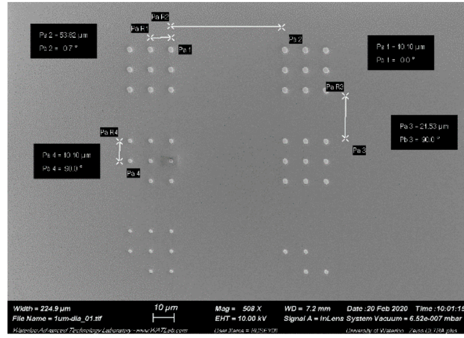

Fig 5.17 The pattern of each sample

The etch with modified pseudo-Bosch recipe has been completed for 40 min with the C_4F_8/ SF_6 gas ratio of 50/10. We find that the etch depth is 2.4 µm, which gives an etching rate of 60 nm/min.

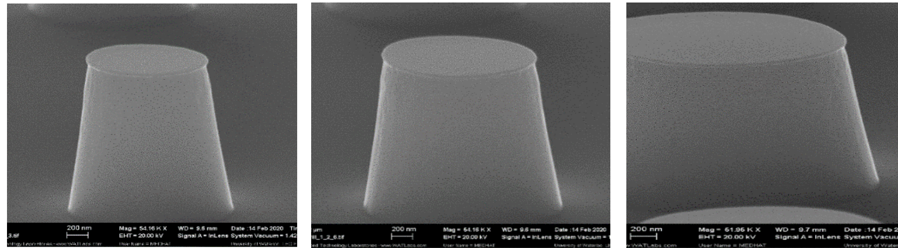

Fig 5.18 SEM image for 40 min etch with gas ratio of C_4F_8/ SF_6 = 50/10 for 1.2, 1.5, 2 µm regular mask diameters left to right respectively

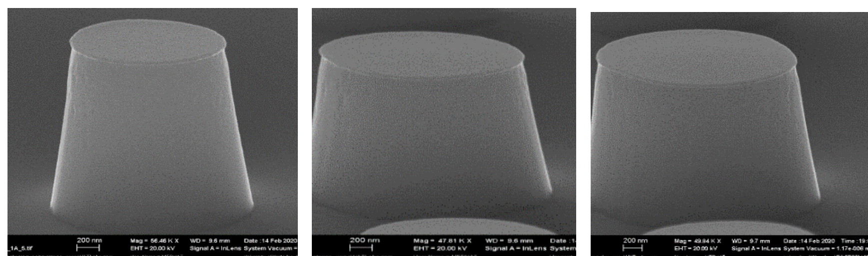

Fig 5.19 SEM image for 40 min etch with gas ratio of C_4F_8/ SF_6 = 50/10 for elongated side mask diameters of 1.4, 1.8, 2.1 µm left to right respectively

The result demonstrates that the cone shaped pillars are generated due to gas ratio C_4F_8/ SF_6 = 50/10. Fig 5.18 shows the pillar with the 1.2, 1.5, 2 µm Cr mask diameters have 1.7 µm height, and 1.2, 1.3, 1.6 µm

(top diameters); 1.5, 1.6, 1.9 μm (middle diameters); 2, 2.2, 1.7 μm (bottom diameters), respectively. For elongated diameter, Fig 5.19 shows the pillar with the 1.4, 1.8, 2.1 μm Cr mask elongated diameters have 1.7 μm height, and 1.4, 1.6, 1.8 μm (top diameters); 1.8, 2, 2.2 μm (middle diameters); 2.6, 2.3, 2,1 μm (bottom diameters). The final observation is that the taping angle is the same for all the different diameters including the elongated one. The slope at all the sides of the cones is 77°.

5.2.4. Dry etch conclusion

To study the effects of RF power, ICP power as well as the oxygen cleaning on RIE Si etching rate and profile, we incorporate a recipe (ICP 1200W, RF 20W, pressure 10 mTorr, temperature 15 °C, C_4F_8/ SF_6 = 38/22 sccm) which has a Si etching rate of 400nm/min. We increase the etching rate to 500 nm/min by raising RF power from 20 to 50 and further increasing the etching rate to 715 nm/min by elevating the ICP power from 1200 to 2000 W. We also add an Oxygen cleaning cycle and switch between the etching and cleaning cycles; accordingly, the etching rate is slower, but the surface roughness and taper angle have been improved.

To investigate the effect of gas ratio on the etch rate and profile, we examine the different SF_6/C_4F_8 gas ratios of (55/5, 50/10, 40/20, 30/30, 20/40, 10/50, 5/55). A further study of the values between 40/20 and 50/10 is performed, including the ratios of 42/18, 44/16, 46/14, and 48/12. Decreasing the SF_6 will reduce the undercut and the etching rate but will have a better shape profile and smoother surface. As a special study, the cone shape fabrication employs the right gas ratio, for both the regular and the elongated diameter, is performed. In conclusion, the gas ratio for SF_6/C_4F_8 = 10/50 is the optimum level to create a cone shape.

5.3. Wet etch

5.3.1. Introduction

Wet etch is used to form high aspect ratio Si structures in many applications. Y. Lee et al. [259] present crystalline silicon deep tunnel with a high aspect ratio using alkali solution for better light trapping and low reflectance solar cells. Using the acidic solution, the etching rate is around ~ 9 μm/min but the aspect ratio

is only 1:1.26. R. A. Morris et al. [260] fabricate <100> Si pillars with an aspect ratio of 20 using mechanical and chemical size reduction. Wet etch can also be combined with other techniques such as focused ion beam milling to achieve a flat top surface or into a 100 nm tip point. These pillars reduce the usage of NaOH and KOH solution at 100 °C and generate an apex surface in the shape of a spherical tip radius of 50–100 nm. The steps and outcomes are shown in Fig 5.20.

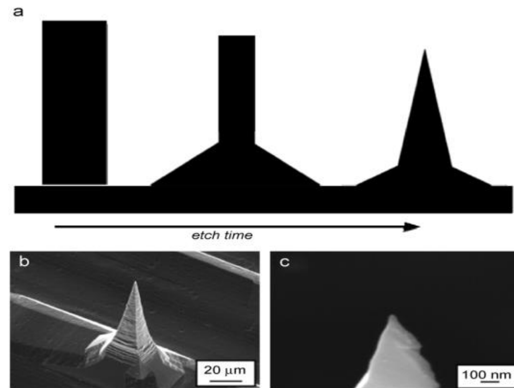

Fig 5.20 (a) Schematic illustration of fabrication steps (b) & (c) the outcome of the process

As the HAR structure is needed, it seems that the combination of dry and wet etch is the best solution. Here, we present a combined method to fabricate a high aspect ratio array by deep reactive ion etching and sharpen it to nanoscale by a wet etching process to employ the advantages of each technique and avoiding the disadvantages in both. Here, we achieve an ultra-high aspect ratio of order 100.

The crystal orientation of silicon and surface roughness is also an important factor for the etching rate. The <111> plane is denser than <110> plane which is denser than <100>; resulting in an etching rate that will be faster in the <100> plane, then slow down in <110> plane, and get slower in <111> plane.

5.3.2. Experiment

A combination of dry and wet etch is used to employ the advantages of both techniques. We start with a silicon 4 inches wafer of <100> surface orientation, clean it with Acetone/IPA, O_2 plasma clean, and then dry it with nitrogen. The double resist layers coat ZEP 520A of 250 nm and 220 nm PMMA resists are spin-coated on the Si wafer and prebaked for 3min at 180°C. EBL is completed by Raith 150TWO using the

parameter of 20 kV, 60µm aperture with a dose of 500µC/cm^2 for a 2X4 array of circles with 1000 nm mask diameter. We also expose a big square of 80 µm x 50µm to examine its edges after etching. The complete exposure is repeated every 1.5 cm in two directions into the full 4 inches wafer.

Following EBL, both resist films are developed by xylene for 2 min and by O_2 clean for 10 sec to remove the residue from the bottom of the pattern. Then, 150 nm of Cr is deposited by Intlvac Nanochrome II e-beam evaporator, followed by lift-off using acetone for roughly 1 h with an ultrasonic bath (medium-power) to form circular patterns with 1 µm radius of the hard mask, then we cut it into 1.5X1.5 cm pieces with the pattern in the middle.

Deep Si RIE etching is carried out using an Oxford ICP380 instrument. 22 sccm SF_6 and 38 sccm C_4F_8 gases are introduced to the chamber, and 1200 W ICP power, 20 W RF power, 10 mTorr pressure at 15 °C are applied. After chromium mask was removed by Cr etchant for 10 min (to remove the 150 nm Cr from the top of pillars array of 10 µm height).

At this stage, the sharpening process can be started by employing a wet etching technique by mixing one unit of diluted hydrofluoric acid HF (HF diluted with distilled water to a concentration of 1:10) with 20 units of undiluted nitric acid (HNO_3) to obtain a mixture at a final ratio of hydrofluoric acid to nitric acid of 1:200. We placed the sample into the mixture for 8 minutes to sharpen the pillars after dipping it in HF 1:10 for 5 seconds to clean the sample from any oxidation.

The etch rate of each step at all the samples is measured by a Veeco Dektak profilometer, and the etched structures are examined by Zeiss Ultra Plus scanning electron microscopy with the samples mounted on 70° tilted stubs.

5.3.3. Results and discussion

We employed double photoresist as a single layer dose have not enough thickness to generate the undercut profile for easy lift-off of the thick metals and uniform Cr mask with a more sensitive bottom layer of ZEP 250A resist.

To achieve a 10 µm pillar, knowing that our recipe etching rate is 400nm/min, a 25min duration is required. Testing the recipe etch for Cr gives an etching rate of 4.5 nm/min, which means that we should have more than 113 nm of Cr. Thus employing 150 nm of Cr will be safer.

Many parameters of the fabrication process are optimized to achieve pillars with high aspect ratios like EBL and RIE parameters. EBL has been tested with many parameters to reach optimum parameters. For RIE, the Bosch process can give a high aspect ratio [261], but the main drawback is the wavy sidewall profile. The Bosch process can be improved to deliver smooth sidewalls in nanostructure fabrication. We modify the Bosch process to non-switching gases with an optimization technique that is calibrated to optimize all the recipe's parameters to achieve the best output results.

The key point in the experiment is that the non-switching pseudo-Bosch process, SF_6, and C_4F_8 gas flow ratio will influence the taper angle of silicon pillars sidewall. Our study previously showed that the gas flow ratio of C_4F_8/ SF_6 = 38/22 sccm led to a vertical profile, so it is chosen to etch the pillars. The silicon plasma etching is carried out to obtain the pillars array. The profile is shown in Fig 5.21 and Fig 5.22. The measured diameters of the top, middle, and bottom part of unsharpened nanoneedles is 755.1nm, 819.8nm, and 755.1nm respectively, i.e. the pillars are nearly vertical.

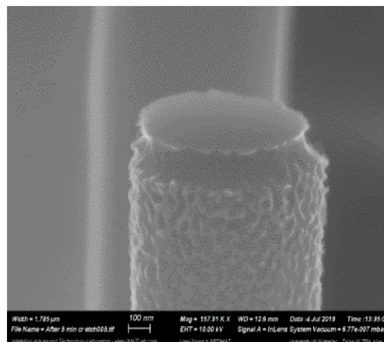

Fig 5.21 A rough sidewall surface of the pillar before wet sharping

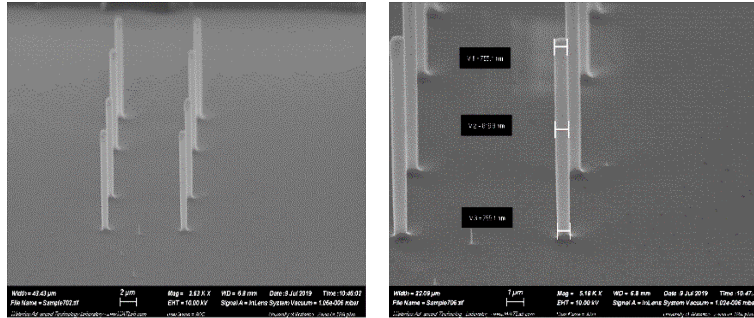

Fig 5.22 (left) nanopillars array before sharpening process (right) detailed information and profile of pillars before sharpening, the diameter of the pillar is 755.1nm

We need a slow etching rate to protect the pillars from damage. To achieve the best result, a combination of HF: HNO_3 with different concentration have been tested for vertical and horizontal etching rate. The result is demonstrated in Fig 5.23 which displays in both the table and the graph. From the etching result, we select HF: HNO_3 as 1:200 gives a low etching rate with no acid limitation.

To produce a smooth surface with a high aspect ratio, the HF should be the limiting factor to introduce more oxidation forming a smooth surface. Many combinations have been experimented to select the optimum result, which comes up to be (HF: HNO_3 as 1:200). Testing this solution on pillar sharping for different times, the optimum time is found to be 8 min to get aspect ratio of 135.

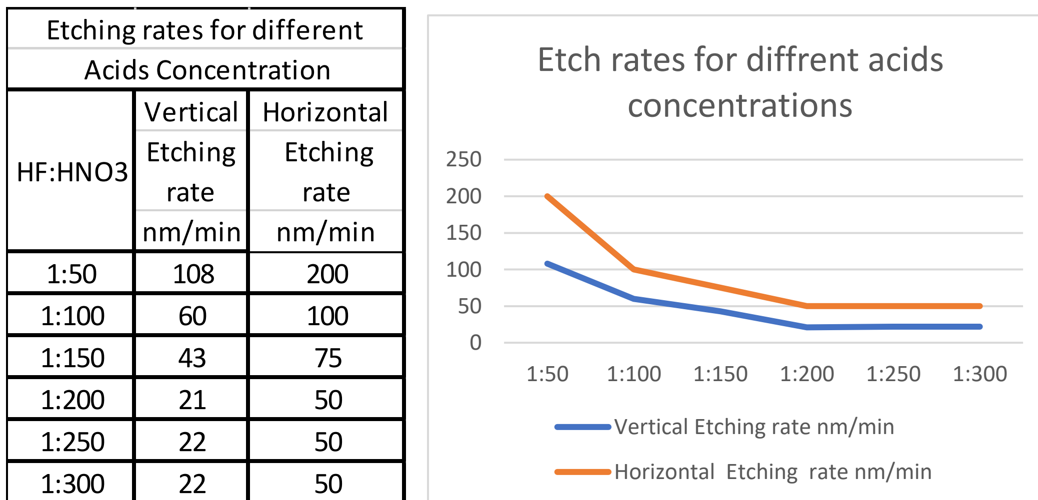

Etching rates for different Acids Concentration		
HF:HNO3	Vertical Etching rate nm/min	Horizontal Etching rate nm/min
1:50	108	200
1:100	60	100
1:150	43	75
1:200	21	50
1:250	22	50
1:300	22	50

Fig 5.23 Etching rates for different acids concentration vs vertical and horizontal etch in nm

After sharpening, the profile is demonstrated in Fig 5.24, and the measured diameters of the top, middle,

and bottom part of sharpened nanopillars are 73.71nm, 221.1nm, and 129.0nm. It is worth mentioning that acetic acid enhances the chemical reaction, so silicon structures will be consumed rapidly in HNA (hydrofluoric, nitric, acetic) solution.

As a result, the shrinkage of the needle tip part is 681.39nm, and the shrinkage on the bottom part is 626.1nm. Because the edge is exposed to the solution in both vertical and lateral directions, the etching rate on the top part is faster than the bottom part as more solution is coming from the top while the bottom limits the reacting solution by the silicon wafer surface.

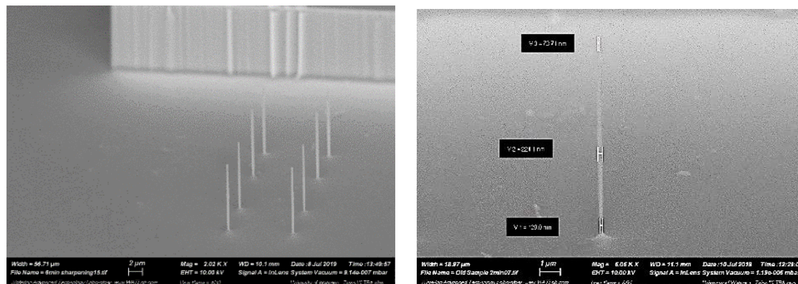

Fig 5.24 (left) nanopillars array after sharpening process (right) detailed information and profile of pillars after sharpening, the diameter of the pillar is 73.71nm

5.3.4. Wet etch conclusion

Our process consists of three major steps: (1) electron beam lithography (EBL) includes transferring the pattern into double photo resistance ZEP 520A and PMMA by the lift-off technique to create the Cr mask, then (2) inductive coupled plasma (ICP) RIE etches the silicon with the protected area of Cr as a mask and finally (3) the resulting pillars are sharpening using wet etch employing HNO_3 and HF with ratio 200:1. The target arrayed pillars length is 10 micrometers and diameter ~100 nm, leading to an aspect ratio of order 100. After dry etching, the nanopillars array with the desired height is accomplished then thinning takes place to the desired diameter using wet etching is performed. The measured tip diameter of sharpened nanopillars is 73.71nm, and the needle height is 10µm. Consequently, this method can successfully achieve the fabrication of ultra-high aspect ratio of silicon nanopillars array and have an aspect ratio of 135.

Chapter 6

Fabrication of HAR AFM tips and nano pillars using FIB (Focus Ion Beam)

6.1. Fabrication of HAR tip using FIB

6.1.1. Introduction

Commercial HAR tips are most popularly fabricated by focused ion beam (FIB) shaping, i.e., milling away the surrounding Si to leave behind a high aspect ratio sharp Si AFM tip. The Ga ion current in FIB must be low to deliver high sharpness, but low current reduces milling speed, noting that a significant amount of Si (order of ~ 5 μm^3) needs to be milled away. As a result, the commercial HAR tips are very expensive, in the range of ~ $100 per each tip. Here our method is to mill away only ~10 nm metal layer (order of 0.01 μm^3 to mill) and use the plasma etching process to transfer the pattern into Si, to form a HAR Si pillar at the tip apex. Since metal deposition and plasma etching are both low-cost batch process, our method is much more cost-effective when multiple tips are processed simultaneously.

6.1.2. Experiment and process discussion

To develop the recipe, a trial is performed on a Si wafer (not on the AFM tip) before applying the technique on the real tip. A schematic of the recipe is shown in Fig 6.1. Fig 6.1 (a) shows the wafer before processing Fig 6.1 (b) illustrations 30 nm of Al deposition, Fig 6.1 (c) demonstrations the second 10 nm of Cr deposition, Fig 6.1 (d) after FIB milling, Fig 6.1 (e) after Al etching using RIE, Fig 6.1 (f) after deep Si etch. Fig 6.1 (g) after wet etch to clean the Cr and Al. The complete recipe consists of four steps. It starts with e-beam deposition of Al and Cr, followed by FIB milling of Cr, then RIE to etch Al, and finally Si RIE. Fig 6.2 shows the expected result when applying the complete technique on the regular commercial tip. Here we used double-layer metal, Cr on top of Al (Cr acts as a metal mask in Al etch), because Al

etches 10 times faster than Cr using BCl_3 gas ICP-RIE, so in principle, ~10 nm Cr mask can become a 100 nm Al mask when etching very deep into Si.

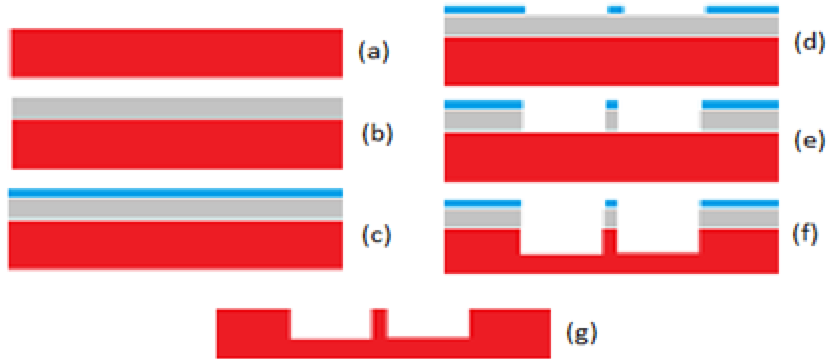

Fig 6.1 Schematic of the process flow to make high aspect ratio pillars using FIB (on Si wafer) (a) shows the wafer before processing (b) displays 30 nm of Al deposition, (c) demonstrates the 10 nm Cr deposition, (d) after FIB milling of Cr 10 nm (Cr acts as a metal mask in Al etch), (e) after Al etching using RIE, (f) after deep Si etch, (g) after wet etch to clean the Cr and Al

Fig 6.2 The expected result when applying the technique on the regular commercial AFM tip

6.1.2.1. Deposition of two materials

As discussed before, two materials are selected for deposition: Cr and Al. The reason for selecting Cr instead of Cr_2O_3 is that the recipe for Al etching using RIE has an etching rate of 115 nm per minute for Al, about ten times slower for Cr, but only ~5 times for Cr_2O_3. As Cr acts as a metal mask in Al etch, this gives the Cr an advantage of higher selectivity. Furthermore, 10 nm of Cr will make the Cr stress have a minor effect.

E-beam deposition of 10 nm for Cr has a rate of 0.5 Å / sec, while 30 nm of Al has a rate of 1 Å/sec. The Cr will be milled by FIB and that is why it is thin and will save the FIB usage time. To get a thicker mask, another material is needed (Al in this case) for pattern transfer to replace the FIB with the RIE etching, saving thicker milling with FIB.

6.1.2.2. FIB milling

For the dose test, Zeiss Auriga FIB/SEM with Ga ions is employed for more than one dose and is tested to select the optimal dose in this case. FIB exposure parameters are 30 kV, 10 pA (measured as 7 pA), and are presented with different milling durations (15, 21, 29, 39, 54, 75, 104, 143, and 197 seconds). The FIB milling area is carried out between the two circles as shown in Fig 6.3 (right) as red area, one with a 2 µm diameter and another with a 0.2 µm diameter, while the location of each milling spots of the 9 different doses place is shown in Fig 6.3 (left).

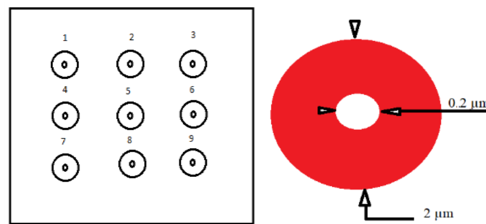

Fig 6.3. (left) Test locations for FIB milling doses (right) close-up view of each circle with the FIB milling the red area

AFM result after the FIB is shown in Fig 6.4, the first 3 holes did not show; only holes over 29 seconds dose have a response (from hole position 4 to 9).

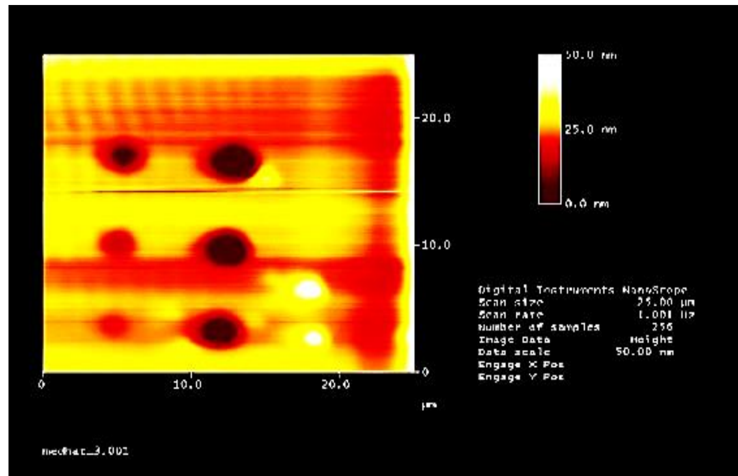

Fig 6.4 AFM results after the FIB milling

6.1.2.3. Al RIE dry etch

A 30 nm of Al should be dry etched. To etch 30 nm of Al, knowing that the recipe has an etching rate of 115 nm/min, a 30 second duration is needed, but as over etch is required 40 seconds is selected. A slight over etch is required to ensure that the Al is completely removed while Cr is still there to protect the rest of the wafer outside the FIB milling. The recipe for Al etches has the parameters: RF power 300W, ICP power 800W, the pressure 1 mTorr, temperature 85 °C, the gas used is Boron trichloride (BCl_3) 50 sccm.

Table 6.1 shows the depth right after the FIB milling and after the Al RIE. After FIB milling, the depth is not enough to be detected till hole number 4, while after Al etch, it shows after hole number 2. We choose to test the tips with 39 seconds as the result is a promising result. Meanwhile, we will go further with 75 and 143 seconds for testing purposes.

Table 6.1 The spot numbers and the depth in nm after FIB mill and Al dry etch

Hole #	Depth after FIB (nm)	Depth after Al RIE (nm)
1	not readable	not readable
2	not readable	not readable
3	not readable	15
4	5	25
5	15	30
6	25	40
7	30	70
8	50	80
9	75	150

6.1.2.4. Si RIE dry etch

The same deep Si RIE dry etch recipe "pseudo-Bosch recipe", previously used in edge tip, will be employed. Since the etch rate of silicon is 400nm/min and the required etching is 700 nm, the etching time can easily be calculated to be 1.45 min. The SEM image of the sample at 70° (tilted angle) is shown in Fig 6.5. The letter 'A' is milled with a size of 100 µm and acts as the guide to find the scanned area. The image resembles grass due to the over-etching of Al, taking into consideration the roughness of the Al surface and the ratio between Al and Cr etch. Fig 6.6 shows the 9 holes result with the same sequence as in Fig 6.3 (right). The HAR Si pillar can be detected on the middle of each spot.

The images are not good in Fig 6.5 and Fig 6.6 because the Al etching time is 45 s, which also etched away Cr and then Al underneath, and the metal is further etched away on Si etching. We adjust Al etch to be 25 seconds in the actual tip.

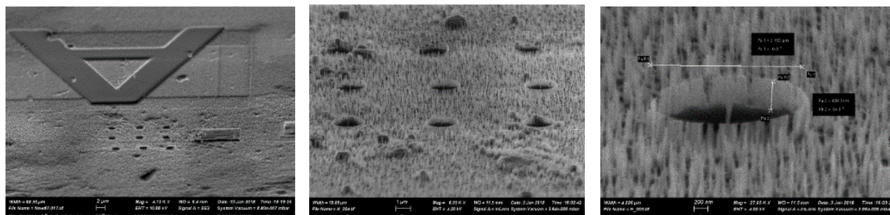

Fig 6.5 70° Tilted SEM images right after Si etch

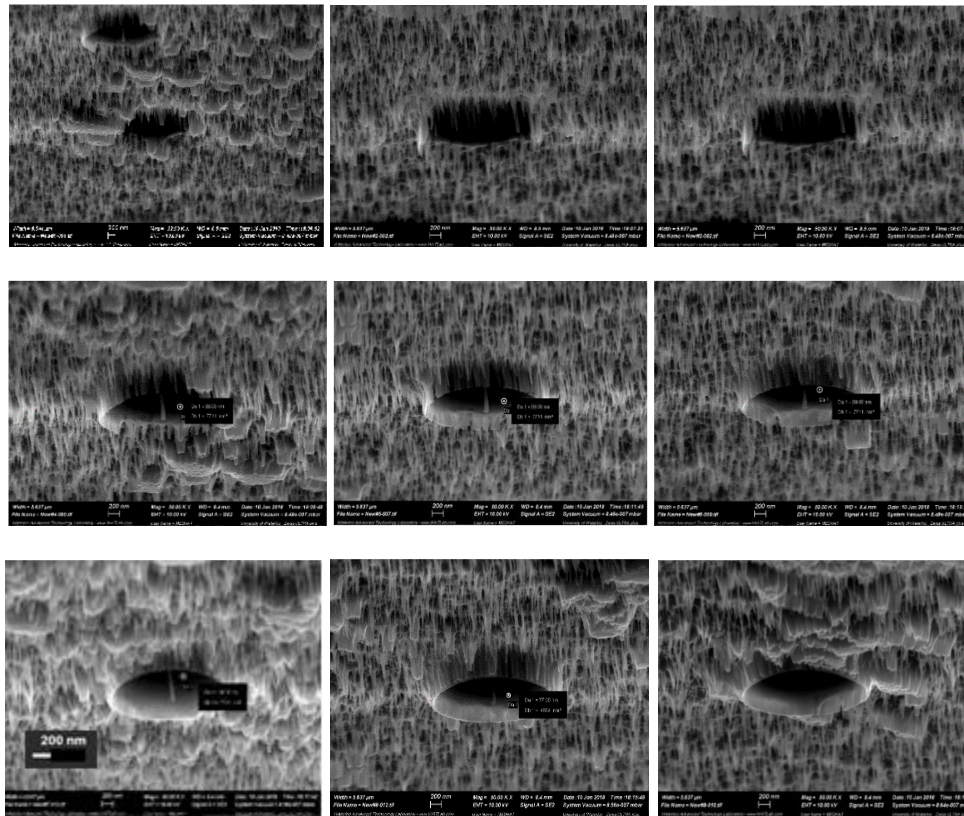

Fig 6.6 70° Tilted SEM images of individual holes arranged as shown in Fig 6.3 (left)

6.1.3. Process transferred to commercial tip

After a careful review of the above result, a change has been introduced on the inner diameter from 0.2 to 0.3 µm and the FIB doses for hole numbers 4 and 6 are selected for testing at the AIO tip. AIO tips are the abbreviation for all-in-one tip (AIO), as it has 4 cantilevers with different lengths giving the user 4 different tips with different characteristics. Fig 6.7 shows the SEM image of 39 s of FIB and 25 s Al etch while Si etch remains the same throughout the experiment (1:45 s). Fig 6.8 demonstrates the results with FIB dose of 75 s and Al RIE etch for 25 s. Fig 6.9 displays the results when FIB dose is 75 s and Al RIE etch is 40 s. Fig 6.10 illustrates effect of FIB dose of 143 s and Al RIE etch for 25 s.

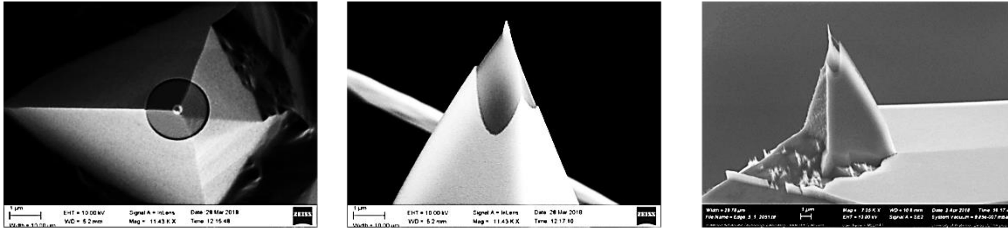

Fig 6.7 (left) Top view after 39 s FIB exposure (middle) 70° tilted SEM images after 39 s FIB exposure (right) 70° tilted SEM images of the final product after 39 s FIB, Al etch for 25 s and Si etch

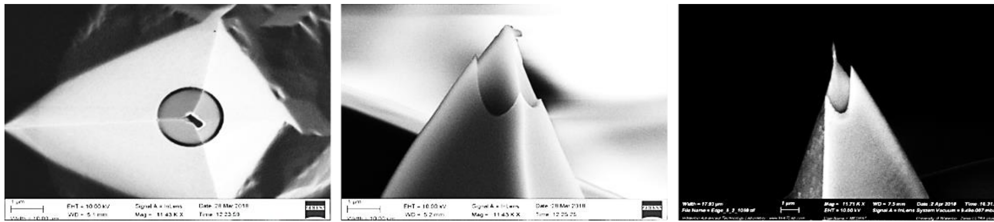

Fig 6.8 (left) Top view after 75 s FIB exposure (middle) 70° tilted SEM images after 75 s FIB exposure (right) 70° tilted SEM images of the final product after 75 s FIB, Al etch for 25 s and Si etch

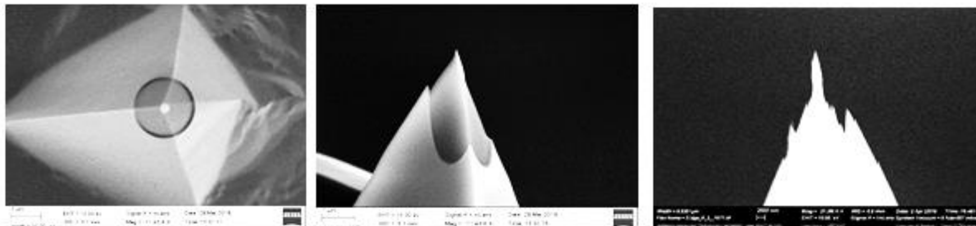

Fig 6.9 (left) Top view after 75 s FIB exposure (middle) 70° tilted SEM images after 75 s FIB exposure (right) 70° tilted SEM images of the final product after 75 s FIB, Al etch for 40 s and Si etch

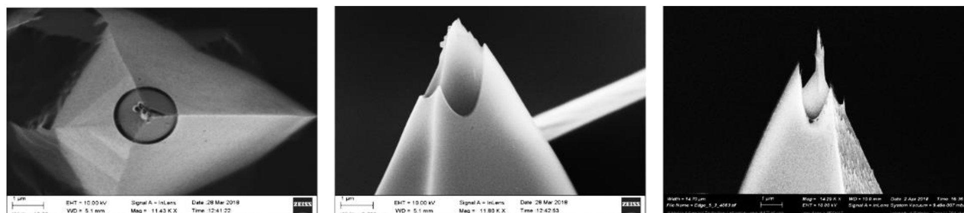

Fig 6.10 (left) Top view after 143 s FIB exposure (middle) 70° tilted SEM images after 143 s FIB exposure (right) 70° tilted SEM images of the final product after 143 s FIB, Al etch for 25 s and Si etch

To ensure the repeatability of this experiment, many tips have been produced and tested with good consistent quality. The recipe for these tips is chosen based on the above results. The recipe starts with the deposition of 30 nm of Al, then 10 nm of Cr, followed by 35, 40, 45 s of FIB milling. Finally, Al RIE etches for 30 s and Si RIE etch for 1.45 min. The resulting tip is as shown in Fig 6.11.

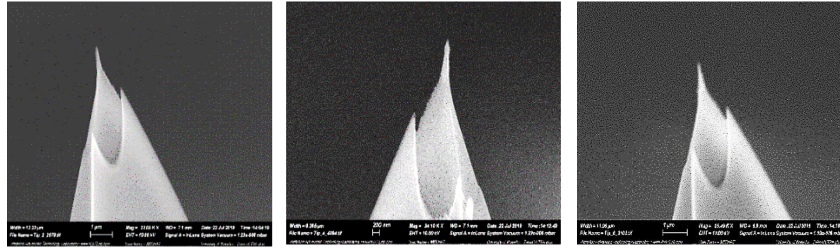

Fig 6.11 70° Tilted SEM images of HAR tip using different FIB doses (left) 35s (middle) 40s (right) 45s

6.1.4. Testing the tip for AFM imaging

The same test previously done is performed using the fabricated FIB HAR tip and the result of the AFM scan is shown in Fig 6.12 (bottom). The test is performed by an AFM tool (Dimension 3100) under tapping mode. The SEM images of the tip are demonstrated in Fig 6.7. The height, width, and length of cantilever is similar to regular commercial tips that perform the scan shown in Fig 6.12 (top). The test shows that the fabricated FIB HAR tip has a much better scan profile and higher vertical resolution than the regular commercial tip as well as proves that the fabricated tip can reach the bottom of the testing sample.

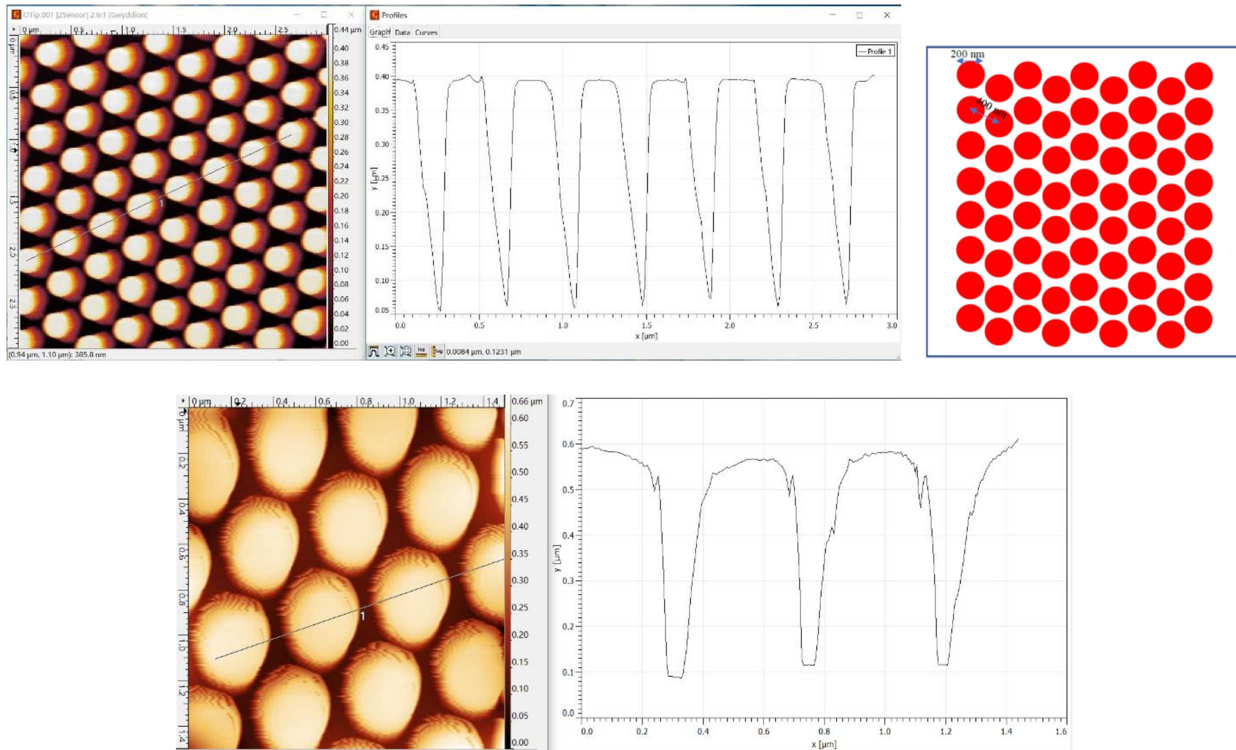

Fig 6.12 (top) AFM scan using regular tip (top right) test sample (bottom) AFM scan using HAR tip fabricated by FIB

6.1.5. Fabrication of HAR tip with reduced FIB milling time

To fabricate the HAR tip using only a fraction of the FIB time, two steps must be accomplished. The first is using a 40-degree angle to deposit the Al and Cr to cover a partial area as shown in Fig 6.13 (A). The second is to mill the metal on the deposited area only, by replacing the full milling area between the circles shown in Fig 6.13 (B), by the partial area shown in Fig 6.13 (C). That will reduce the milling area (the area which is covered by the Al and Cr deposition only) and thus reducing the FIB time.

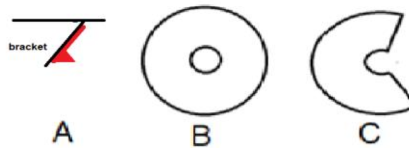

Fig 6.13 (A) Angle deposition (B) FIB complete circle exposure area (C) partial FIB exposure area

The AIO tip has four apexes, two apexes on each side resulting in a different orientation. The area covered with the angle deposited materials has different orientation on each side. As shown in Fig 6.14, two durations for FIB milling with different FIB time, depending on the orientation of the tip related to the material deposition (Al and Cr). The time saving is 45% for the left apex (200° out of 360° circle of exposure), while 20% on the right (300° out of 360° circle of exposure). The average timesaving is more than 35% of the FIB time.

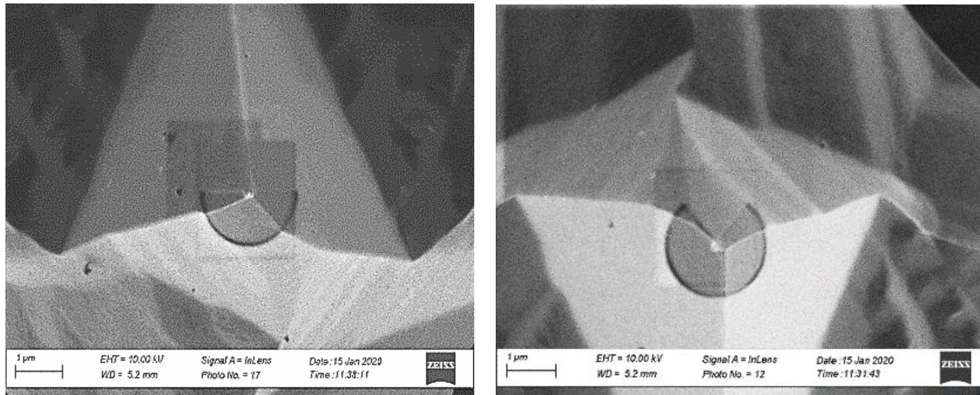

Fig 6.14 Top view of SEM images for two orientations of FIB partial exposures on the metal deposition area only for (left) 200° out of 360° circle of exposure (right) 300° out of 360° circle of exposure

As the AIO AFM tip has 4 apexes, two on each side of the holder, the orientation of the tips in one side is shifted by 180° from the other side, where apexes 1 and 2 on one side with the same orientation, and apexes 3 and 4 having the 180° shift from 1 and 2. When the tip is located at the FIB holder, the beam is looking at a different orientation. The Gallium FIB has 30kV and 10pA (measured as 7 pA), apexes 3 & 4, needs 200 degrees instead of 360 circles of FIB coverage while apexes 1 and 2 need 300 degrees. To cover 200 degrees of 360 degrees (22 s out of 40 s are needed). To cover 300 degrees of 360 degrees (32 s out of 40 s are needed), while overlap is required in all exposures. The final result on both sides of the HAR AFM tips is shown in Fig 6.15. All the other fabricated steps after FIB exposure remains the same as in the FIB HAR tip introduced before.

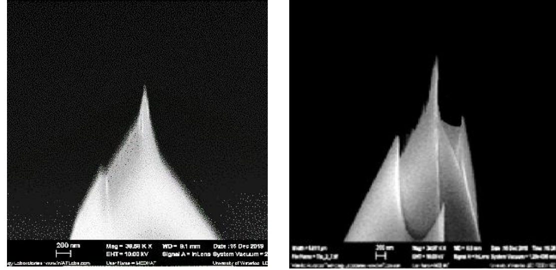

Fig 6.15 70° Tilted SEM images show the final results of the tips after fabrication (left) using 200° out of 360° circle of exposure (right) using 300° out of 360° circle of exposure

The same test as previously performed is done on the fabricated FIB HAR tip shown in Fig 6.15 using an AFM tool (Dimension 3100) under tapping mode. The height, width, and length of cantilevers are the same size as the regular commercial tip which performing the scan as shown in Fig 6.16 (top). The test results are shown in Fig 6.16 (middle and bottom represent 200° and 300° FIB exposure circular angles respectively) demonstrate that the two fabricated FIB HAR tips having the same enhanced scan profile as well as a higher vertical resolution than the regular commercial tip. That test also proves that modified tips can reach the bottom of the testing sample.

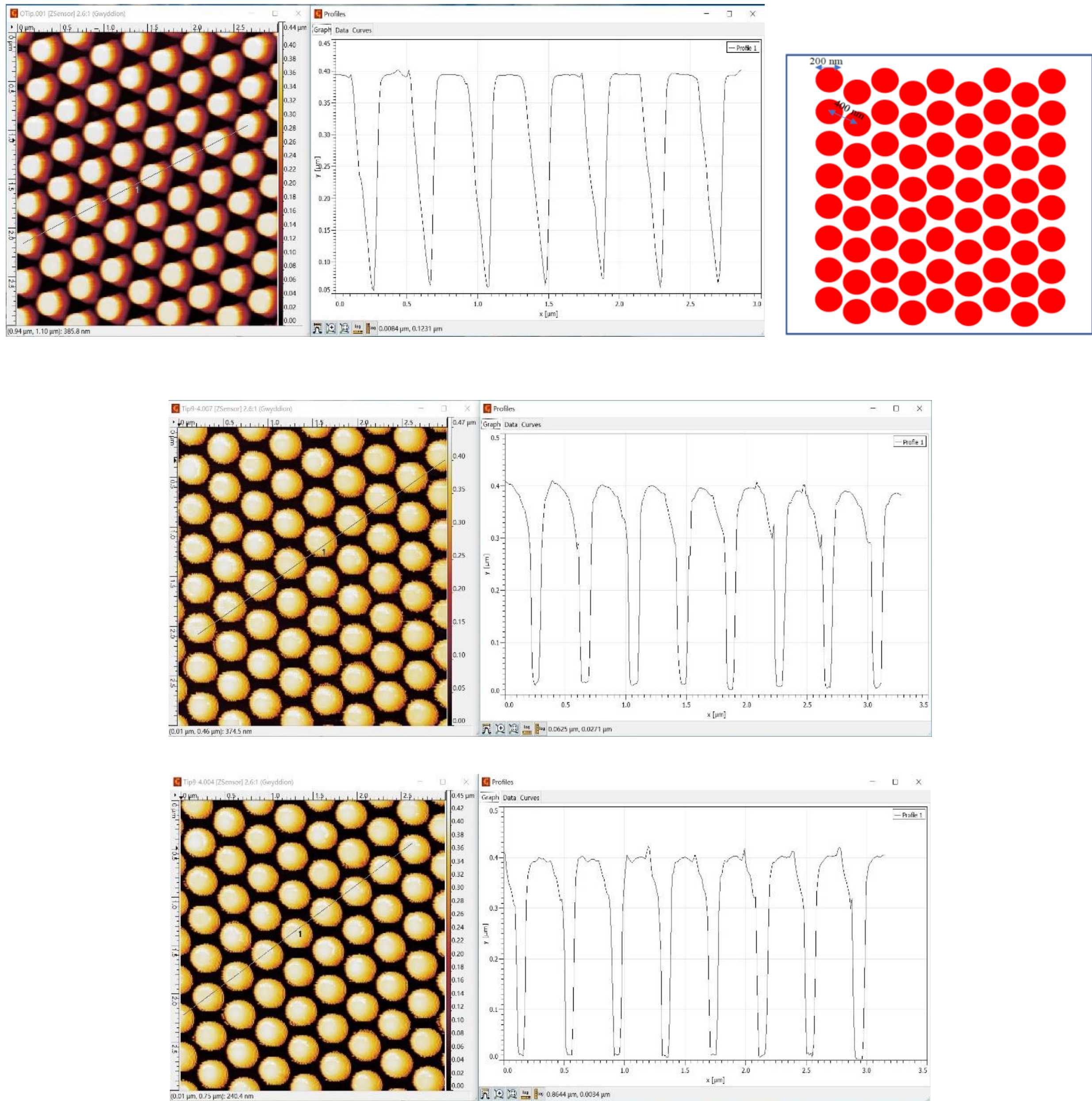

Fig 6.16 AFM scan using (top) regular tip (middle) the 200° partial exposure tip (bottom) 300° partial exposure tip, where (top right) is the testing sample

6.1.6. Semiautomatic fabrication of HAR tip using Focused Au and Si Ion Beam

Fabricating the FIB HAR tip using a semiautomatic way, will maintain the quality and reduce the cost of the skilled fabricator who operates the FIB. We need to switch to a programmable FIB tool. We select RAITH ionLINE, which is programmable and can fit a 4 inches tips wafer (388 tips) and milling all of them

sequentially. The other advantage of this FIB tool is that it can detect the highest point of the tip apex and use it as a center for the milling circle.

But we must recalibrate the process for RAITH ionLINE FIB, as the ions used are not Gallium but Gold (Au) or silicon (Si). The e-beam evaporation and the two steps RIE will stay the same and can be performed to the full 4 inches wafer.

6.1.6.1. Fabrication of the tip

To select the FIB dose, we start with a 2 of 2X2 cm Si wafer (one for Si ions test while the other for Au ions test), deposit 30 nm of Al then 10 nm of Cr on the top of Al. For selecting the optimal FIB dose, we create a 4X4 array of increment FIB doses at each 2X2 cm Si wafer. The FIB is milling between two circles, the outer circle diameter is 2µm with an inner circle diameter is 0.2 µm, on each spot at the 4X4 array with 10 µm center to center. The doses arrange are shown in Fig 6.17 (A).

The RAITH ionLINE is programmed with the dose instead of the time (as Zeiss Ga FIB). The starting dose for testing the Gallium was 5 second at 8pA for a 2µm diameter. The dose = I X t / area = 8pA X 5 s/ π $(1\mu m)^2$ = 1280 $\mu C/cm^2$

A test for Si and Au starts with the same dose at 1280 $\mu C/cm^2$ and increments by a factor of 1.36 from 1 to 16, which gives a final dose of about 128912 $\mu C/cm^2$ (~100 times of the starting dose). The doses will be arranged with the dose position as shown in Table 6.2.

Table 6.2 Hole position and related FIB dose

Hole Position	1	2	3	4	5	6	7	8	9	10	11	12	13	14	15	16
Dose (µC/cm^2)	1280	1740	2367	3219	4379	5955	8099	11015	14980	20373	27707	37682	51248	69697	94788	128912

After depositing the Al and Cr, FIB executes the above doses using both Si and Au ions. The resulting wafer after the two steps of etching is shown in Fig 6.17 (A) for the dose spots distribution, (B) SEM scan for Si ions experiment (C) SEM scan for Au ions experiment. The AFM result is summarized in Table 6.3

(left) for Si and (right) for Au after FIB, after Al/Cr etch, and after Si etch. The FIB parameters are 35KV, 14pA for Si ion, and 6.84pA for Au.

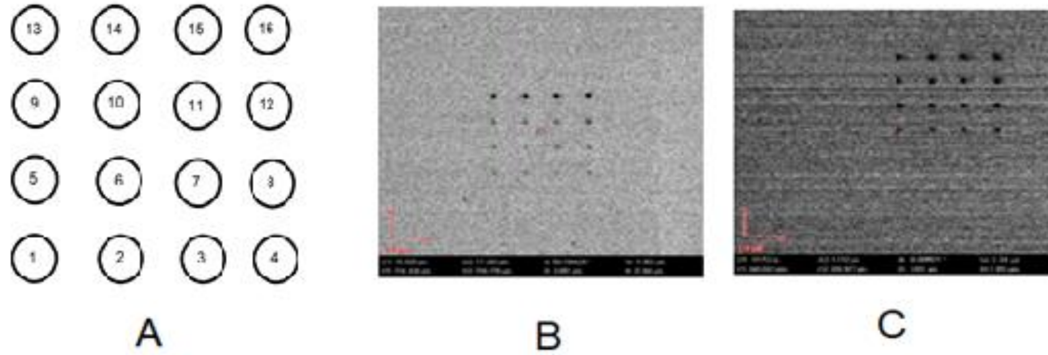

Fig 6.17 (A) Exposure pattern for FIB (B) SEM scan for Si ion experiment (C) SEM scan for Au ion experiment

Table 6.3 AFM depth after ion implantation, after Al RIE etch and after Si RIE etch for both Si FIB (left) and Au FIB (right) samples, (NR = not readable)

Si Gun	Sample 1				Au gun	Sample 2		
Position #	After FIB (nm)	After M RIE 25s (nm)	After Si RIE 1.45 min (nm)		Position #	After FIB (nm)	After M RIE 25s (nm)	After Si RIE 1.45 min (nm)
1	NR	NR	NR		1	7	NR	NR
2	NR	NR	NR		2	8	NR	NR
3	NR	NR	NR		3	12	NR	NR
4	NR	NR	NR		4	10	NR	NR
5	NR	5	10		5	15	NR	20
6	NR	10	20		6	18	50	50
7	NR	15	30		7	35	50	50
8	NR	20	35		8	90	50	50
9	NR	25	35		9	60	50	50
10	NR	28	35		10	60	80	150
11	NR	30	40		11	67	100	150
12	NR	35	40		12	101	180	180
13	NR	40	50		13	74	100	150
14	3	40	60		14	78	150	200
15	5	50	75		15	78	200	200
16	7	60	100		16	80	200	250

From the above results, it seems that the Si ion is a good candidate for milling as the ion dose is proportional to the milling depth; however, Au ions are implanted in the wafer and acts as an etching mask to prevent Al etching as demonstrated at sample 6 to sample 9, thus Au ion is not good for this purpose. Ion implantation of Au will be explored later in this chapter, but the Si will go further to create the HAR Tip.

Fig 6.18, Fig 6.19, Fig 6.20 and Fig 6.21 demonstrate the experiment's output for different parameters, including the recipe for each one (the FIB dose, Al etch time and Si etch time).

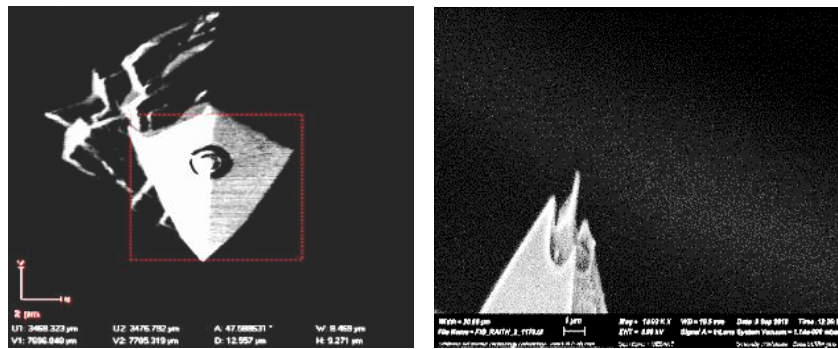

Fig 6.18 (left) Top view of the tip after FIB exposure (right) 70° tilted SEM image of the final result of the fabricated tip with 14 pA and128 mC/cm^2 FIB dose (5 min), Al RIE etch for 25s, and Si etch for 1.45 min

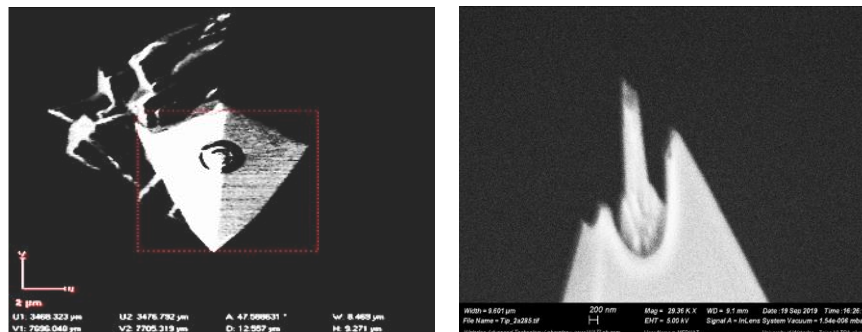

Fig 6.19 (left) Top view of the tip after FIB exposure (right) 70° tilted SEM images of the final result of the fabricated tip with 14 pA and 256 mC/cm^2 FIB dose (10 min), Al RIE etch for 25s, and Si etch for 1.45 min

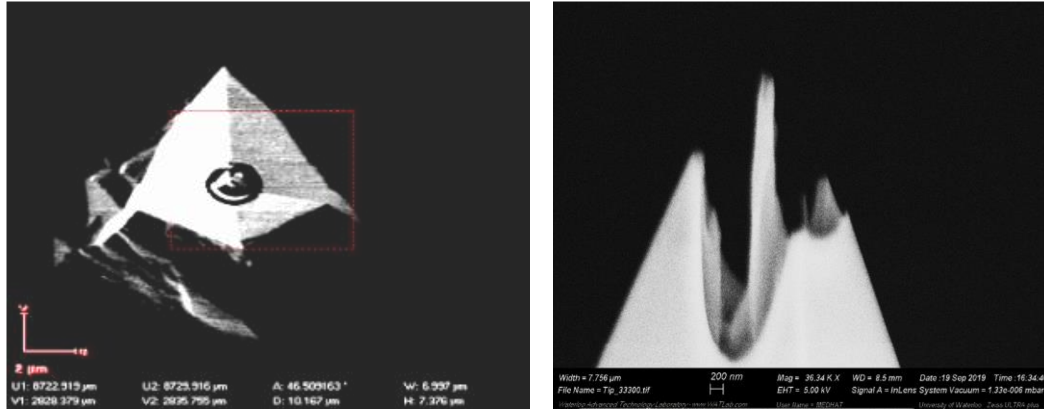

Fig 6.20 (left) Top view of the tip after FIB exposure (right) 70° tilted SEM images of the final results of the fabricated tip with 30 pA and128 mC/cm^2 FIB dose (2.30 min), Al RIE etch for 25s, and Si etch for 1.45 min

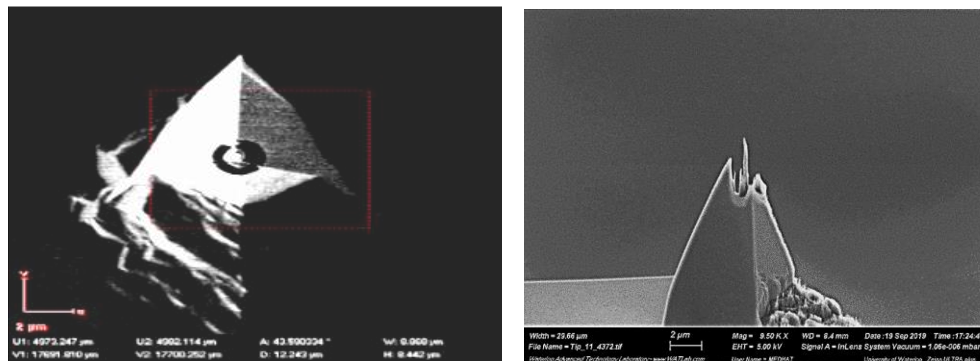

Fig 6.21 (left) Top view of the tip after FIB exposure (right) 70° tilted SEM images of the final results of the fabricated tip with 30 pA and 256 mC/cm^2 FIB dose (5 min), Al RIE etch for 45s, and Si etch for 1.45 min

After a careful review of all the above results, all the tips seem acceptable, but, a decision has been taken that 30pA with the doze 128 mC/cm^2 is the optimum as it has a shorter FIB exposure time (2.5 min FIB exposure per tip). Increasing the current will no longer be a valid option as the beam size will not keep the apex as shown in Fig 6.22 which demonstrates the next step of the current increase (75 pA).

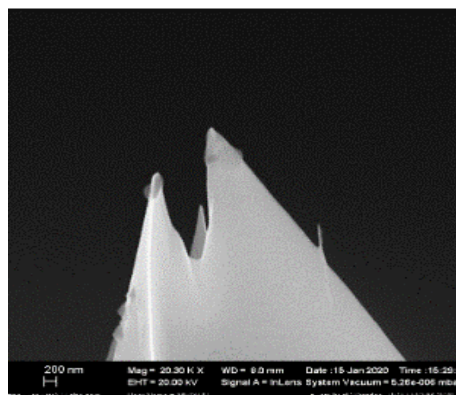

Fig 6.22 70° Tilted SEM images of higher beam current exposure (75 pA)

We recommend that the outer circle diameter for the FIB milling should be 3 μm instead of 2 μm because the edges around the tip are too high; however, this will occur at the expense of FIB time. Also, the Al etching is 25 or 45 seconds. Although 25 s is acceptable, we will choose 30 s to be on the safe side.

The only drawback of this experiment is the FIB milling time for each exposure (minimum of 2.5 min for each apex). Knowing that the dose is proportional to the area, which means that, if the milling circle increases to 3 μm, the milling time will be almost doubled. The Ga FIB is more time efficient (only needs 40 seconds per apex).

The reason Ga FIB is preferred over Si is the spattering yield which is proportional to the atomic weight of the FIB ions[262]. The Ga atomic weight is 70 while Si is 28, the unit is Dalton (symbolled as Da, or u) where 1 Dalton is defined as 1⁄12 of the mass of a single carbon-12 atom at rest. That makes Ga is faster than Si by almost 70/28 times.

6.1.6.2. Results and tip testing

The same test previously performed using the fabricated FIB HAR with Ga, will be repeated for the tip made with Si FIB (with 30 pA, 128 mC/cm^2). The tested tip is shown in Fig 6.20. The test is done using the AFM tool (Dimension 3100) under tapping mode. The height, width, and length of cantilevers are the

same size as regular commercial tips that perform the scan shown in Fig 6.23 (top left). The test result for the fabricated HAR AFM tip is shown in Fig 6.23 (bottom). The scan demonstrates that the fabricated FIB HAR tip has a better scan profile as well as a higher vertical resolution than the regular commercial tip. The test also proves that the fabricated tip can reach the bottom of the testing sample.

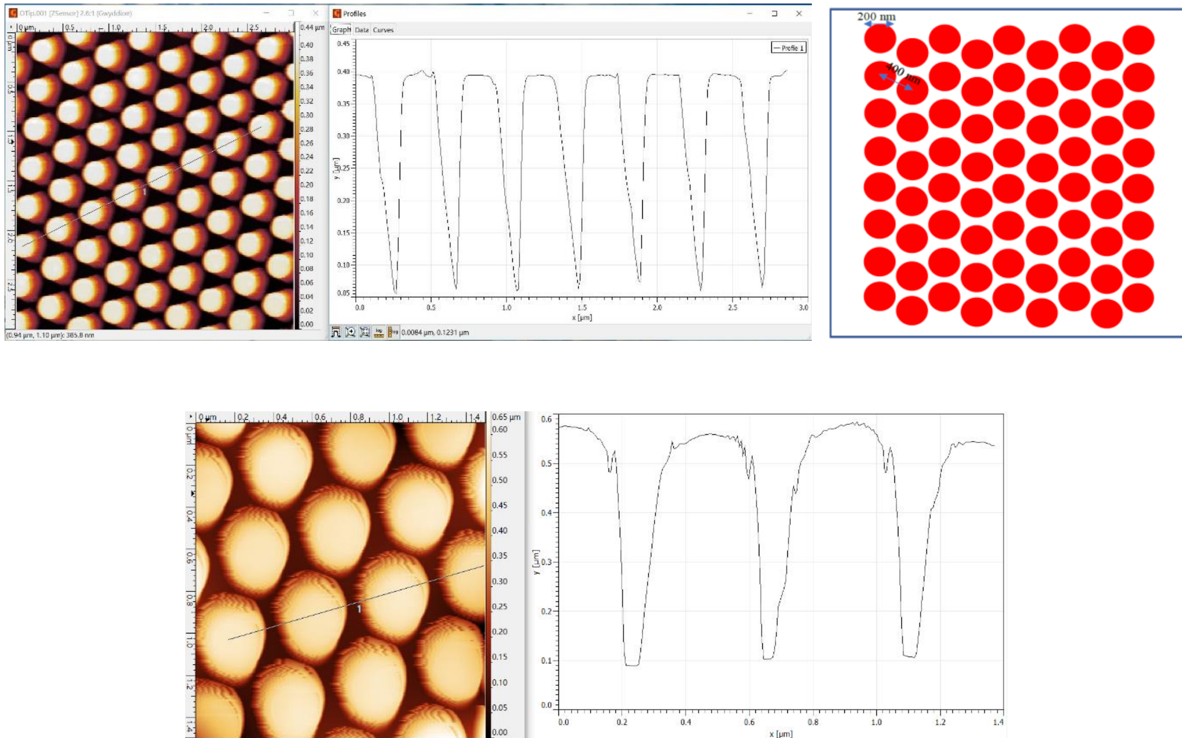

Fig 6.23 AFM scan using (top left) regular tip (bottom) fabricated HAR AFM tip, while (top right) is the testing sample

6.2. Ion implantation

6.2.1. Introduction

Ion implantation is employed to change the substrate surface of many materials and it is important to a wide variety of technologies. It is a significant technique for semiconductor fabrication and other industries, as well as the basic research and future applications. Ion beams are also modifying optical properties of dielectric materials to create optical waveguides and related photonic devices as well as three-dimensional structures like piezoelectric nanostructures.

The main basis of silicon fabrication is the capability of patterning a mask on the silicon surface and use this mask to etch a feature in the silicon [263]. Many varieties can be used to define this pattern in resist, including ultraviolet, electron beam, or nanoimprint lithography [264] [265]. On the other hand, direct removal of silicon by a focused ion beam can avoid the need to resist but limit the material removal, feature size, and HAR [266] [267].

The focused ion beam is a well-established technique both in science and industry [268]. FIB systems can be used in multiple ways including direction milling, ion implantation, FIB assisted etching, and FIB induced deposition [269] [270]. Ion beam resolutions are below 10 nm and offer flexible and highly reproducible patterning [271] and thus become more widely available. But structural damage and contamination of the milled materials are issues that often limit the use of FIBs. This damage depends on the ion energy, ion dose, incident angle, and substrate material density and structure.

FIB can also be used to implant gallium (Ga) into silicon to define nanoscale structures directly without resist and achieve high throughput and high aspect ratio structures [272] [273] [274] [275]. The first announcement of high Ga masking selectivity is done in the wet etching of the silicon over Ga-doped silicon [276] [277] [278] [279]. Gallium FIB treated silicon has selectivity against the non-treated region in both plasma [280] [281] [282] [283] [284] and alkaline wet chemical etching. Etch stop limitation of FIB implantation is lattice damage and contamination due to implantation species that will change mechanical and electrical properties.

A combination of focused ion beams (FIB) for gallium mask implantation and KOH solution is used for etching [285]; the result is shown in Fig 6.24. It has an implant dose range of 1 pC μm^{-2} to 25 pC μm^{-2} with a 1000 pA ion beam current. Followed by potassium hydroxide (KOH) anisotropic wet etch of a 30% KOH solution at 78 °C to achieve an etch rate of 1 μm/min. The wet etch process has a higher throughput with greater etch selectivity than the photolithographic techniques [286] [287].

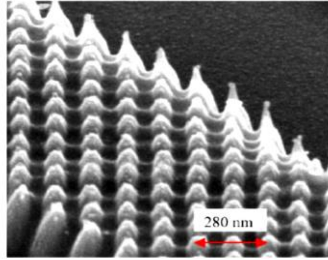

Fig 6.24 SEM image for the structural profile of the implant array after etching

Further research proves that Ga based masking is a good candidate for deep reactive ion etching (DRIE) and produces micron scale features with nanometer scale etch depths [288]. Schmidt et al [289] demonstrate the resistance of gallium treated silicon towards plasma etching with no etching of micro or nanostructures confirmed. Qian et al [290] fabricate microstructures using gallium implanted silicon as a mask in RIE for low aspect ratio structures with micrometer dimensions. Further research of Ga based masking in deep reactive ion etching (DRIE) has been executed ever since.

The etch selectivity between the un implanted and Ga implanted increases gradually to 2.56 with Ga ion dose increase up to 1.59×10^{16} ions cm^{-2}. Meanwhile, the etch rate selectivity decreases with further increase in ion dose as well as the surface concaves due to ion sputtering. Ga implantation into SiO_2 is resistant to wet etching and reactive ion etching [291].

To experiment with the ion implantation, two important factors should be considered [292] [293]. The first one is the thickness and depth of the Ga implant, while the second is the max heights of the silicon structures after etching.

Fig 6.25 is a simulation using SRIM/TRIM performed for implanting Ga+ ions into silicon which introduces the effect of the beam voltage on the thickness of the implantation layer and implantation depth [294] [295]. As an example, from the simulation, the implantation of 30 kV beams damages the top 15 nm of silicon creating amorphous silicon while the 20 nm below is a Ga rich amorphous silicon.

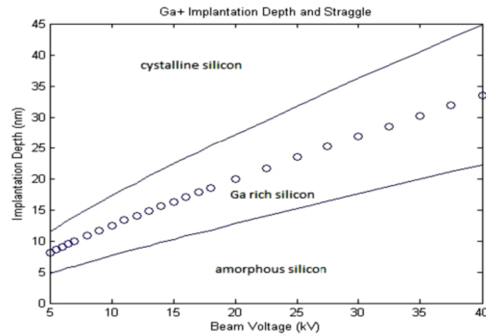

Fig 6.25 Ga+ implantation depth vs beam voltage

N Chekurov et al. [296] study the Ga+ ion dose and related etch resistance. They start with 300 μm×300 μm square and exposure different Ga+ doses ranging from 10^{15} to 10^{17} cm^{-2}, then etch it at different etch times to achieve the etch resistance on each depth. Fig 6.26 plots the heights of the etched silicon structures vs the gallium dose on various etch times. From this plot, the threshold value of 2×10^{15} cm^{-2} is needed before any etch resistance, and eventually, the dose of 2×10^{16} cm^{-2} delivers the highest etch resistance and can produce a silicon structure of 80 μm high[297].

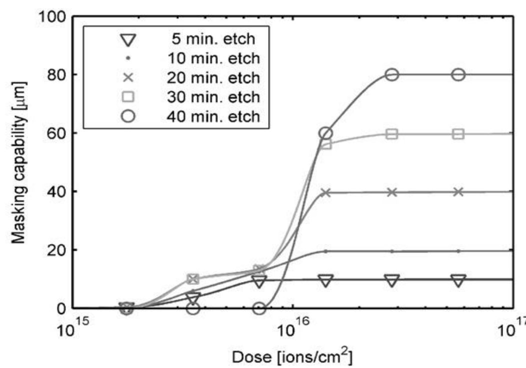

Fig 6.26 The step height versus gallium dose with various DRIE etch times

To know the limitation of the dose implantation, include the greatest etch depths and selectivity, they use a Monte Carlo simulation and find out that dose/height is a straight line up to $1X10^{16}$ cm^{-2}, then it curves and leads to a steady-state of $3X10^{15}$ cm^{-2}. Maximize the Ga implantation on the top layer, more doses must be implanted. However, further exposure of the beam after a certain point will gradually saturate the

exposed area. Fig 6.27 represents the Ga amount existing in the silicon sample as a function of total ion flux for a 30 kV beam. It is the total flux of Ga atoms minus the sputtered Ga atoms by Monte Carlo simulation. At low doses, the areal dose implanted is linear with total flux for a low concentration of Ga. As the sputtered depth approaches the mean implantation depth of 27 nm, the total concentration of Ga in the sputtered material increases. At 28.4 nm the areal concentration is 10^{17} Ga atoms cm^{-2}. This is lower than the total incident flux by 16%. This Ga sputter keeps increasing from this point but needs an enormous amount of incident flux to increase the implanted concentration. The maximum implanted value at a steady state is calculated to be 3×10^{17} Ga atoms cm^{-2} which is depending on the ratio of the mean implantation depth and the sputter yield.

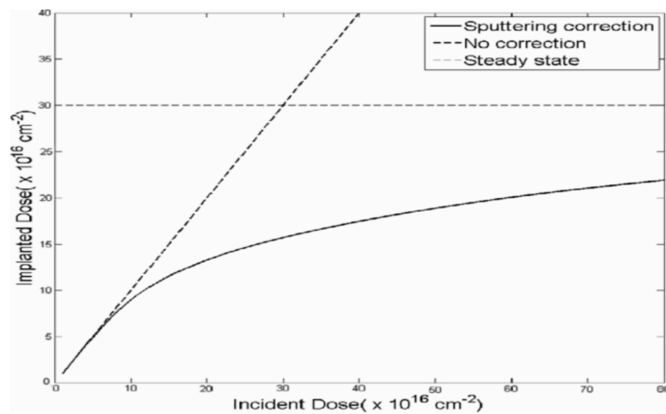

Fig 6.27 The plot of implanted dose as a function of incident dose, with the limiting value is 3×10^{17} Ga atoms cm^{-2}

The implant can be in Si or metal/ metal oxide such as Al, Cr, Al_2O_3, CrO_x, besides the use of photoresist. For example, the direct resist patterning with ion beams has atomic elements such as H+, He+, Be+, and Si+ [298]. The advantages over the electron beam lithography are a better resist sensitivity and lower proximity effects but have a limited penetration depth of light ions into the resist layer which reduces the resist thickness and resulting in a lower aspect ratio. FIB ion implantation modifies the organic photoresist's resistance to dry etching in an oxygen plasma. Ion beam inhibited etching (IBIE) is done by FIB implanting

a high dose of a reactive element into a resist, followed by oxygen reactive ion etching (RIE) which represents a negative image in the exposed areas. As an example, PMMA (polymethyl methacrylate) resist with the implanted area using ion species, such as Si+ and Ga+, has a significant reduction in the etching rates employing the oxygen RIE process. Also, patterning of nonorganic materials such as gallium implanted titanium layers remains unetched in an SF_6 plasma etch. Gallium implanted in glass has a 30% lower etching rate.

Many papers [299] investigate the three-dimensional distribution of germanium atoms in silicon after implantation through an aperture of 10 nm diameter. M D Henry et al. [300] have tested the ion implantation and its application to produce nanoscale features. The pattern arranges the squares from 50 nm to 500 nm with 50 nm increments. They implement the Ga ions doses column from 5.3×10^{15} cm^{-2} to 1.96×10^{17} cm^{-2} with a dose increment of 1×10^{16} cm^{-2}. Following Ga implanted anisotropically etched (pseudo-Bosch) in an Oxford Instruments PlasmaLab 100 inductively coupled plasma reactive ion etcher (ICP RIE) 380. the array is etched with ICP power of 1200 W, RF power of 10 W, table temperature of 15 °C, chamber pressure of 10 mTorr, SF_6/C_4F_8 gas flow of 33 sccm/50 sccm, and a measured forward bias of 54 V. The final results are shown in Fig 6.28.

To be able to know the threshold of the higher edged feature related to the Ga dose, an array of squares has been implanted with different doses and etched for different times to get the threshold dose to determine the maximum height of each structure as shown in Fig 6.29.

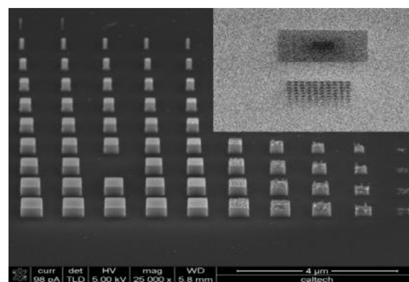

Fig 6.28 SEM image of Ga implanted nanoscale dose array in silicon, the implant image for visual mark and the full-scale image

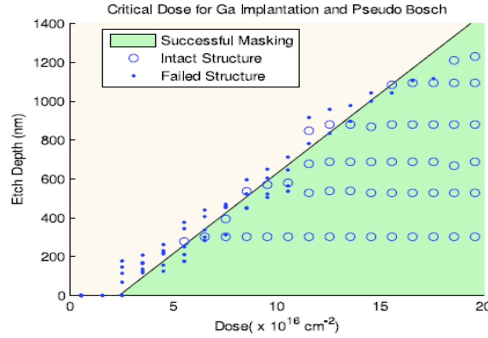

Fig 6.29 The threshold of variable Ga implantation doses and various etch times

---

6.2.2. Ga ion implantation experiment and discussion

A silicon 2X2 cm wafer is prepared and cleaned. Then, 20 nm Al_2O_3 deposited using the ALD technique, followed by 50nm SiO_2 employing PECVD technology. Ga FIB exposed steps are done with the parameters; 200nm diameter (1µm period) with energy: 30 kV, Current: 5 pA (Actual), dwell time: 1µs, exposure times 2 s, 4 s, 6 s, 8 s, 10 s, 15 s, 20s, 30 s and 40 s in consequence of 5 exposures in each column and two columns for each exposure time. The beam dot size is 10nm, the beam period is 5nm, the field of width is 20µm. RIE is used with non switching Bosch for 50s to etch the SiO_2 followed by Al etch (BCl_3 70 sccm, Cl_2 5 sccm, pressure 5 mTorr, RF 250 W, ICP 800 W, temperature 22°C) for 18 s to take off Al leaving the Ga implantation. Finally, non switching Bosch for 2 min to etch the silicon. The SEM for final results is shown in Fig 6.30 where the 2 second exposure in the left two columns and the 40 seconds exposure on the right two columns. Fig 6.31(left) demonstrate two columns of the 2 s exposure while in Fig 6.31 (right) show the two columns of the 40 s exposure. All the other doses that come in between are irrelevant as shown in Fig 6.30. Table 6.4 will calculate all the doses related to the time per second from the FIB current. The equation for dose calculation is:

Dose = current x time / Area

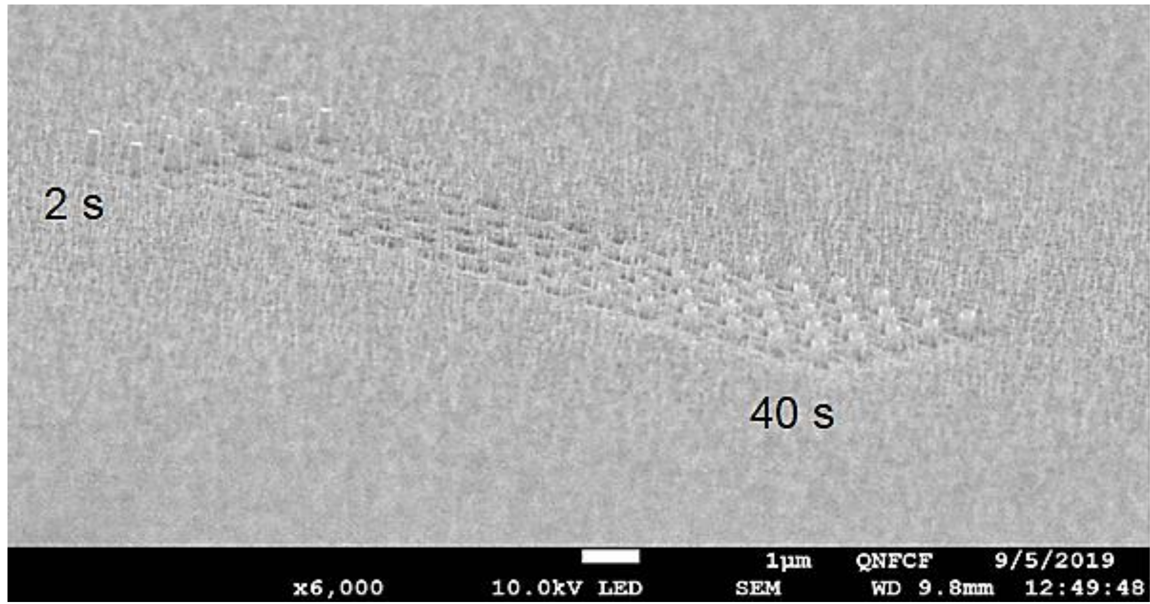

Fig 6.30 70° Tilted SEM images of the sample after the recipe is done. 2 second exposure on the two left columns and 40 seconds on the two right columns, while all the other doses come in increments doses every two columns in between

Table 6.4 Dose calculation for the related time of exposure

Time in Sec	2	4	6	8	10	15	20	30	40
Dose ($10^{16}cm^{-2}$)	1.3	2.6	3.9	5.2	6.5	9.75	13	19.5	26
Dose ($mC\ cm^{-2}$)	0.8125	1.625	2.4375	3.25	4.0625	6.09375	8.125	12.1875	16.25

Based on Fig 6.27 the 2s dose will be in the implantation range and provide nano pillars shown in Fig 6.31 (left). The higher dose will fall in the milling area up to 15s. Higher than 15 s will fall into the area of saturation which is in ion milling and implantation together and thus creating the nano-pillars shown in Fig 6.31(right).

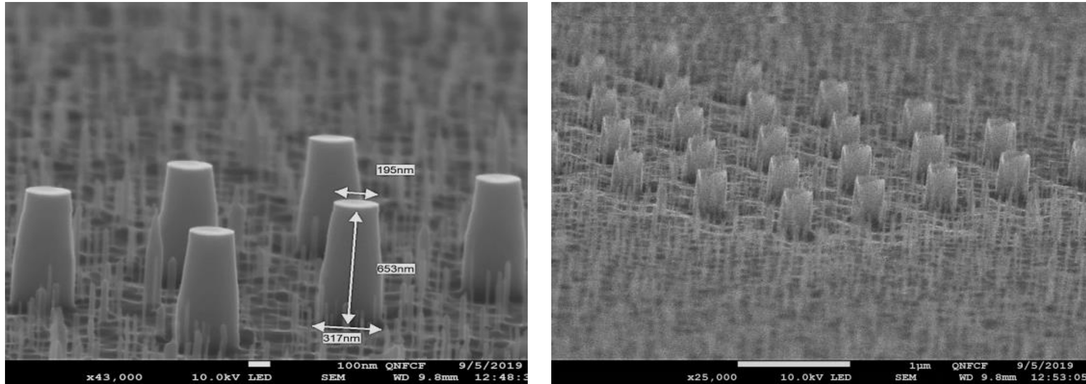

Fig 6.31 70° Tilted images of (Right) SEM image of the final result for 2 second Ga FIB exposure (Left) SEM image of the final result for 40 second Ga FIB exposure

We use a double mask 20nm Al_2O_3 deposited using the ALD technique, followed by 50nm SiO_2 employing PECVD technology. The chlorin base which etch Al, can etch the Ga implantation while the fluorine base which etch Si will be masked by the Ga implantation. We deposit Al as a mask to be able to etch the silicon with fluorine, while SiO_2 is protecting the Ga implantation by Al mask.

6.2.3. Au FIB ion implantation

FIB employs a different liquid metal as ion source (LMIS) such as Ga, Au, Be, Si, Pd, B, P, As, Ni, Sb, … etc. All these metals can be tested for ion implantation. Ion implantation getters the gold in silicon [301] [302] [303], used for the fabrication of modern semiconductor devices. Silicon wafers and devices have been implanted with gold ions and thermally processed in the 1073-1243 °K temperature range. The authors forming nanoscale droplets on the surface after annealing step using FIB implantation of Ga ions into Si <100> and Si <111> substrates to grow GaAs nanowires at defined positions by molecular beam epitaxy instead of the lithographic process [304] [305] [306] [307].

Based on the previous experiment on HAR AFM tip using the FIB employing Au as milling, we observe that Au can be used as an implant and act as a mask. The target is to fabricate the HAR AFM tip employing FIB ion as an implantation mask. To do so, repeating the Au FIB calibration experiment with implantation

in mind (not milling). RAITH ionLINE with Au source ion is used, which is programmable and can fit a 4 inches tip wafer (388 tips) and Au is automatically implanted. The other advantage of this FIB tool is that it can detect the highest point of the tip apex and use it as a center for implantation circles. The e-beam evaporation and the RIE two steps can be executed in batches to the full 4 inches wafer of tips.

6.2.3.1. Experiment and discussion

To select the right material to implant the ions, a comparison between Cr and Al is needed. We start with 2 pieces of silicon 2x2 cm Si wafer, deposit 30 nm of Al on one of them, and 30nm of Cr on the other one. To choose the optimal FIB dose, we create a 4x4 array of increment FIB doses at each 2x2 cm Si wafer. The FIB is implanting Au in a circle of 200 nm diameter with 10 µm distance between them as shown in Fig 6.32 (a).

The RAITH ionLINE is programmed with the dose instead of the time. We used 35 kV and aperture of 30 µm to give a current of 44pA. We expose 200nm circles as shown in Fig 6.32 (a). The starting dose is 1280 µC/cm^2 which increment by a factor of 1.36 from 1 to 16 and the final dose is 128912 µC/cm^2 (~100 times of the starting dose). The dose is arranged with the 4X4 array as shown in Fig 6.32 (a) and the position/dose is demonstrated in Table 6.5.

Table 6.5 Spot hole position and related FIB exposure dose

Hole Position	1	2	3	4	5	6	7	8	9	10	11	12	13	14	15	16
Dose (µC/cm^2)	1280	1740	2367	3219	4379	5955	8099	11015	14980	20373	27707	37682	51248	69697	94788	128912

After depositing the Al or Cr (one metal per each of the two wafers), FIB is achieved at the above doses for Au ions. Then two step etching is performed on each wafer, one for either Cr or Al for the full 30 nm (4 min of Cr etch or 25 s for Al etch), where over etch is required (etching rate for Cr is 12nm/min and for Al is 115 nm/min), then Si etch for 1.45 min (etching rate for Si is 400 nm/min). The result is shown in Fig 6.32 (b) for Cr deposited wafer and Fig 6.32 (c) for Al deposited wafer.

Si etch recipe is (ICP 1200, RF 50, gas ratio of C_4F_8:SF_6 = 45:15 sccm, temperature 15°C, pressure 10 mTorr)

Cr etch recipe is (ICP 600W, RF 200W, Cl_2 50 sccm, temperature 50°C, pressure 5 mTorr)

Al etch recipe is (ICP 800W, RF 300W, BCI_3 50 sccm, temperature 22°C, pressure 1 mTorr)

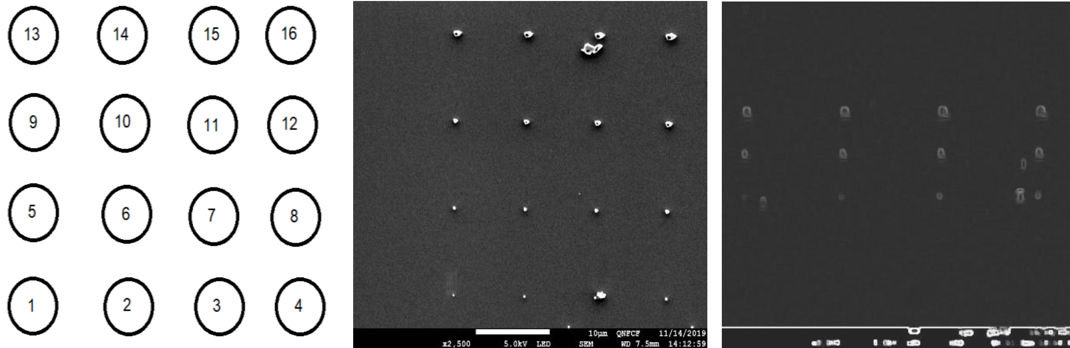

Fig 6.32 (a) Exposure pattern for FIB (b) Cr sample (c) Al sample

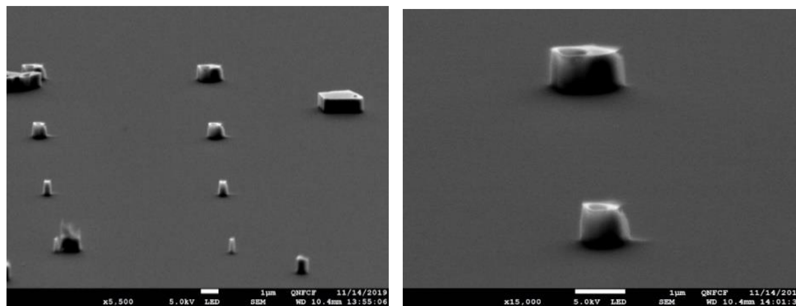

Fig 6.33 Cr sample, 70° tilted SEM images of (right) top right is spot# 16, (left) top is spot# 16

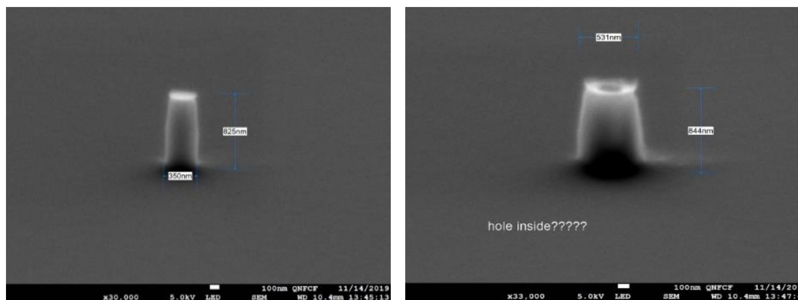

Fig 6.34 Cr sample, 70° tilted SEM images of (right) is spot# 5, (left) is spot# 9

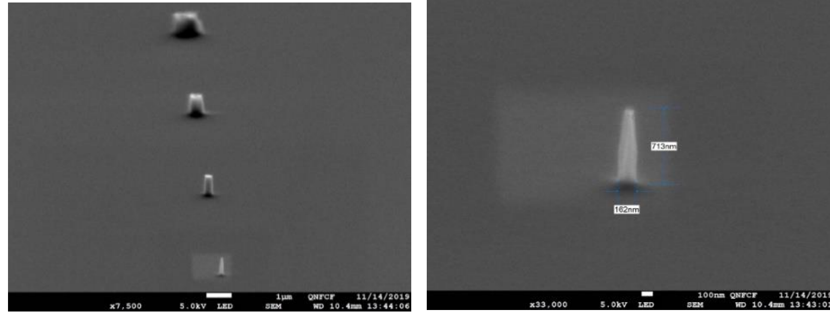

Fig 6.35 Cr sample, 70° tilted SEM images (right) the first one from the bottom is spot# 1, (left) is spot# 1

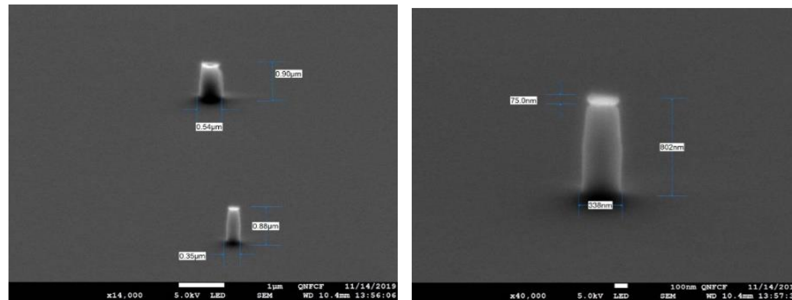

Fig 6.36 Cr sample, 70° tilted SEM images (right) the bottom is spot# 4 (left) is spot# 4

Fig 6.33 to Fig 6.36 demonstrate some of the SEM images of the final results with Cr deposition sample. After a careful review of all the above results, the optimum result is spot#4 for 3219 $\mu c/cm^2$. This implantation is done in 200nm diameter and the result is 880nm high and 338nm base diameter.

6.3. Conclusion

In this research, HAR tips are fabricated using a FIB as a milling machine. We demonstrate a direct fabrication method involving FIB and RIE to convert a regular pyramidal shaped probe into the HAR probe. That occurs systematically with the reduction of FIB milling volume from 0.5 μm^3 to around 0.01 μm^3 and is replaced with RIE in batch style. The result is a semi batch style of HAR tips while minimizing the time of FIB for individual tips; then the tip batches are processed through two steps of RIE, where the HAR batch is accomplished. The tips have been tested by AFM and the result shows a higher vertical resolution

than the regular commercial tips and it can reach the bottom of the testing sample. Further successful work has been performed to fully automate the process using a programmable FIB.

Also, this chapter demonstrates the use of FIB patterns in both Ga and Au implanted as an etch mask. FIB mask writing is used for the lithographic process to protect silicon against fluorinated plasma etching. This work is limited to nanoscale patterning of silicon, but it can also be extended as an etch mask for other materials. We demonstrate the use of Ga FIB, and find that 1.3×10^{16} ion/cm^2 (equivalent to 812.5 $\mu C/cm^2$) dose is the optimum dose for Si as an ion implantation mask of 200 nm diameter and get nanopillar of 653 nm high with the base diameter of 317 nm. We also find that 3219 $\mu C/cm^2$ is the optimum dose for Au FIB implantation. This implantation is done in 200nm diameter and the result is nanopillar with 880nm high and 338nm base diameter. This technique can be applied to a regular commercial tip to transform it into a HAR tip.

Chapter 7

Conclusion

This thesis is focused on nanofabrication and its application of high aspect ratio AFM tips as well as HAR nanopillars. Seven projects based on nanofabrication have been performed.

Project 1: We present a simple repeatable and low-cost batch to fabricate the edge AFM probes. This method is applied to a regular commercial probe and produces an edge tip by a Cr_2O_3 mask on one side of the tip and etches away the Si from the other side to reveal the apex position. The AFM test shows a clear location of the probe. Sharping this tip can be obtained by the thermal oxidation sharpening process.

Project 2: We successfully introduced a method to fabricate the high aspect ratio AFM probes in batches. The main procedure is to form a small Cr_2O_3 dot mask on the tip apex of each tip by overlapping Al at the top of Cr_2O_3 then etching Cr_2O_3 followed by Al and leaving only the Cr_2O_3 on the apex to etch the silicon underneath and to create the HAR tip. This process is applied to regular commercial tips and successfully gain high aspect ratio (HAR) tips in the range of 15:1. AFM test shows that the HAR tips have a significantly better image quality compared to regular commercial tips. This method is accomplished in a batch and lithography-free process which is cost effective and with much higher throughput.

Project 3: Our oxidation study concludes that the regular commercial tip two-step oxidation of 950°C for half to one hour each, yields the best tip sharpening result of an apex diameter (between 2 to 5 nm). Any further steps after the second step are either redundant or the apex gets wider. The SEM cannot be accurate in the range of 2 – 5 nm measurement even using 300k magnification. Besides, SEM with 20K volt high tension results in charging and moving the tip image quickly, and thus catching the image promptly was difficult.

Project 4: In this project, we use a pseudo-Bosch recipe (ICP 1200W, RF 20W, pressure 10 mTorr, temperature 15 °C, gas ratio of C_4F_8/ SF_6 is 38/22) which has an etching rate of 400nm/min. We increase the etching rate to 500 nm/min by raising RF power from 20 to 50W. Further increase of the etching rate to 715 nm/min is accomplished by elevating the ICP power from 1200 to 2000 W. Also, adding an oxygen cleaning cycle and switching between the etching and cleaning cycles, make the etching rate slower, but the surface roughness and taper angle are improved.

Moreover, we investigate the new values in different C_4F_8/ SF_6 gas ratios of 55/5, 50/10, 40/20, 30/30, 20/40, 10/50 and 5/55, and further investigate the values between 40/20 and 50/10 to examine the shape for 42/18, 44/16, 46/14, and 48/12 gas ratio. The decrease of SF_6 will reduce the undercut and the etching rate but the shape is improved. We especially investigate the cone shape related to the gas ratio of C_4F_8/ SF_6 to be 50/10 sccm for both regular and elongated pillars and find that this is the optimum ratio for the cone shape pillars production.

Project 5: Our process fabricates ultra-high aspect ratio pillars and consists of three major steps: (1) electron beam lithography (EBL) which includes transferring the pattern into double photo resistance ZEP 520A and PMMA by the lift-off technique to create the Cr mask, then (2) inductively coupled plasma (ICP) RIE to etch the silicon with the protected area of Cr as a mask and finally (3) sharpening the resulting pillars using wet etch employing HNO_3 and HF with ratio 200:1. The target arrayed pillars length is 10 micrometers and diameter ~100 nm, leading to an aspect ratio of order 100. After dry etching, the nanopillars array with the desired height is accomplished then the thinning to the desired diameter using wet etching. The measured tip diameter of sharpened nanopillars is 73.71nm and pillar height is 10μm. Consequently, this method can successfully achieve the fabrication of ultra-high aspect ratio of silicon nanopillars array with an aspect ratio of 135.

Project 6: This research fabricates HAR tips using a FIB. We demonstrate a direct fabrication method involving FIB and RIE to convert a regular pyramidal shaped probe into a HAR probe. That occurs

systematically by reducing FIB milling volume from 0.5 μm^3 to around 0.01 μm^3 and replacing it with RIE in batch style. The result is a semi batch style of HAR tips, using a little time of FIB for individual tips, then the tip batches are processed through two steps of RIE, where the HAR batch is accomplished. The tips have been tested by AFM and show a very good scanning result. Further successful work has been performed to automate the process using a programmable FIB.

Project 7: We demonstrate the use of FIB patterns in both Ga and Au implanted as an etch mask. FIB mask writing is using the lithographic process for patterning of silicon by fluorinated plasma etching. This work is limited to nanoscale patterning of silicon, but it can be extended into an etch mask using other ions and materials followed by other etching chemistries. We demonstrate the use of Ga FIB and find that 8125 $\mu C/cm^2$ dose is the optimum dose for Si as ion implantation for 200 nm implant mask diameter and get nanopillar of 653 nm height with the base of 317 nm. Also, the 3219 $\mu C/cm^2$ is the optimum dose for Au FIB implantation. This implantation is done in 200nm diameter and the result is nanopillars with 880nm high and 338nm base. This technique can be applied to a regular commercial tip to transform it into a HAR tip.

In conclusion, AFM probes is a very promising field of research where more development is still needed. The market share in the mid $1000's of million and have a double-digit growing rate. The starting point on this work was modifying a regular commercial tip to high-performance probes, where we explore all the possible techniques from deposition/etching to FIB (milling and implantation) including the tip oxidation sharpening. Then we switch to the tip fabrication from silicon wafer directly, where we study the RIE recipe of Si etch and all the effect from different parameters, then the wet etch and how to employ it in the production of HAR pillar. This pillar becomes the foundation to build up the HAR apex.

References

[1] B. Abhijit, S. B. Ilker, Alexandru, T. Wang, D. Enkeleda, F Franz, "Advances in top-down and bottom-up surface nanofabrication: Techniques, applications & future prospects". Advances in Colloid and Interface Science. 170: 2-27, (2012).
[2] C. Minelli, "BOTTOM-UP APPROACHES FOR ORGANIZING NANOPARTICLES WITH POLYMERS", Ph.D. thesis, FACULTÉ SCIENCES, Università Degli Studi di Firenze, Italie (2004).
[3] W. Lu; C. ML, "Nanoelectronics from the bottom up". Nature Materials. 6, 841 - 850 (2007).
[4] R. Dey, "Nanofabrication and its application in atomic force microscopy (AFM)", thesis Doctor of Philosophy, Electrical and Computer Engineering (Nanotechnology), University of Waterloo, Canada, (2015)
[5] S. Y. Chou, P. R. Krauss, and P. J. Renstrom, "Imprint Lithography with 25-Nanometer Resolution", Science 272 (5258), 85–7 (1996).
[6] L. Novotny, B. Hecht, "Principles of nano-optics", first ed., Cambridge University, Press: Cambridge, England, (2006).
[7] NanoTechWire.com Press Release: "ALIS Corporation Announces Breakthrough in Helium Ion Technology for Next-Generation Atomic-Level Microscope", (2005).
[8] W. H. Escovitz, T. R. Fox and R. Levi-Setti, "Scanning Transmission Ion Microscope with a Field Ion Source", Proceedings of the National Academy of Sciences of the United States of America 72 (5), 1826 (1975).
[9] K. Lee, J Lim, C. Mirkin, "Protein Nanostructures Formed via Direct-Write Dip-Pen Nanolithography". Journal of American Chemistry Society. 125:5588 (2003).
[10] M. Mohammad, M Mustafa, S. Dew, M. Stepanova, "The Interdependence of Exposure and Development Conditions when Optimizing Low-Energy EBL for Nano-Scale Resolution, Nanofabrication Techniques and Principles", Springer M. Stepanova and S. Dew (Eds.) 350 (2012).
[11] Drexler, K. Eric, " Engines of Creation: The Coming Era of Nanotechnology". Doubleday. ISBN 0-385-19973-2 (1986).
[12] Drexler, K. Eric, "Nanosystems: Molecular Machinery, Manufacturing, and Computation", New York: John Wiley & Sons. ISBN 0-471-57547-X, (1992).
[13] "Nanoscience and nanotechnologies: opportunities and uncertainties". Royal Society and Royal Academy of Engineering. July 2004, (2011).
[14] Allhoff, Fritz, Lin, Patrick, Moore, Daniel, "What is nanotechnology and why does it matter?: from science to ethics", John Wiley and Sons, ISBN 1-4051-7545-1, (2010).
[15] M. Kafshgari, N. Voelcker, F. Harding, "Applications of zero-valent silicon nanostructures in biomedicine". Nanomedicine (Lond). 10 (16): 2553–71, PMID 26295171, (2015).
[16] M. Kurtoglu, T. Longenbach, P. Reddington, Y. Gogotsi, "Effect of Calcination Temperature and Environment on Photocatalytic and Mechanical Properties of Ultrathin Sol-Gel Titanium Dioxide Films". Journal of the American Ceramic Society. 94 (4): 1101–1108, (2011).
[17] B. Mayer, L. Janker, B. Loitsch, J. Treu, T. Kostenbader, S. Lichtmannecker, T. Reichert, S. Morkötter, M. Kaniber, G. Abstreiter, C. Gies, G. Koblmüller, J Finley, (2015).
[18] H.S. Carlslaw, J.C. Jaeger, "Conduction of Heat in Solids", Oxford University Press, Oxford, UK, ed. 2, (1959).
[19] A. Gaharwar, N. Peppas, A. Khademhosseini, "Nanocomposite hydrogels for biomedical applications". Biotechnology and Bioengineering, 111 (3): 441–53, (2014).
[20] S. Mashaghi, T. Jadidi, G. Koenderink, A. Mashaghi, "Lipid Nanotechnology". Int. J. Mol. Sci. 2013 (14): 4242–4282, (2013).
[21] R. Jaeger, "Film Deposition". Introduction to Microelectronic Fabrication (2nd ed.). Upper Saddle River: Prentice-Hall. ISBN 0-201-44494-1, (2002).
[22] R. D. Mathis Company Evaporation Sources Catalog, by R. D. Mathis Company, (1992).
[23] S.M. Sze, "Semiconductor Devices: Physics and Technology", ISBN 0-471-33372-7, (2001).
[24] K. Harsha, "Principles of Physical Vapor Deposition of Thin Films", Elsevier, Great Britain (2006).
[25] S. Mackie and S. P. Beaumont, "Materials and Processes for Nanometer Lithography", Solid State Technology, 117 (1995).
[26] R. Bunshah, "Deposition Technologies for Films and Coatings", New York: Noyes Publication, (2001).
[27] "Vacuum Thermal Evaporation", exposed by Hivatec Laboratory, http://hivatec.ca/consulting-design/thin-film-deposition/.

[28] M. Madou, "Fundamentals of Microfabrication: The science of Miniaturization" 2nd Ed., CRC Press (2002).
[29] J. George, "Preparation of thin films", Marcel Dekker, Inc., New York (1992).
[30] S. Kesapragada, "Nanospring pressure sensors grown by glancing angle deposition". Nano Letters 6.4, 854–857 (2006).
[31] S. A. Chambell, "The Science and Engineering of microelectronic Fabrication", Oxford University Press, (2001).
[32] B. Cui, University of Waterloo, ECE Department course, retrieved from https://ece.uwaterloo.ca/~bcui/ECE_730.html.
[33] S. Wolf, R. Tauber, "Silicon Processing for the VLSI Era: Volume 1- Process Technology". Lattice Press. ISBN 0-9616721-3-7. 531-534 (1986).
[34] J. Driskell, "The use of aligned silver nanorod arrays prepared by oblique angle deposition as surface enhanced Raman scattering substrates". The Journal of Physical Chemistry C 112.4, 895–901 (2008).
[35] K. Robbie, M. J. Brett. "Sculptured thin films and glancing angle deposition: Growth mechanics and applications". Journal of Vacuum Science & Technology A: Vacuum, Surfaces, and Films 15.3, 1460–1465 (1997).
[36] D. Wolfe, "Synthesis and characterization of TiC, TiBCN, TiB2 /TiC and TiC/CrC multilayer coatings by reactive and ion beam assisted, electron beam-physical vapor deposition (EB-PVD)", thesis PHD, The Pennsylvania State University, (1996).
[37] T. W. Johnson, Z. J. Lapin, R. Beams, N. C. Lindquist, S. G. Rodrigo, L. Novotny, S. H. Oh, "Highly Reproducible Near-Field Optical Imaging with Sub-20-nm Resolution Based on Template-Stripped Gold Pyramids", ACS Nano 6, 9168–9174 (2012).
[38] B. Cui, University of Waterloo, ECE Department course, retrieved from https://ece.uwaterloo.ca/~bcui/ECE_730.html.
[39] T. Suntola, "Thirty Years of ALD", An Invited Talk at AVS Topical Conference on Atomic Layer Deposition (ALD2004); University of Helsinki: Helsinki, Finland, (2004).
[40] V. B. Aleskovskii, Z. Khim, J. Appl. Chem 47, 2145, USSR, (1974).
[41] M. Ritala, M. Leskela, J. Dekker, C. Mutsaers, P. Soininen, J. Skarp, J. Chem. Vap. Deposition 5, 7, (1999).
[42] S. George, A. Ott, J. Klaus, J. Phys. Chem., 100, 13121, (1996).
[43] S. George, A. Ott, J. Klaus, J. Phys. Chem., 100, 13121, (1996).
[44] X. Mu, "Liquid Etching Mask in Wet Chemical Etching to Generate Glass Microstructures with an Improved Aspect Ratio", Lab on a Chip, 2009, 9: (1994-1996).
[45] M. Shikida, K. Sato, K. Tokoro, D Uchikawa, "Surface morphology of anisotropically etched single-crystal silicon". Journal of Micromechanical Microengineering. 10: 522, (2000).
[46] R. Finne, D. Klein, "A Water-Amine-Complexing Agent System for Etching Silicon". Journal of the Electrochemical Society. 114: 965–70, (1967).
[47] P. Walker, H. William CRC Handbook of Metal Etchants, ISBN 0-8493-3623-6, (1991).
[48] S. Wolf, "Silicon Processing for the VLSI Era: Volume 2", Process Technology. Lattice Press. ISBN 0-9616721-5-3, (1990).
[49] S. Wolf, S, R.N. Tauber, "Silicon Processing for the VLSI Era: Volume 3" Process Technology. Lattice Press. ISBN 0-9616721-4-5, (1995).
[50] B. Bahadur, "Liquid Crystals: Applications and Uses vol.1", World Scientific. p. 183. ISBN 981-02-2975-5, (1990).
[51] M. Kohler, "Etching in Microsystem Technology", John Wiley & Son Ltd. p. 329. ISBN 3-527-29561-5, (1999).
[52] "A graphical representation of the selectivity of wet etching", exposed by Wikipedia, https://en.wikipedia.org/wiki/Etching_(microfabrication).
[53] R. Richard, "Lithography". Introduction to Microelectronic Fabrication (2nd ed.). Upper Saddle River: Prentice Hall. ISBN 0-201-44494-1, (2002).
[54] E. SHKONDIN, O. TAKAYAMA, M. E. ARYAEE PANAH, P. LIU, P. V. LARSEN, M. D. MAR, F. JENSEN, A. V. LAVRINENKO, "Large-scale high aspect ratio Al-doped ZnO nanopillars arrays as anisotropic metamaterials", OPTICAL MATERIALS EXPRESS Vol. 7, No. 5, 1606, May (2017)
[55] C. Padeste, H. Ozcelik, J. Ziegler, A. Schleunitz, M. Bednarzik, D. Yucel, V. Hasırcı, "Replication of high aspect ratio pillar array structures in biocompatible polymers for tissue engineering applications", Microelectronic Engineering 88 (2011) 1836–1839
[56] N. Toan, S. Sangu, T. Ono, "Fabrication of High Aspect Ratio SiO2 and Tempax Glass Pillar Structures and Its Application for Optical Modulator Device", JOURNAL OF MICROELECTRO MECHANICAL SYSTEMS, VOL. 25, NO. 4, AUGUST 2016

[57] H. Robbins and B. Schwartz," Chemical Etching of Silicon I", Journal of the electrochemical society, 106, 505 (1959).
[58] H. Robbins and B. Schwartz, "Chemical Etching of Silicon II", Journal of the electrochemical society, 107, 108 (1960).
[59] B. Schwartz and H. Robbins, "Chemical Etching of Silicon III", Journal of the electrochemical society, 108, 365 (1961).
[60] B. Schwartz, H. Robbins, "Chemical Etching of Silicon IV", Journal of the electrochemical society, 123, no 12 (1976)
[61] S. H. Kim, S. H. Lee, H. T. Lim, S. K. Lee, Y. K. Kim, "Anisotropic bulk etching of <100> silicon with high aspect ratio", Technical Digest of the 15th Sensor Symposium Kanagawa, Japan, 3-4 June 1997, pp193-196, The Institute of Electrical Engineers of Japan (IEEJ), Tokyo, Japan.
[62] M. Sugawara, "Plasma etching: fundamentals and applications", New York: Oxford University Press Inc, (1998).
[63] M. D. Henry, "ICP ETCHING OF SILICON FOR MICRO AND NANOSCALE DEVICES", PHD Thesis, CALIFORNIA INSTITUTE OF TECHNOLOGY, Pasadena, California (2010).
[64] C. Cardinaud, M. Peignon, P. Tessier, "Plasma etching: principles, mechanisms, application to micro- and nano-technologies". Applied Surface Science. Surface Science in Micro & Nanotechnology. 164 (1–4): 72–83, (2000).
[65] J. Coburn, H. Winters, "Ion- and electron-assisted gas-surface chemistry—An important effect in plasma etching". Journal of Applied Physics. 50 (5), 3189–3196, (1979).
[66] D. Mattox, "Handbook of Physical Vapor Deposition (PVD) Processing", Westwood, New Jersey: Noyes Publication, (1998).
[67] K. Bean, "Anisotropic etching of silicon". IEEE Transactions on Electron Devices. ED-25, 1185 (1978).
[68] "Basic Mechanism of a DC Plasma discharge"- exposed in the slide of "Application of thin films in contemporary industry", http://www.slideshare.net/laboratoridalbasso/obst-salento-1st.
[69] T. Suntola, "Thirty Years of ALD", An Invited Talk at AVS Topical Conference on Atomic Layer Deposition (ALD2004); University of Helsinki: Helsinki, Finland, (2004).
[70] Atomic Layer Deposition: An Overview, Steven M. George*, Chem. Rev., 110, 111–131, (2010).
[71] A. Wasy, G. Balakrishnan, S. Lee, J. Kim, D. Kim, T. Kim, J. Song, "Argon plasma treatment on metal substrates and effects on diamond-like carbon (DLC) coating properties". Crystal Research and Technology. 49: 55, (2014).
[72] J. Coburn, H. Winters, Harold, "Plasma etching—A discussion of mechanisms". Journal of Vacuum Science & Technology. 16 (2): 391–403, (1979).
[73] K. Suzuki, S. Okudaira, N. Sakudo, I. Kanomata, "Microwave Plasma Etching". Japanese Journal of Applied Physics. 16: 1979–1984, (1977).
[74] R. Chang, C. Chang, S. Darac, "Hydrogen plasma etching of semiconductors and their oxides". Journal of Vacuum Science & Technology. 20 (1): 45–50, (1982).
[75] A. Zia, Y. Wang, S. Lee, S, "Effect of Physical and Chemical Plasma Etching on Surface Wettability of Carbon Fiber-Reinforced Polymer Composites for Bone Plate Applications". Advances in Polymer Technology. 34, (2015).
[76] K. Nojiri, "Dry Etching Technology for Semiconductors". Springer International. ISBN 978-3-319-10295-5, (2015).
[77] https://www.oxford-instruments.com/products/etching-deposition-and-growth/plasma-etch-deposition/rie.
[78] Handbook of Silicon Based MEMS Materials and Technologies. DOI: http://dx.doi.org/10.1016/B978 0-323-29965-7.00022-1
[79] C. Chang, Y.-F. Wang, Y. Kanamori, J.-J. Shih, Y. Kawai, C.-K. Lee, et al., "Etching submicrometer trenches by using the Bosch process and its application to the fabrication of antireflection structures," Journal of micromechanics and microengineering, vol. 15, p. 580, 2005.
[80] J. Yeom, Yan Wu', M. A. Shannon, "CRITICAL ASPECT RATIO DEPENDENCE IN DEEP REACTIVE ION ETCHING OF SILICON", The 12th International Conference of Solid Stale Sensors, Actuators and Microsystems. Boston, June 8-12. 2003
[81] Y. Zargouni, S. Deheryan, A. Radisic, D. J. Cott, S. Rochan, K. Alouani, C. Huyghebaert, P. M. Vereecken, "Electrodeposition and Characterization of Manganese Dioxide Thin Films on Silicon Pillar Arrays for 3D Thin-Film Lithium-Ion Batteries", ECS Transactions, 61 (9) 29-41 (2014)
[82] L . V. Asquez-Garc, A. Akinwande, "Fabrication of large arrays of high-aspect-ratio single-crystal silicon columns with isolated vertically aligned multi-walled carbon nanotube tips", Nanotechnology 19 (2008) 405305
[83] J. Aebersold, K. Walsh, M. Beggans, "Utilization of Direct Write Lithography to Develop Ultra High Aspect Ratio (>100:1) DRIE Silicon Pillars", IEEE Xplore Conference, West Lafayette, IN, USA 15 July 2010
[84] R Dussart, T Tillocher, P Lefaucheux and M Boufnichel, "Plasma cryogenic etching of silicon: from the early days to today's advanced technologies", J. Phys. D: Appl. Phys. 47 - 123001 (2014)

[85] B. Wu, A. Kumar, and S. Pamarthy, “High aspect ratio silicon etch: A review”, JOURNAL OF APPLIED PHYSICS 108, 051101 (2010)
[86] P. Doll, A. Ahmad, A. Bacher, A. Muslija, R. Thelen, L. Hahn, R. Ahrens, B. Spindler, A. Guber, “Fabrication of silicon nanopillar arrays by electron beam lithography and reactive ion etching for advanced bacterial adhesion studies”, Mater. Res. Express 6 (2019) 065402
[87] A. Méndez-Vilas, J. Díaz, “Microscopy: Science, Technology, Applications and Education”, 2190, FORMATEX (2010)
[88] B. Hafner, “Scanning Electron Microscopy Primer”, Characterization Facility, University of Minnesota—Twin Cities (2007).
[89] E.W. Mueller, T.T. Tsong, “Field Ion Microscopy Principles and Applications”, American Elsevier, New York, (1969).
[90] A. Benninghoven, F.G. Rüdenauer, H.W. Werner, “Secondary Ion Mass Spectrometry: Basic Concepts, Instrumental Aspects, Applications and Trends” John Wiley, New York, (1987).
[91] M. Nastasi, J.W. Mayer, J.K. Hirvonen, “Ion-Solid Interactions: Fundamentals and Applications”, Cambridge University Press, Cambridge, UK, (1996).
[92] A. A. Tseng, "Recent developments in micromilling using focused ion beam technology", J. Micromech. Microeng. 14(4), R15 (2004).
[93] V. Sivel, J. Van den Brand, W. Wang, “Mohdadi H, Tichelaar FD, Alkemade PFA, Zandbergen HW. Application of the dual-beam FIB/SEM to metals research”, J. Mircrosc.-Oxford, 214:237, (2004).
[94] J. Orloff, M. Utlaut, L. Swanson, “High Resolution Focused Ion Beams: FIB and its Applications”, Kluwer Academic, Dordrecht, (2002).
[95] M. Phaneuf, L. Li, “FIB Techniques for Analysis of Metallurgical Specimens”, Microsc. Microanal, 6S2:524, (2000).
[96] A. Latif, “NANOFABRICATION USING FOCUSED ION BEAM, PHD thesis, Darwin College, University of Cambridge, (2000).
[97] J. Taniguchi, N. Ohno, S. Takeda, I Miyamoto, M. Komuro, “Focused-ion-beam-assisted etching of diamond in XeF2”, J. Vac., Sci. Technol. B., 16:2506, (1998).
[98] D. Mavrocordatos, M. Steiner, M. Boller, “Analytical electron microscopy and focused ion beam: complementary tool for the imaging of copper sorption onto iron oxide aggregates”, J. Microsc.-Oxford, 210:45, (2003).
[99] L.A Giannuzzi, F.A. Stevie, “Introduction to Focused Ion Beams: Instrumentation, Theory, Techniques, and Practice”, Springer, New York, (2005).
[100] L. Mechin, J. Villegier, and D. Bloyet, “Chapter 1 Introduction Nanofabrication using FIB”, Appl. Phys. Lett. 70, 123 (1997).
[101] Driesel W, Dietzsch C, Muhle R, J. Vac. Sci. Technol. B, 14, 3367(1996)
[102] A. Latif "NANOFABRICATION USING FOCUSED ION BEAM", Darwin College, Cambridge, Ph.D. thesis, University of Cambridge, (2000).
[103] B. Cui, University of Waterloo, ECE Department course, retrieved from https://ece.uwaterloo.ca/~bcui/ECE_730.html.
[104] F. S. Jamaludin, M. F. Mohd Sabri, S. M. Said, “Review: Controlling parameters of focused ion beam (FIB) on high aspect ratio micro holes milling”, Microsyst Technol 19:1873–1888 (2013)
[105] A. Tseng, A. Notargiacomo, T. Chen, "Nanofabrication by scanning probe microscope lithography: A review", J. Vac. Sci. Technol. B. 23, 877 (2005).
[106] G. Binnig, H. Rohrer, "Scanning tunneling microscopy". IBM Journal of Research and Development. 30 (4) 355–69, (1986).
[107] "Press Release: the 1996 Nobel Prize in Physics". Nobelprize.org. 15 October (1986).
[108] H. Lyeo, A. Khajetoorians, L. Shi, K. Pipe, R. Ram, A Shakouri, C. Shih, “Profiling the Thermoelectric Power of Semiconductor Junctions with Nanometer” Resolution Science 303 816-8 (2004).
[109] H. Bhaskaran, A Sebastian, U Drechsler, M Despont, “Encapsulated tips for reliable nanoscale conduction in scanning probe technologies”, Nanotechnology 20 105701 (2009).
[110] J. Stroscio, D. Eigler, “Atomic and Molecular Manipulation with the Scanning Tunneling Microscope” Science 254 1319-26 (1991).
[111] G. Binnig, Quate, C. Gerber, “Atomic force microscope” Physical review letters 56 930-3 (1986).
[112] A. Schneider, R. H. Ibbotson, R. J. Dunn, E. Huq, “Arrays of SU-8 microcantilevers with integrated piezoresistive sensors for parallel AFM applications” Microelectronic Engineering 88 2390-3 (2011).
[113] D. Saya, Belaubre, F. Mathieu, D. Lagrange, J. B. Pourcel, C. Bergaud, "Sipiezoresistive microcantilevers for highly integrated parallel force detection applications", Sensors and Actuators A-Physical 123-24 23-9 (2005).

[114] K. Salaita, Y. Wang, J. Fragala, R. Vega, C. Liu, C. Mirkin, “Massively Parallel Dip–Pen Nanolithography with 55 000-Pen Two-Dimensional Arrays”, Angewandte Chemie International Edition 45 7220-3 (2006).
[115] B. Gotsmann, U. Duerig, J. Frommer, C. Hawker, “Exploiting chemical switching in a Diels-Alder polymer for nanoscale probe lithography and data storage”, Advanced functional materials 16 1499-505 (2006).
[116] J. Gimzewski, C. Gerber, E. Meyer, R. Schlittler, “Observation of a Chemical- Reaction Using a Micromechanical Sensor”, Chemical Physics Letters 217 589-94 (1994).
[117] W. King, B Bhatia, J. Felts, H. Kim, B. Kwon, B. Lee, S. Somnath, M. Rosenberger, “Heated Atomic Force Microscope Cantilevers and their Applications” Annual Review of Heat Transfer 16 287-326 (2013).
[118] G. Binnig, M. Despont, U. Drechsler, W. Häberle, M Lutwyche, P. Vettiger, H. Mamin, B. Chui, T. Kenny, “Ultrahigh-density atomic force microscopy data storage with erase capability” Applied Physics Letters 74 1329 (1999).
[119] D. Price, M Reading, A. Hammiche, H. Pollock, “Micro-thermal analysis: scanning thermal microscopy and localised thermal analysis”, International Journal of Pharmaceutics 192 85-96 (1999).
[120] D. Pires, J. Hedrick, A. De Silva, J. Frommer, B. Gotsmann, H. Wolf, M. Despont, U Duerig, A. Knoll, “Nanoscale Three-Dimensional Patterning of Molecular Resists by Scanning Probes”, Science 328 732 (2010).
[121] M. Igeta, K. Banerjee, G. Wu, C. Hu, A. Majumdar, “Thermal Characteristics of Submicron Vias Studied by Scanning Joule Expansion Microscopy”, IEEE Electron Device Letters, V 21, 5, (2000).
[122] B. Bhushan, O. Marti, “Scanning Probe Microscopy – Principle of Operation, Instrumentation, and Probes, Chapter 2”, Springer, ISBN: 978-3-642-15282-5 (2011).
[123] P. Schön, K. Bagdi, K. Molnár, P. Markus, B. Pukánszky, G. Vancso, P. Schön, “Quantitative mapping of elastic moduli at the nanoscale in phase separated polyurethanes by AFM”, European Polymer Journal 47, 692–698 (2011).
[124] D. W. Pohl, W. Denk and M. Lanz, "Optical stethoscopy: Image recording with resolution lemda/20", Appl Phys. Lett. 44, 651-653 (1984).
[125] D. Wang, L. Tsau and K. L. Wang, "Nanometer-structure writing on Si (100) surfaces using a non-contact mode atomic force microscope", Appl. Phys. Lett. 65, 1415-1417 (1994).
[126] Z. J. Davis, G. Abadal, O. Hansen, X. Borise, N. Barniol, F. Perez-Murano and A. Boisen, "AFM lithography of aluminium for fabrication of nanomechanical systems", Ultramicroscopy 97, 467-472 (2003).
[127] F. Leite, P. Herrmann, “Application of atomic force spectroscopy (AFS) to studies of adhesion phenomena: a review”, J. Adhesion Sci. Technol., V 19, 3–5, 365–405 (2005).
[128] T. R. Albrecht, S. Akamine, T. E. Carver, C. F. Quate, "Microfabrication of cantilever styli for the atomic force microscope", J Vac Sci Technol A. 8, 3386–3396 (1990).
[129] A. Miletic, “Introduction to Scanning Probe Microscope”, University of Novi Sad, Faculty of Technical Science (2010).
[130] E. Meyer, Atomic Force Microscopy”, Progress in Surface Science, Vol. 41, pp. 3-49 (1992).
[131] R. Wilson, H. Bullen, “Introduction to Scanning Probe Microscopy (SPM)”, Department of Chemistry, Northern Kentucky University, Highland Heights, KY 41099., Development Workshop held at the University of California - Riverside, July 10-14 (2006).
[132] P. Neuzil, R. J. Nagarajan, "The formation of sharp AFM tips by single step etching", Micromech Microeng. 16, 1298–1300 (2006).
[133] E. Duriau, T. Clarysse, T. Hantschel, W. Vandervorst, "Fabrication of cantilevers and double AFM tips for the NanoProfiler", Microelectronic Engineering 84, 1162–1167 (2007).
[134] G. Meyer, N Amera, “Novel optical approach to atomic force microscopy”, Phys, Lett. 53, 12, 19 September (1988).
[135] A. Weisenhorn, P. Hansma, T. Albrecht, C. Quate, “Forces in atomic force microscopy in air and water”, Appl. Phys. Lett. 54 (26), 26 (1989).
[136] F. J. Giessibl and B. M. Trafas, “Piezoresistive cantilevers utilized for scanning tunneling and scanning force microscope in ultrahigh vacuum”, Rev. Sci. Instrum. 65 (6), June (1994).
[137] Y. Jeong, G. Jayanth, S. Jhiang, C. Menq, “Design and Fabrication of an Active Multiaxis Probing System for High Speed Atomic Force Microscopy”, IEEE TRANSACTIONS ON NANOTECHNOLOGY, V 9, 3, (2010).
[138] S. Salapaka, A. Ramamoorthy, M. Salapaka, “AFM Imaging”, IEEE CONTROL SYSTEMS MAGAZINE1066-033X/13, DECEMBER (2013).
[139] A. Bard, F. Fan, J. Kwak, O. Lav, "Scanning Electrochemical Microscopy. Introduction and Principles", Anal. Chem. 61(2), 132-138 (1989).
[140] R. Meservy, “The Use of Atomic Force Microscopy in Biological Imaging”, Utah State University, Physics (2006).

[141] R. Reifenberger, “Introduction to Scanning, Probe Microscopy, Fundamentals of Atomic Force Microscopy, Part I Foundations, Chapter 1”, Published by World Scientific Publishing ISBN 10: 9814630357 or ISBN 13: 9789814630351 (2015).
[142] I. Dobryden,"Scanning Probe Microscopy Studies of Interaction Forces Between Particles", Department of Engineering Sciences and Mathematics, Lule˚a University of Technology, Sweden Doctor Thesis (2015).
[143] B. Bhushan, H. Fuchs, M. Tomitori, “Applied Scanning Probe Methods VIII, Scanning Probe Microscopy Techniques”, Springer, ISBN 978-3-540-74079-7 (2008).
[144] B. Bhushan (ed.), “Nanotribology and Nanomechanics”, Springer, ISBN 978-3-642-15283-2, (2011).
[145] P. Russell, "AFM TIP NanoWorld Webinar" www.nanoworld.com, Appalachian State Univ., 10 November (2008).
[146] AppNano, www.appnano.com.
[147] Optimized Positioning Upon Sample, www.opustips.com.
[148] NT-MDT Co., www.ntmdt.com, www.ntmdt-tips.com.
[149] MikroMasch, www.mikromasch.com.
[150] Budget Sensors, www.budgetsensors.com.
[151] R. Dey, “Nanofabrication and its application in atomic force microscopy (AFM)”, thesis Doctor of Philosophy, Electrical and Computer Engineering (Nanotechnology), University of Waterloo, Canada, (2015).
[152] T. S. Ravi, R. B. Marcus, and D. Liu, "Oxidation sharpening of silicon tips", J. Vac. Sci. Technol. B 9(6), 2733 (1991).
[153] S. Akamine, R.C. Barrett, C.F. Quate, Improved atomic force microscope images using microcantilevers with sharp tips. Appl. Phys. Lett. 57(3), 316–318 (1990).
[154] A. Folch, M. S. Wrighton, and M. A. Schmidt, "Microfabrication of Oxidation- Sharpened Silicon Tips on Silicon Nitride Cantilevers for Atomic Force Microscopy", Journal of Micro electro-mechanical systems 6(4), 303–306 (1997).
[155] P. Russell, "AFM TIP NanoWorld Webinar", www.nanosensors.com, Appalachian State Univ., 10 November (2008).
[156] H. Takahashi, Y. Mimura, S. Mori, M. Ishimori, A. Onoe, T. Ono, M. Esashi, "The fabrication of metallic tips with a silicon cantilever for probe-based ferroelectric data storage and their durability experiments", Nanotechnology 20, 365201 (2009).
[157] L. Li, X. Han, W. G. Wu, F. Ding, Q. H. Chen, "Fabrication of novel cantilever with nanotip for AFM applications", Solid State Integr. Circuit Technol. ICSICT 20–23, 2383–2386 (2008).
[158] D. P. Burt, P. S. Dobson, L. Donaldson, J. M. R. Weaver, "A simple method for high yield fabrication of sharp silicon tips", Microelectron Eng. 85, 625–630 (2008).
[159] "AFM TIP NanoWorld Webinar", P. Russell Appalachian State Univ., 10 November (2008).
[160] C. Martin-Olmos, H. I. Rasool, B. H. Weiller, and J. K. Gimzewski, "Graphene MEMS: AFM probe performance improvement", ACS Nano 7(5), 4164–70 (2013).
[161] K. Akiyama, T. Eguchi, T. An, Y. Fujikawa, Y. Yamada-Takamura, T. Sakurai, and Y. Hagegawa, "Development of a metal tip cantilever for non-contact atomic force microscopy", Rev. Sci. Instrum. 76, 033705 (2005).
[162] M. J. Vasile, D. Grigg, J. E. Griffith, E. Fitzgerald, and P. E. Russell, "Scanning Probe Tip Geometry Optimized for Metrology by FIB Ion Milling", J. Vac. Sci. Technol. B 9, 3569 (1991).
[163] C. V. Nguyen, Q. Ye and M Meyyappan, "Carbon nanotube tips for scanning probe microscopy: fabrication and high aspect ratio nanometrology", Measurement Science and Technology 16, 2138 (2005).
[164] N. R. Wilson and J. V. Macpherson, "Carbon nanotube tips for atomic force microscopy", Nature Nanotechnology 4, 483 (2009).
[165] S. Kuwahara, S. Akita, M. Shirakihara, T. Sugai, Y. Nakayama, H. Shinohara, "Fabrication and characterization of high-resolution AFM tips with high-quality double-wall carbon nanotubes", Chemical Physics Letters 429, 581–585 (2006).
[166] T. Larsen, K. Moloni, F. Flack, M. A. Eriksson, M. G. Lagally, C. T. Black, "Comparison of wear characteristics of etched-silicon and carbon nanotube atomic force microscopy probes", Appl. Phys. Lett. 50, 1996 (2002).
[167] B. Bhushan, “Nanotribology and Nanomechanics, An Introduction”, 2nd edition, Springer-Verlag Berlin Heidelberg, ISBN 978-3-540-77607-9, (2008).
[168] T.R. Albrecht, S. Akamine, T.E. Carver, C.F. Quate, Microfabrication of cantilever style for the atomic force microscope. J. Vac. Sci. Technol. An 8(4), 3386–3396 (1990).
[169] H. Takahashi, Y. Mimura, S. Mori, M. Ishimori, A. Onoe, T. Ono, M. Esashi, "The fabrication of metallic tips with a silicon cantilever for probe-based ferroelectric data storage and their durability experiments", Nanotechnology 20, 365201 (2009).

[170] O. Wolter, T. Bayer, J. Greschner, Micromachined silicon sensors for scanning force microscopy. J. Vac. Sci. Technol. B 9(2), 1353–1357 (1991).
[171] G. Villanueva, J. A. Plaza, A. Sánchez, K. Zinoviev, F. Pérez-Murano, and J. Bausells, "DRIE based novel technique for AFM probes fabrication",Microelectronic Engineering 84(5–8), 1132– 1135 (2007).
[172] C. Cheung, J. Hafner, T. Odom, K. Kim, C. Lieber, Appl. Phys. Lett. 76, 3136-3138, (2000).
[173] J. Griffith, H. Marchman, G. Miller, L. Hopkins, J. Vac. Sci. Technol. B, 13, 1100-1105, (1995).
[174] Woolley, A. T.; Cheung, C. L.; Hafner, J. H.; Lieber, C. M. Chem. Biol, 7, R193-204, (2000).
[175] C. Cheung, J. Hafner, C. Lieber, Proc. Natl. Acad. Sci. U.S.A., 97, 3809-3813, (2000).
[176] C. Martin-Olmos, H. I. Rasool, B. H. Weiller, and J. K. Gimzewski, "Graphene MEMS: AFM probe performance improvement", ACS Nano 7(5), 4164–70 (2013).
[177] Y. Fu, W. Zhou, and L. Lim, "Geometrical characterization issues of plasmonic nanostructures with depth-tuned grooves for beam shaping", Optical Engineering 45(10), 108001 (2006).
[178] L. Cockins, Y. Miyahara, R. Stomp, and P. Grutter, "High-aspect ratio metal tips attached to atomic force microscopy cantilevers with controlled angle, length, and radius for electrostatic force microscopy", Review Of Scientific Instruments 78, 113706 (2007).
[179] J. K. David., and C. Chou, "Imaging steep, high structures by scanning force microscopy with electron beam deposited tips", Surface Science 268, 333-339 (1992).
[180] D. J. Comstock, J. W. Elam, M. J. Pellin, and M. C. Hersam, "High aspect ratio nanoneedle probes with an integrated electrode at the tip apex", Review of scientific instruments 83, 113704 (2012).
[181] R. Jalilian, J. Rivera, D. Askari, S. Arva, J. M. Rathfon, R. W. Cohn, and M. M. Yazdanpanah, "Toward wafer-scale patterning of freestanding intermetallic nanowires", Nanotechnology 22, 295601 (2011).
[182] J. Brown, P. Kocher, C. S. Ramanujan, D. N. Sharp, K. Torimitsu, J. F. Ryan, "Electrically conducting, ultra-sharp, high aspect-ratio probes for AFM fabricated by electron-beam-induced deposition of platinum", Ultramicroscopy 133, 62–66 (2013).
[183] K. Akiyama, T. Eguchi, T. An, Y. Fujikawa, Y. Yamada-Takamura, T. Sakurai, and Y. Hagegawa, "Development of a metal tip cantilever for non-contact atomic force microscopy", Rev. Sci. Instrum. 76, 033705 (2005).
[184] J. Han, X. Li, H. Bao, G. Zuo, Y. Wang, F. Feng, Z. Yu, and X. Ge, "AFM probes fabricated with masked–maskless combined anisotropic etching and p+ surface doping", Journal of Micromechanics and Microengineering, 16(2), 198–204 (2006).
[185] B. Tang, K. Sato, H. Tanaka, and M. A. Gosalvez, "Fabrication of sharp tips with high aspect ratio by surfactant-modified wet etching for the AFM probe", micro-electro-mechanical systems (mems), IEEE 24th international conference, 328 - 331 (2011).
[186] S. Kuwahara, S. Akita, M. Shirakihara, T. Sugai, Y. Nakayama, H. Shinohara, "Fabrication and characterization of high-resolution AFM tips with high-quality double-wall carbon nanotubes", Chemical Physics Letters 429, 581–585 (2006).
[187] T. Larsen, K. Moloni, F. Flack, M. A. Eriksson, M. G. Lagally, C. T. Black, "Comparison of wear characteristics of etched-silicon and carbon nanotube atomic force microscopy probes", Appl. Phys. Lett. 50, 1996 (2002).
[188] A. T. Woolley, C. L. Cheung, J. H. Hafner, and C. M. Lieber, "Structural biology with carbon nanotube AFM probes", Chem. Biol. 7, R193–R204 (2000).
[189] Q. Ye et al., "Large-scale fabrication of carbon nanotube probe tips for atomic force microscopy critical dimension imaging applications", Nano Lett. 4, 1301–1308 (2004).
[190] J. H. Hafner, C. L. Cheung, T. H. Oosterkamp, and C. M. Lieber, "High-yield assembly of individual single-walled carbon nanotube tips for scanning probe microscopies", J. Phys. Chem. B 105, 743–746 (2001).
[191] http://nauganeedles.com/.
[192] M. M. Yazdanpanah, S. A. Harfenist, A. Safir and R. W. Cohn, "Selective self-assembly at room temperature of individual freestanding Ag2Ga alloy nanoneedles", J. Appl. Phys. 98, 073510 (2005).
[193] R. Dey, “Nanofabrication and its application in atomic force microscopy (AFM)”, thesis Doctor of Philosophy, Electrical and Computer Engineering (Nanotechnology), University of Waterloo, Canada, (2015).
[194] http://www.nanoworld.com/, http://nanosensors.com, http://www.nauganeedles.com.
[195] http://www.appnano.com/home.
[196] https://www.budgetsensors.com/all_in_one_afm_probes.html.
[197] https://angel.co/nanodevice-solutions.

[198] S. Zheng, “Nanofabrication of direct positioning atomic force microscope (AFM) probes and a novel method to attain controllable lift-off”, thesis Master of Applied Science, Electrical and Computer Engineering (Nanotechnology), University of Waterloo, Canada, (2017).

[199] S. Zheng, C. Zhu, R. K. Dey, and B. Cui, “Batch fabrication of AFM probes with direct positioning capability”, J. Vac. Sci. Technol. B 35(6), Nov/Dec 2017

[200] C. Con C, J. Zhang, B Cui, “Nanofabrication of high aspect ratio structures using evaporated resist containing metal”, Nanotechnology, 25, 175301 (2014)

[201] R. Dey, “Nanofabrication and its application in atomic force microscopy (AFM)”, thesis Doctor of Philosophy, Electrical and Computer Engineering (Nanotechnology), University of Waterloo, Canada, (2015).

[202] M. Liu, J. Peng, "Two-dimensional modeling of the self-limiting oxidation in silicon and tungsten nanowires". Theoretical and Applied Mechanics Letters. 6 (5): 195–199, (2016).

[203] B. Cui, University of Waterloo, ECE Department course, retrieved from https://ece.uwaterloo.ca/~bcui/ECE_730.html.

[204] J. Appels, E. Kooi, M. M. Paffen, J. J. H. Schatorje, and W. H. C. G. Verkuylen, “Local oxidation of silicon and its application in semiconductor-device technology,” PHILIPS RESEARCH Reports, vol. 25, no. 2, pp. 118–132, (1970).

[205] A. Kuiper, M. Willemsen, J. M. G. Bax, and F. H. P. H. Habraken, "Oxidation behavior of LPCVD silicon oxynitride films," Applied Surface Science, vol. 33, no. 34, pp. 757–764, (1988).

[206] R. Jaeger, "Thermal Oxidation of Silicon". Introduction to Microelectronic Fabrication. Upper Saddle River: Prentice-Hall. ISBN 0-201-44494-1, (2001).

[207] G. Pennelli, M. Totaro, M. Piotto, "Selective Doping of Silicon Nanowires by Means of Electron Beam Stimulated Oxide Etching", Nano Lett. 12, 1096–1101 (2012).

[208] R. K. Dey, B. Cui, “Thermal Oxidation in muffle furnace”, Oxidation user manual, (2017).

[209] N. Cabrera, N.F. Mott: Rep. Prog. Phys. 12, 163 (1949).

[210] N.F. Mott, S. Rigo, F. Rochet, A.M. Stoneham: Philos. Mag. B 60, 189 (1989).

[211] N.F. Mott: Philos. Mag. B 55, 117 (1987).

[212] E.S. Snow, P.M. Campbell: Science 270, 1639 (1995)

[213] R.B. Marcus, T.S. Ravi, T. Gmitter, K. Chin, D.J. Liu, W. Orvis, D.R. Ciarlo, C.E. Hunt, J. Trujillo, Formation of silicon tips with < 1 nm radius. Appl. Phys. Lett. 56(3), 236–238 (1990).

[214] C.A. Quote: In Highlights in Condensed Matter Physics and Future Prospects, L. Esaki (Ed.) (Plenum Press, New York 1991).

[215] D. Goldfaber-Gordon, M.S. Montemerlo, J.C. Love, G.J. Opiteck, J.C. Ellenbogen: Proc. IEEE, 85, 521 (1997).

[216] S. Akamine, C. F. Quate, "low-temperature thermal oxidation sharpening of micro-cast tips”, J. Vac. Sci. Tech. B 10(5), Sep/Oct 1992

[217] N. Sakuma, T. Ono, T. Saka, “Reproducibly Sharpened Pyramidal Diamond Field Emitter Arrays”, Technical Digest of IVMC'97 Kyongju, Korea 1997

[218] H Im, S-H. Oh, “Oxidation Sharpening, Template Stripping, and Passivation of Ultra-Sharp Metallic Pyramids and Wedges”, www.small-journal.com, small 2014, 10, No. 4, 680–684

[219] H. Takemura, N. Furutake, M. Nishimura, S. Tsuda, M. Yoshiki, A. Okamoto, S. Miyano, "Fully large- M. Alves et al. replace the high-temperature thermal oxidation technique by a mask of amorphous

[220] A. P. Janssen and J. P. Jones, J. Phys. D: Appl. Phys. 4, 118 (1971).

[221] B. Tang, K. Sato, H. Tanaka, M. A. Gosalvez, “FABRICATION OF SHARP TIPS WITH HIGH ASPECT RATIO BY SURFACTANT-MODIFIED WET ETCHING FOR THE AFM PROBE”, MEMS 2011, Cancun, MEXICO, January 23-27, 2011

[222] M. Alves, L. Porto, P. de Faria, E. Braga, "Amorphous hydrogenated carbon films used as masks for silicon micro-tips fabrication in a reactive ion etching with SF6 plasma", Vacuum 72 (2004) 485–488

[223] M. R. Rakhshandehrooa, S. W. Pangb, "Sharpening Si field emitter tips by dry etching and low-temperature plasma oxidation", J. Vac. Sci. Technol. B 14(6), Nov/Dec 1996

[224] C-H. Choi, C-J. Kim, “Fabrication of a dense array of tall nanostructures over a large sample area control with sidewall profile and tip sharpness”, Nanotechnology 17, 5326–5333 (2006)

[225] J. Han, X. Li, H. Bao, Y. Wang, B. Liu, X. Ge, “High-yield Fabrication of AFM Probes with Simultaneous Formation of Both Nano-tips and Cantilever”, Shanghai Institute of Microsystem and Information Technology, Chinese Academy of Sciences Shanghai 200050, China (2005)

[226] D. Resnik, D. Vrtacnik, U. Aljancic, M. Mozek, S. Amon, “Different aspect ratio pyramidal tips obtained by wet etching of (100) and (111) silicon”, Microelectronics Journal 34 (2003) 591–593

[227] K. Sun, W. Zhang, B. Li, J. Y. Lee, Y-H. Xie, J. Katzer, X. Wei, T. P. Russell, "Field Emission Tip Array Fabrication Utilizing Geometrical Hindrance in the Oxidation of Si", IEEE TRANSACTIONS ON NANOTECHNOLOGY, VOL. 11, NO. 5, SEPTEMBER 2012

[228] G. Georgiev, M. Muller-Wiegand, A. Georgieva, K. Ludolph, E. Oesterschulzea), "Lithography-free fabrication of sub-100 nm structures by self-aligned plasma etching of silicon dioxide layers and silicon", J. Vac. Sci. Technol. B 21.4., July/Aug 2003

[229] M. KITAZAWA, K. SHIOTANI, A. TODA, "Batch Fabrication of Sharpened Silicon Nitride Tips" Jpn. J. Appl. Phys. Vol. 42 pp. 4844–4847 (2003)

[230] V. Agache, R. Ringot, P. Bigotte, V. Senez, B. Legrand, L. Buchaillot, D. Collard, "Modeling and Experimental Validation of Sharpening Mechanism Based on Thermal Oxidation for Fabrication of Ultra-Sharp Silicon Nanotips", IEEE TRANSACTIONS ON NANOTECHNOLOGY, VOL. 4, NO. 5, SEPTEMBER 2005

[231] H. He, J. Zhang, J. Yang, F. Yang, "Silicon tip sharpening based on thermal oxidation technology", Microsyst Technol 23:1799–1803 (2017)

[232] B. Cui, Retrieved from https://ece.uwaterloo.ca/~bcui/ECE_343.html

[233] D-B Kao, J. P. McVittie, W. D. Nix, K. C. Saraswat, "Two-dimensional thermal oxidation of silicon—II. Modeling stress effects in wet oxides," IEEE Trans. Electron Devices, vol. 35, no. 1, pp. 25–37, Jan. 1988.

[234] M-Y. Jung, D. W. Kim, S. S. Choi, Y-S. Kim, Y. Kuk, K. C. Park, J. Jang, "Fabrication of a nanosized Si-tip coated with a thin diamond-like carbon film", Thin Solid Films 294, 157-159 (1997)

[235] T. S. Ravi, R. 8. Marcus, D. Liu, "Oxidation sharpening of silicon tips", J. Vac. Sci. Technol. B 9 (6), Nov/Dec 1991

[236] T. S. Ravi, R. 8. Marcus, D. Liu, "Oxidation sharpening of silicon tips", J. Vac. Sci. Technol. B 9 (6), Nov/Dec 1991

[237] V. Agache, R. Ringot, P. Bigotte, V. Senez, B. Legrand, L. Buchaillot, D. Collard, "Modeling and Experimental Validation of Sharpening Mechanism Based on Thermal Oxidation for Fabrication of Ultra-Sharp Silicon Nanotips", IEEE TRANSACTIONS ON NANOTECHNOLOGY, VOL. 4, NO. 5, SEPTEMBER 2005

[238] R. B. Marcus, T. S. Ravi, T. Gmitter, K. Chin, D. Liu, W. J. Orvis, D. R. Ciarlo, C. E. Hunt, and J. Trujillo, Appl. Phys. Lett. 56, 236 (1990).

[239] R. K. Dey, J. Shen, B. Cui, "Oxidation sharpening of silicon tips in the atmospheric environment", J. Vac. Sci. Technol. B 35(6), Nov/Dec 2017

[240] J. Li, "Dramatically enhanced polarization in (001), (101), and (111) BiFeO3 thin films due to epitaxial-induced transitions." Appl. Phys. Lett. 84, 5261 (2004).

[241] J. D. Plummer, M. D. Deal, P. B. Griffin, "Silicon VLSI Technology: Fundamentals, Practice, and Modeling", 1st ed. (Prentice Hall, NJ, 2000), p. 419.

[242] B. G. Streetman, S. Banerjee, "Solid State Electronic Devices", 5th ed. (Prentice Hall, NJ, 2000), p. 323.

[243] I. Cornago, A. L. Hernández, R. Casquel, M. Holgado, M. F. Laguna, F. J. Sanza, J. Bravo, "Bulk sensing performance comparison between silicon dioxide and resonant high aspect ratio nanopillars arrays fabricated utilizing interference lithography", OPTICAL MATERIALS EXPRESS, Vol. 6, No. 7, Jul 2016

[244] M. Hartensveld, "Optimization of Dry and Wet GaN Etching to Form High Aspect Ratio Nanowires", Master of Science in Material Science, College of Science, Rochester Institute of Technology, July 2018

[245] A. Tang, "Fabrication of High Aspect Ratio Microstructures using Time Multiplexed Reactive Ion Etching", Master thesis, Institute of Physics and Nanotechnology, Aalborg University, Denmark, www.nano.aau.dk, September 2015,

[246] M. Hartensveld, "Optimization of Dry and Wet GaN Etching to Form High Aspect Ratio Nanowires", Master of Science in Material Science, College of Science, Rochester Institute of Technology, July 2018

[247] A. Tang, "Fabrication of high aspect ratio microstructure using time multiplexed reactive ion etching", Master thesis, Institute of Physics and Nanotechnology, Aalborg University, Denmark, Spring 2015

[248] I. Cornago, A. L. Hernández, R. Casquel, M. Holgado, M. F. Laguna, F. J. Sanza, J. Bravo, "Bulk sensing performance comparison between silicon dioxide and resonant high aspect ratio nanopillars arrays fabricated by means of interference lithography", OPTICAL MATERIALS EXPRESS , Vol. 6, No. 7 , Jul 2016

[249] T. B. Kirchner, N. A. Hatab, N. V. Lavrik, M. J. Sepaniak, "Highly Ordered Silicon Pillar Arrays As Platforms for Planar Chromatography", Anal. Chem. 2013, 85, 11802−11808

[250] A. Frommhold, A. P.G. Robinson, E. Tarte, "High aspect ratio silicon and polyimide nanopillars by combination of nanosphere lithography and intermediate mask pattern transfer", Microelectronic Engineering 99 (2012) 43–49

[251] D. R. Lincoln, N. V. Lavrik, I. I. Kravchenko, M. J. Sepaniak, "Retention in Porous Layer Pillar Array Planar Separation Platforms", Anal. Chem. 2016, 88, 8741−8748

[252] S. Kalem, P. Werner, O. Arthursson, V. Talalaev, B. Nilsson, M. Hagberg, H. Frederiksen, U. Sodervall, "Black silicon with high density and high aspect ratio nanowhiskers", Nanotechnology 22 (2011) 235307

[253] Y. Li, Y. Hao, C. Huang, X. Chen, X. Chen, Y. Cui, C. Yuan, K. Qiu, H. Ge, Y. Chen, "Wafer Scale Fabrication of Dense and High Aspect Ratio Sub-50 nm Nanopillars from Phase Separation of Cross-Linkable Polysiloxane/Polystyrene Blend", ACS Appl. Mater. Interfaces 2017, 9, 13685−13693

[254] Y. Zargouni, S. Deheryan, A. Radisic, K. Alouani. P. M. Vereecken, "Electrolytic Manganese Dioxide Coatings on High Aspect Ratio Micro-Pillar Arrays for 3D Thin Film Lithium Ion Batteries", Nanomaterials 2017, 7, 126

[255] L . V. Asquez-Garc, A. Akinwande, "Fabrication of large arrays of high-aspect-ratio single-crystal silicon columns with isolated vertically aligned multi-walled carbon nanotube tips", Nanotechnology 19 (2008) 405305

[256] J. Aebersold, K. Walsh, M. Beggans, "Utilization of Direct Write Lithography to Develop Ultra High Aspect Ratio (>100:1) DRIE Silicon Pillars", IEEE Xplore Conference, West Lafayette, IN, USA 15 July 2010

[257] M. A. Verschuuren, M. W. Knight, M. Megens, A. Polman, "Nanoscale spatial limitations of large-area substrate conformal imprint lithography", Nanotechnology 30 (2019) 345301

[258] K. NAKAMATSU, M. OKADA, S. MATSUI, "Fabrication of High-Aspect Si Structures by Deep Reactive Ion Etching Using Hydrogen Silsesquioxane Masks Replicated by Room Temperature Nanoimprinting", Japanese Journal of Applied Physics Vol. 47, No. 11, 2008, pp. 8619–8621

[259] Y. Lee, H. Kim, S. Q. Hussain, S. Han, N. Balaji, Y-J Lee, J. Lee, J. Yi, "Study of metal assisted anisotropic chemical etching of silicon for high aspect ratio in crystal line silicon solar cells", Materials Science in Semiconductor Processing 40. 391–396 (2015)

[260] R. A. Morris, R. L. Martens, I. Zana, G. B. Thompson, "Fabrication of high-aspect ratio Si pillars for atom probe 'lift-out' and field ionization tips" Ultramicroscopy 109 (2009) 492–496

[261] A. Ayari-Kanoun, F. Aydinoglu, and B. Cui, "Silicon nanostructures with very large negatively tapered profile by inductively coupled plasma-RIE" J. Vac. Sci. Technol. B, 34, 06KD01 (2016).

[262] B. Cui, University of Waterloo, ECE Department course, retrieved from https://ece.uwaterloo.ca/~bcui/ECE_730.html.

[263] M D Henry, "ICP Etching of Silicon for Micro and Nanoscale Devices", PhD thesis, California Institute of Technology, Pasadena, California, (2010)

[264] B. D. Gates, Q Xu, M Stewart, D Ryan, C G Willson, G M Whitesides, "New approaches to nanofabrication: molding, printing, and other techniques" Chem. Rev. 105 1171–96 (2005)

[265] C R K Marrian, D M Tennant, Nanofabrication J. Vac. Sci. Technol. A 21 S207–15 (2003)

[266] J Gierak et al, "Exploration of the ultimate patterning potential achievable with high resolution focused ion beams", Appl. Phys. A 80 187–94 (2005)

[267] F Watt, A Bettiol, J Van Kan, E Teo, M Breese "Ion beam lithography and nanofabrication: a review" Int. J. Nanosci. 4 269–86 (2005)

[268] Z. Han, M. Vehkamäki, M. Mattinen, E. Salmi, K. Mizohata, M. Leskelä, M. Ritala, "Selective etching of focused gallium ion beam implanted regions from silicon as a nanofabrication method", Nanotechnology 26 (2015) 265304 (10pp)

[269] A A Tseng, "Recent developments in nanofabrication using focused ion beams", Small 1 924–39 (2005)

[270] A. F. EVASON, J. R. A. CLEAVER, H. AHMED, "Fabrication and Performance of GaAs MESFET's with Graded Channel Doping Using Focused Ion-Beam Implantation", IEEE ELECTRON DEVICE LETTERS, VOL. 9, NO. 6, JUNE 1988 281

[271] C-S Kim, S-H Ahn, D-Y Jang, "Review: developments in micro/nanoscale fabrication by focused ion beams" Vacuum 86 1014–35 (2012)

[272] N Chekurov, K Grigoras, A Peltonen, S Franssila, I Tittonen, "The fabrication of silicon nanostructures by local gallium implantation and cryogenic deep reactive ion etching", Nanotechnology 20 (2009) 065307 (5pp)

[273] M. M. Mitan, D. P. Pivin, T. L. Alford, and J. W. Mayer, "Direct patterning of nanometer-scale silicide structures by focused ion-beam implantation through a thin barrier layer", Journal of Vacuum Science & Technology B 19, 2525 (2001)

[274] M. David Henry, S Wolfley, T Monson, R Lewis, "Ga lithography in sputtered niobium for superconductive micro and nanowires", APPLIED PHYSICS LETTERS 105, 072601 (2014)

[275] H. J. LEZEC, K. ISMAIL, L. J. MAHONEY, M. I. SHEPARD, D. A. ANTONIADIS, J. MELNGNLIS, "A Tunable-Frequency Gunn Diode Fabricated by Focused Ion-Beam Implantation", IEEE ELECTRON DEVICE LETTERS, VOL. 9, NO. 9, SEPTEMBER 1988

[276] B Schmidt, L Bischoff, J Teichert, “Writing FIB implantation and subsequent anisotropic wet chemical etching for fabrication of 3D structures in silicon”, Sensors Actuators A 61 369–73 (1997)
[277] Brugger J, Beljakovic G, Despont M, De Rooij N F and Vettiger P 1997 Silicon micro/nanomechanical device fabrication based on focused ion beam surface modification and KOH etching Microelectron. Eng. 35 401–4
[278] Kawasegi N, Morita N, Yamada S, Takano N, Oyama T, Ashida K, Taniguchi J and Miyamoto I 2006 Three-dimensional nanofabrication utilizing selective etching of silicon induced by focused ion beam irradiation JSME Int. J. C 49 583–9
[279] Bischoff L, Schmidt B, Lange H and Donzev D 2009 Nano-structures for sensors on SOI by writing FIB implantation and subsequent anisotropic wet chemical etching Nucl. Instrum. Methods Phys. Res. B 267 1372–5
[280] Z. Liu, K. Iltanen, N. Chekurov, K. Grigoras, I. Tittonen, “Aluminum oxide mask fabrication by focused ion beam implantation combined with wet etching”, Nanotechnology 24 (2013) 175304 (6pp)
[281] Fischer A C, Belova L M, Rikers Y G M, Malm B G, Radamson H H, Kolahdouz M, Gylfason K B, Stemme G and Niklaus F 2012 3D free-form patterning of silicon by ion implantation, silicon deposition, and selective silicon etching Adv. Funct. Mater. 22 4004–8
[282] Chekurov N, Grigoras K, Sainiemi L, Peltonen A, Tittonen I and Franssila S 2010 Dry fabrication of microdevices by the combination of focused ion beam and cryogenic deep reactive ion etching J. Micromech. Microeng. 20 085009
[283] La Marche P H, Levi-Setti R and Wang Y L 1983 Focused ion beam microlithography using an etch-stop process in gallium-doped silicon J. Vac. Sci. Technol. B 1 1056–8
[284] Sievil¨a P, Chekurov N and Tittonen I 2010 The fabrication of silicon nanostructures by focused-ion-beam implantation and TMAH wet etching Nanotechnology 21 145301
[285] E. Coyne, G. M O’Connor, “Fabrication of silicon-blazed phase diffractive gratings using grey scale gallium implantation with KOH anisotropic etch”, J. Micromech. Microeng. 20 (2010) 085037 (8pp)
[286] H. C. Mogul, A. J. Steckl, “Rapid Thermal Annealing Effects on Si p+-n Junctions Fabricated by Low-Energy FIB Ga+ Implantation”, IEEE ELECTRON DEVICE LETTERS, VOL. 14, NO. 3, MARCH 1993 123
[287] H. C. Mogul, A. J. Steckl, E. Ganin, “Electrical Properties of Si p+-n Junctions for Sub-0.25 pm CMOS Fabricated by Ga FIB Implantation”, IEEE TRANSACTIONS ON ELECTRON DEVICES, VOL. 40, NO. IO, OCTOBER 1993 1823
[288] H X Qian, W. Zhou, J. Miao, Lennie, E N Lim, X R Zeng, “Fabrication of Si microstructures using focused ion beam implantation and reactive ion etching”, J. Micromech. Microeng. 18 (2008) 035003 (5pp)
[289] B Schmidt, S Oswald, L Bischoff, J. Electrochem. Soc. 152 G875 (2005)
[290] C.M. Park, J. A. Bain, T. W. Clinton, P. A. A. van der Heijden, and T. J. Klemmer, “Measurement of Ga implantation profiles in the sidewall and bottom of focused-ion-beam-etched structures”, APPLIED PHYSICS LETTERS VOLUME 84, NUMBER 17 26 APRIL 2004
[291] K D Choquette, L R Harriott, “Dry lithography using focused ion beam implantation and reactive ion etching of SiO2”, Appl. Phys. Lett. 62 3294–6 (1993)
[292] F. Vallini, L. A. M. Barea, E. F. Reis, A. A. Zuben, N. C. Frateschi, “Induced Optical Losses in Optoelectronic Devices due to Focused Ion Beam Damages”, Journal of Integrated Circuits and Systems 7(2) · July 2012
[293] S. Waid, H D Wanzenboeck, M. Muehlberger, M. Gavagnin, E. Bertagnolli, “Generation of 3D nanopatterns with smooth surfaces”, Nanotechnology 25 (2014) 315302 (10pp)
[294] P Roediger, H D Wanzenboeck, S Waid, G Hochleitner, E Bertagnolli, “Focused-ion-beam-inflicted surface amorphization and gallium implantation—new insights and removal by focused-electron-beam-induced etching’, Nanotechnology 22 (2011) 235302 (10pp)
[295] J F Ziegler, J Biersack, U Littmark, “The Stopping and Range of Ions in Solids: Stopping and Range of Ions in Matter”, vol 1 (New York: Pergamon) 8 (1985)
[296] N Chekurov, K Grigoras, A Peltonen, S Franssila, I Tittonen, “The fabrication of silicon nanostructures by local gallium implantation and cryogenic deep reactive ion etching”, Nanotechnology 20 (2009) 065307 (5pp)
[297] K Arshak, M Mihov, S Nakahara, A Arshak, D McDonagh, “Investigations of the Ga+ focused-ion-beam implantation in resist films for nanometer lithography applications”, Journal of Vacuum Science & Technology B 22, 3016 (2004)
[298] O Hildreth, K Rykaczewski, C. P. Wonga, “Participation of focused ion beam implanted gallium ions in metal-assisted chemical etching of silicon”, J. Vac. Sci. Technol. B 30, 040603 (2012)
[299] Y Tu , B Han, Y Shimizu , K Inoue, Y Fukui, M Yano, T Tanii, T Shinada, Y Nagai, “Atom probe tomographic assessment of the distribution of germanium atoms implanted in a silicon matrix through nano-apertures”, ECS Transactions, 9 (1) 123-132 (2007)

[300] M D Henry, “ICP Etching of Silicon for Micro and Nanoscale Devices”, PhD thesis, California Institute of Technology, Pasadena, California, (2010)
[301] S. Coffa, L. Calcagno, S. U. Campisano, G. Calleri, and G. Ferla, "Control of Minority Carrier Lifetime by Gold Implantation", J. Electrochem. Soc., Vol. 136, No. 7, July 1989
[302] D Jaworska, E. Tarnowska, “Gettering of Au atoms in silicon induced by ion Implantation”, J. Phys. D Appl. Phys. 26 (1993) 22262230.
[303] T. W. Sigmon, L. Csepregi, J. W. Mayer, “Ion Implantation Gettering of Gold in Silicon”, J. Electrochem. Soc. 123 1116 (1976)
[304] H Detz, T U Wien, M Kriz, T Zederbauer, “Lithography-free positioned GaAs nanowire growth with focused ion beam implantation of Ga“, J. Vac. Sci. Technol. B 35, 011803 (2017)
[305] F. S. Teixeiraa,b, R. D. Mansanoa, M. C. Salvadorib, M. Cattanib and I. G. Brownc “Anisotropic Resistivity of PMMA Doped with Gold”, ECS Transaction, 9 (1) 123-132 (2007)
[306] M. C. Salvadori, F. S. Teixeira, L. G. Sgubin, W. W. R. Araujo, R. E. Spirin, M. Cattani, E. M. Oks, I. G. Brown, “Gold ion implantation into alumina using an “inverted ion source” Configuration“, REVIEW OF SCIENTIFIC INSTRUMENTS 85, 02B502 (2014)
[307] F. S. Teixeira, M. C. Salvadori, Mauro Cattani, S. M. Carneiro, I. G. Brown, “Surface plasmon resonance of gold nanoparticles formed by cathodic arc plasma ion implantation into polymer“, Journal of Vacuum Science & Technology B 27, 2242 (2009)